CHARACTERIZING AQUIFER HETEROGENEITY USING HYDRAULIC TOMOGRAPHY

Submitted to the Department of Geology and the Faculty of the Graduate School of the University of Kansas in partial fulfillment of the requirements for the degree of Master of Science

Brian J. Wachter
B.S. The College of William and Mary, 2006

Advisory Committee:

_____
Dr. Carl McElwee, Chairman

_____
Dr. John F. Devlin

_____
Dr. George Tsoflias

Date Defended:_____

C2008

The Thesis Committee for Brian J. Wachter certifies that this is the approved version of

the following thesis:

CHARACTERIZING AQUIFER HETEROGENEITY USING HYDRAULIC TOMOGRAPHY

Advisory Committee:

_____
Dr. Carl McElwee, Chairman

_____
Dr. John F. Devlin

_____
Dr. George Tsoflias

Date Defended:_____

Abstract

Fine-scale heterogeneity in a geologic medium determines rates and directions of flow and of contaminant transport. Traditional methods of determining hydraulic conductivity provide only average values of hydraulic conductivity, as opposed to a distribution throughout the aquifer. Hydraulic tomography can be used to relate phase shifts and amplitude decays of a sinusoidal pressure signal to hydraulic conductivity. Hydraulic tomography can provide fine-scale interwell resolution, but processing methods require extensive time and computing power to handle the large amounts of data necessary. This tomography study comprises a combination of multiple offset gather surveys taken at the University of Kansas' Geohydrologic Experimental and Monitoring Site, a well-studied site in northeastern Kansas. A computer program has been developed to analyze the data by extending the 3D homogeneous spherical radial equation to the heterogeneous case. The analysis program is capable of efficiently resolving zones with dimensions of about one meter on each side.

Acknowledgements

I would like to thank Dr. Carl McElwee for being my advisor on this project.

I would like to thank Dr. Rick Devlin and Dr. George Tsoflias for serving on my thesis committee.

I would like to thank Pema Deki, Shane Lyle, Ben Ramaker, Rebecca Smedlund, and Christopher Volek for field assistance.

This research was funded in part through the Strategic Environmental Research and Development Program (SERDP).

Table of Contents

LIST OF FIGURES

LIST OF TABLES

CHAPTER 1: Introduction and Previous Work

A. Objectives

The objectives of this study are to determine if hydraulic conductivity values obtained by hydraulic tomography are an effective means of characterizing aquifer heterogeneity. The individual goals within this objective are to construct field equipment to expedite data collection, to develop a program that reduces the computing power and time needed for data processing, to determine the maximum resolution of this model, and to apply the model to a well-studied field site to test its applicability with real world data.

B. Introduction

Hydraulic conductivity is a primary control on the travel path of contaminants. Hydraulic conductivity, or K, is defined as the ease with which a liquid moves through a geologic material. K is related to properties of both the geologic material and the fluid. It is a factor of grain size, sorting, porosity, and the interconnectedness of pores. K can vary by orders of magnitude even across small distances due to heterogeneities in aquifer material. Water, and therefore contaminants traveling with the water, will preferentially flow through regions of higher K. This fine-scale heterogeneity must be understood to determine the fate of these contaminants. Hydraulic tomography is one method of obtaining this fine scale resolution. Hydraulic tomography has traditionally required a large amount of computing power and time to process the large amount of data collected because traditional processing programs use nonlinear equations that require iterations to solve.

The most basic equation involving K is Darcy's Law:

$$Q = -KAI \tag{1}$$

The discharge, Q, is a product of K, the area through which water is flowing (A), and the hydraulic gradient (I). The hydraulic gradient is more completely described as

$$I = \frac{dh}{dl} \tag{2}$$

The hydraulic gradient is simply the slope of hydraulic head (h), equal to the change in hydraulic head divided by the distance between measuring points (l). The resulting value is unitless. Hydraulic head is a measure of energy per unit weight and reduces to units of length. There are three components incorporated into total head: the elevation head, the pressure head, and the velocity head. The components can all be expressed in terms of Bernoulli's equation, describing conditions of steady flow.

$$gz + \frac{P}{\rho_w} + \frac{v^2}{2} = \text{constant} \tag{3}$$

where g is the acceleration due to gravity, z is the elevation distance from a datum to the piezometer, P is the pressure from the water column, ρ_w is the density of water, and v is velocity. The constant in the equation is the total head. The equation is more commonly expressed after dividing through by g:

$$z + \frac{P}{\rho_w g} + \frac{v^2}{2g} = \text{constant} \tag{4}$$

The first term in equation (4) is the elevation head, the second term is the pressure head, and the third term is the velocity head. In groundwater studies, the velocity term is usually much smaller than the other two terms, so equation (4) reduces to

$$h = z + \frac{P}{\rho_w g} \quad (5)$$

The pressure head is equal to zero at the water's surface, so the total head can be determined by measuring the elevation of the water column.

Transmissivity, T, can be expressed as a function of K.

$$T = Kb \quad (6)$$

The transmissivity is the amount of water that can flow through a unit width of saturated aquifer with thickness b and under a hydraulic gradient of 1 (Fetter, 2001). Transmissivity is expressed as a length squared per time. The storativity, S, is defined as volume of storage per unit volume of aquifer material and is expressed as

$$S = S_s b \quad (7)$$

with units of length. The specific storage, S_s, is a unitless value expressed as

$$S_s = \rho g(\alpha + n\beta) \quad (8)$$

S_s is a function of the fluid density, ρ, the acceleration of gravity, g, fluid compressibility, α, porosity n, and aquifer compressibility, β. Diffusivity, D, is the ratio of the above parameters

$$D = \frac{T}{S} = \frac{K}{S_s} \quad (9)$$

A pressure transducer is a device that measures pressure, in this case water pressure. To make a conversion to water levels inside piezometers, a separate method of measuring the water level must be used. Although the pressure transducer does not measure water level directly, it can accurately record small-scale changes in the

height of water above the sensor with multiple measurements taken every second, if desired. High frequency measurements of this kind are important in high K materials.

C. Theory

A one-dimensional transient pressure head signal with sinusoidal boundary conditions is described by the equation (Engard, 2006)

$$h(r,t) = h_0 e^{d} \sin\left(\Phi_0 - \Phi_r\right) \qquad (10)$$

The head at any radius (r) and time (t) is h(r,t), h_0 is the initial amplitude of pressure head fluctuation, e^d is a decay term, the source reference phase is Φ_0, and Φ_r is the phase shift. Equation (10) can be adapted to other coordinate systems. In the homogeneous three-dimensional spherical radial system, the aquifer response is given by the following equation (Engard, 2006):

$$h(r,t) = h_0 \frac{e^{-\sqrt{\frac{\pi f S_s}{K}} r}}{r} \sin\left(2\pi f t - \sqrt{\frac{\pi f S_s}{K}} r\right) \qquad (11)$$

where f is the frequency, S_s is the specific storage, and K is the hydraulic conductivity. Equation (11) incorporates terms for the amplitude, AMP

$$AMP_r = h_0 \frac{e^{-\sqrt{\frac{\pi f S_s}{K}} r}}{r} \qquad (12)$$

the sinusoidal source phase, Φ_0

$$\Phi_0 = \sin(2\pi f t) \qquad (13)$$

and for the phase shift between source and receiver, Φ_r

$$\Phi_r = -\sqrt{\frac{\pi f S_s}{K}} r = d \qquad (14)$$

Equation (10) is transformed to the heterogeneous case by the following substitution:

$$\sqrt{\frac{\pi f S_s}{K}} r \Rightarrow \sum_{i=1}^{I} \sqrt{\frac{\pi f S_s}{K_i}} \left(r_i - r_{i-1} \right) \qquad (15)$$

The reasoning for the transformation made in equation (15) is explained later in the Modeling section.

D. Previous Work

K can be measured in the laboratory using cored material obtained by a variety of drilling methods. Either constant head or falling head permeameters can be used, depending on the type of material. A falling head permeameter is used for low K materials like silts and clays because extra pressure can be added to speed up the water movement. The constant head permeameter is preferred for high K materials such as sands and gravels because these materials drain the water so quickly. The K value is highly localized and only represents the portion of the aquifer in which the core was taken. When working with unconsolidated sediments, care must be taken to pack the permeameter in a similar manner to the packing when the core was removed.

Pumping tests provide large-scale estimates of K and S_s. Water is removed from one well and water levels are monitored at other wells in the surrounding area. The water levels, h_i, can easily be converted to drawdown values, s_i, by taking measurements of initial head, h_o; i.e., $s_i = h_o - h_i$. The drawdowns in the observation wells can be analyzed together to provide an average K value over a large portion of the aquifer.

Slug tests are commonly used to characterize hydraulic conductivity values on a smaller scale. Traditional slug tests, used since the 1950s, provide an average K value for the whole well (Hvorslev, 1951). The water level is varied by the addition or removal of water, or by adding or removing a solid slug. High resolution slug tests (HRST) have been used in more recent years to provide point measurements of K near a well. Packers isolate small vertical sections of the well screen for independent testing. Pneumatic methods, in which positive or negative pressure is applied to the water column, are increasingly being used because no water need be added or removed. This feature is both convenient and advantageous at sites where the groundwater is contaminated, and cannot be removed from a well without disposal. Pressure transducers have been especially important for characterizing high K materials (Prosser, 1981). A double packer system is used with a sensor located between the packers. One or more initial pressures are used and then the slugged location is moved. The data from each location can be analyzed independently to provide a vertical profile of K values within the well. Due to the cost involved with well installation, efforts have been made to acquire interwell K values using tomographic methods and therefore maximize the amount of information from a small number of wells.

Tomography was initially developed for the medical field to provide high quality images of the interior of the body (Shepp and Kruskal, 1978). The tomographic survey was later employed in geology. Today, a variety of geophysical tomography surveys are used for hydrogeological applications. In all cases, a signal

is generated at a source, the signal propagates through a medium, and a receiver records the resulting signal. The change in the signal can be related to the properties of the medium between sensors. Multiple source and receiver locations are used, and the resulting grid of rays is analyzed simultaneously. The solutions from geophysical surveys are not unique, so multiple methods are often used together for correlation.

Seismic, ground penetrating radar (GPR), and electrical resistivity are geophysical methods that are commonly used in tomography studies. None of the methods give direct measurements of hydraulic conductivity, but the results can be used to infer information about the types of geologic materials in the study area. For example, seismic refraction tomography was used to estimate the transition zone between bedrock and saprolite and then electrical resistivity tomography was used to target suspected regions of a contaminant plume (Watson et al., 2005). Karasaki etl al. (2000) used seismic tomography and GPR tomography to classify fractures in a study site and verified results with tracer tests. Geophysical logs were used in conjunction with borehole GPR to monitor the movement of a vegetable oil emulsion used to stimulate biodegradation (Lane Jr. et al., 2006).

Unlike other tomographic methods, hydraulic tomography can be used to measure hydraulic conductivity. Hydraulic tomography studies have used either a pneumatic source or a pumped well as the source. A series of short term pumping tests can be used to initiate the tomography study (Butler, McElwee, and Bohling, 1999). A continuous pulse test (CPT) uses a continuous sinusoidal pressure source with observable phase shift and amplitude decay between source and receiver

(Engard, 2006). Like the pneumatic slug tests, the CPT has an advantage over pumping tests in that no water is removed from the aquifer and therefore no disposal is required. Both types of sources can provide estimates of K values, but they require different processing methods.

Much of the work done on hydraulic tomography focused on developing appropriate processing methods. Yeh and Liu (2000) developed a sequential iterative model to process the large amount of data generated in a hydraulic tomography study based on an analysis of drawdown as a function of time. The model is known as the sequential successive linear estimator (SSLE). The tomogram of Yeh and Liu (2000) can be validated by a variety of methods (Illman et al., 2007; Liu et al., 2007). Electrical potential measurements, made on the surface, have been related to hydraulic head and drawdown and subsequently analyzed for transmissivity values also using the SSLE method (Straface et al., 2007). Results are most accurate when the cleanest data are added first to the SSLE algorithm and noisier data are progressively added (Illman et al., 2008). Hydraulic travel time analysis has been employed based on analyses previously adapted for seismic tomography (Brauchler et al., 2007). The study used slug tests in closely spaced wells as the source. Li et al. (2007) examined a series of pumping tests to determine whether interpolation by kriging from type-curve analysis is as effective as geostatistical inversion. The geometric mean values of transmissivity and storativity are roughly the same with both methods, but the type-curve analysis did not resolve the spatial variability of transmissivity as well. Hydraulic tomography has been extended to a synthetic tracer

study to characterize a dense nonaqueous phase liquid (DNAPL) (Yeh and Zhu, 2007). DNAPLs are present at many contaminated sites and are particularly difficult to remediate. The DNAPL field will not be adequately characterized if head measurements are not taken in addition to concentration measurements, so the tracer test works best when paired with hydraulic tomography. Fractures are regions of high hydraulic conductivity, so it is important to accurately map their locations. Synthetic studies have shown that the SSLE algorithm can be applied to characterize fracture patterns and connectivity, with the best results when more wells are added (Hao et al., 2007). Computation time can be greatly reduced with little change in the inversion results by using a steady shape analysis (Bohling et al., 2007). Hydraulic gradients around a pumping well reach steady state before the head values reach steady state; head differences can therefore be analyzed based on a steady state model, although the head values cannot be.

E. Field Site

The University of Kansas' Geohydrologic Experimental and Monitoring Site (GEMS) is a well-studied alluvial aquifer located along the Kansas River floodplain in northeastern Kansas (Figure 1). About 11 m of coarse sand and gravel are overlain by about 11 m of silts and clays. The aquifer is considered to be semi-confined, as the silts and clays mostly cover the underlying sediments. The surficial sediments have been mapped as Newman Terrace deposits (O'Connor, 1992). Underlying the unconsolidated sediments is the Pennsylvanian age Tonganoxie sandstone. Clay lenses of up to one meter in size have been found within the sand and gravel layer

(Healey et al., 2004**)**. There is also a large degree of fine-scale heterogeneity even within a single type of material.

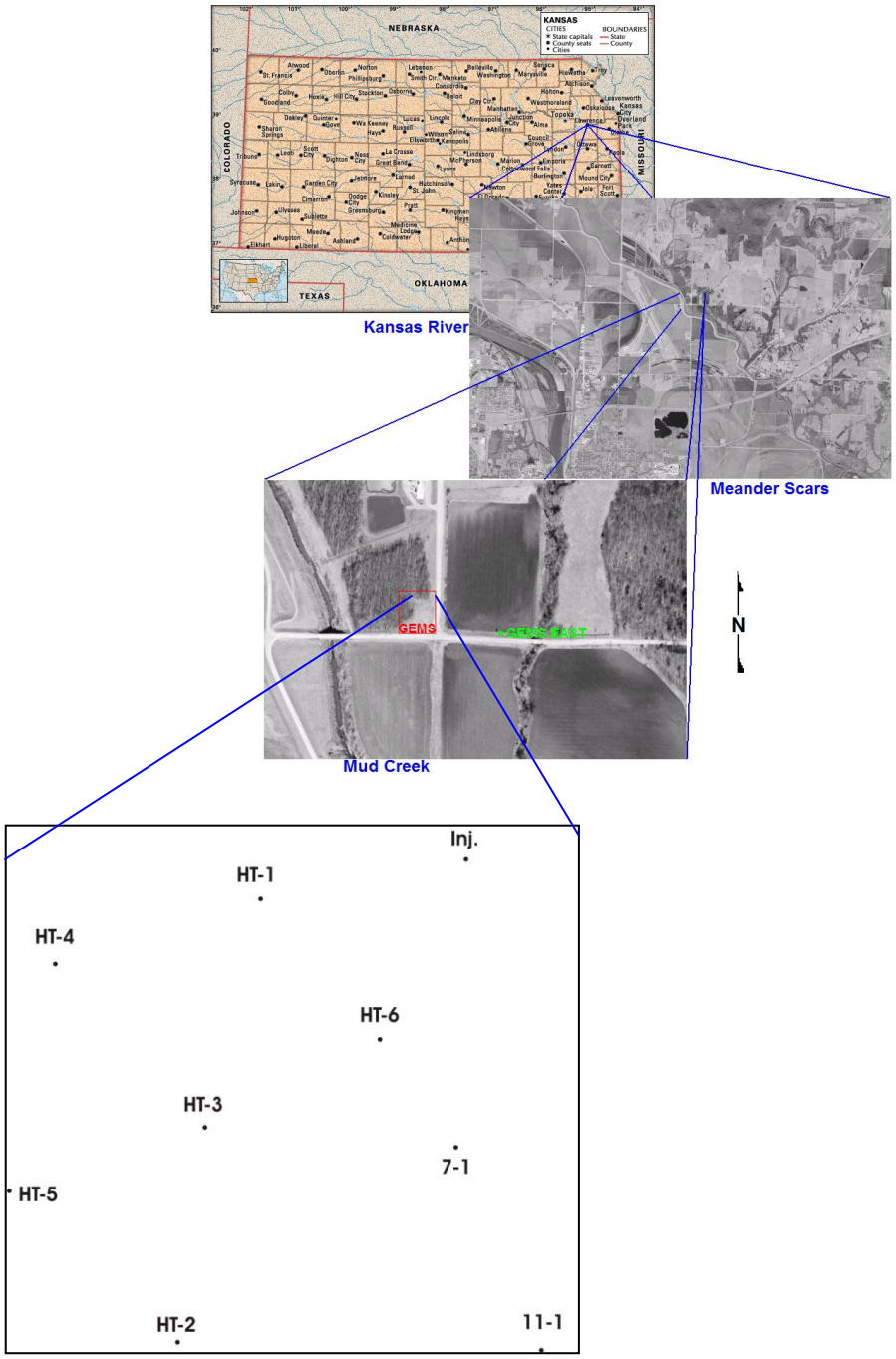

Figure 1: Map of GEMS and layout of wells used in study (figure modified from Engard, 2006).

The aquifer properties at GEMS have been extensively studied using many of the methods mentioned in the previous section. K values were estimated using an electrolytic solution in a single well injection tracer test (Huettl, 1995). K values were also estimated using an induced gradient tracer test and multilevel sampling wells (Bohling, 1999). The direct push method was used next to the tracer experiment wells to obtain both electrical conductivity (EC) profiles as wells as slug tests (Sellwood, 2001). HRST profiles were taken in ten wells at the site in a previous study (Ross, 2005; Ross and McElwee, 2007). Additional HRST profiles had to be conducted in the wells used for the hydraulic tomography study, but results from previous profiles provided a general idea of the variation to expect from heterogeneity. Most recently, the CPT method was used to collect zero offset profile (ZOP) data in three of the wells used in this study (Engard, 2006).

CHAPTER 2: Methods

A. Field Methods

Surveys were done in the form of multiple offset gathers (MOGs). For a MOG, a packed off source excitation interval with a transducer is kept at a fixed depth in the source well while another packed off receiver interval with a transducer is moved throughout the entire screened interval of the receiver well. This procedure is then repeated multiple times with systematically varied locations of the source excitation interval. The packed off intervals in both the source and receiver wells were about 0.5 m in length. For this study, measurements were taken in either 0.305

meter (one foot) or 0.914 m (3 foot) intervals. Once measurements had been taken between one source location and all the receiver locations, the source was moved by 0.305 or 0.914 meters and measurements were again taken at all the receiver locations. The process was repeated until rays had traveled from every location in the source well to every location in the receiver well, as shown schematically in Figure 2. The collective examination of these multiple ray paths forms the tomographic study.

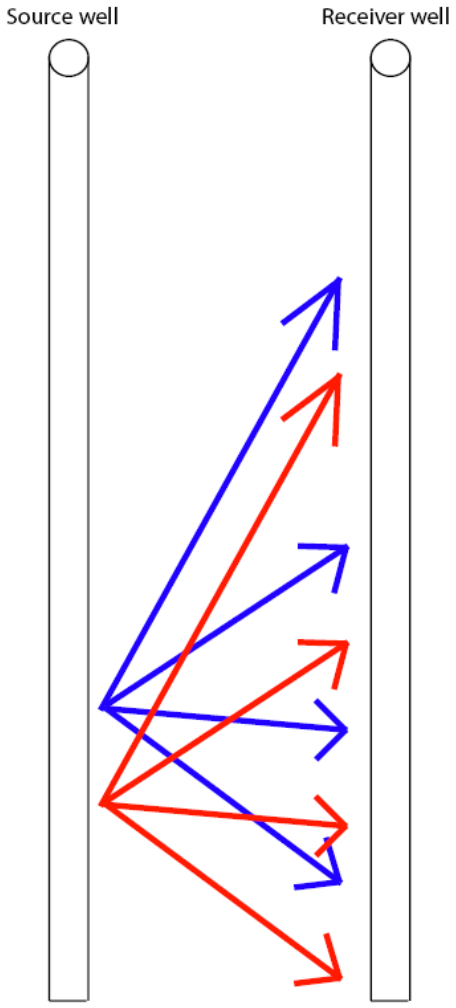

Figure 2: MOG setup for the tomographic study showing two source locations. In actual tests, as many as 26 source locations will constitute the survey.

Initially, a single-channel receiver was used in data collection. One pressure transducer was placed at the level of a port in the receiver, with inflatable packers on either side of the port to isolate the response to a small portion of the well. The packers are connected to a nitrogen tank, which inflates them. When packers are used, the amplitudes seen in the receiver well increase and the signal more closely matches the signal in the source well (Figure 3).

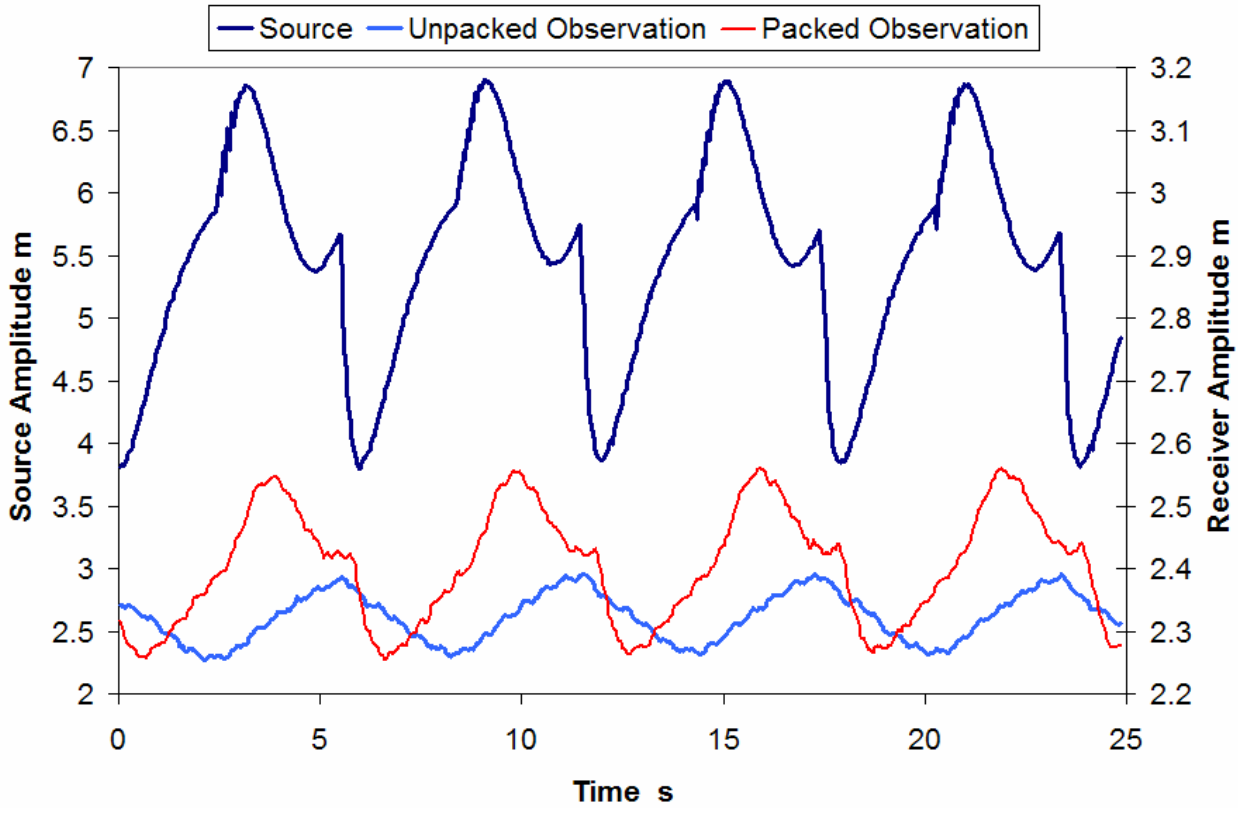

Figure 3: The response in an observation well will differ in terms of both amplitude and shape depending on whether the interval is packed or unpacked (Figure from Engard, 2006).

Before each survey, a steel tape is attached to both the source and receiver riser pipes a known distance above the packers. The steel tape reading, in

conjunction with surveying of well casing elevations, allows comparison from one well to another through a conversion to elevations. The zero reading on the tape is not in the same place as the transducer port, so a correction must be added to convert to a true depth below top of casing. For the source packer, 0.94 meters (3.1 feet) are added to the steel tape reading. In more recent surveys, a multi-level receiver has been used instead of the single-channel receiver. A multi-level receiver with five pressure transducers was constructed to expedite data collection. Each port in the multi-level receiver is isolated by packers on either side (Figure 4). The MOGs collected with the single-channel receiver were repeated using the multi-level receiver to ensure the results were equivalent within the range of experimental accuracy. For the receiver packer, there are five pressure transducers stacked vertically throughout the riser pipe. The correction is different for each transducer, as there are 0.914 meters (3 feet) between transducers. Only the correction for the deepest transducer needs to be input into the data processing program, as the program automatically calculates the other four transducer locations based on the packer instrumentation dimensions. For the receiver, 4.5 meters (14.9 feet) are added to the steel tape reading to get the deepest transducer's location.

Figure 4: Multi-level receiver array consisting of 5 ports isolated by 6 packers.

For each survey, two pressure transducers are placed in the source well. Two transducers are used to measure the ratio of the input signal, at the top of the well, to the input signal lower in the well. The deeper transducer is measured out to be at the same depth as the center of the packed off interval. The shallower transducer is dropped to a depth of 5.2 meters (17 feet) below the water surface. The computer is used to verify the feet of water above the shallower transducer. As the source location changes, the bottom transducer is pulled up along with the port and therefore remains at its desired location between the packers, but the shallow transducer must

be adjusted for each new source location to maintain its position at 5.2 meters below water level.

The continuous pulse test (CPT) uses a pneumatic source for the periodic pressurization and depressurization of a well column. The period of this oscillation can be regulated by a frequency generator connected to an air compressor. Pressure is supplied to the well column through a connection at the top of the well. When pressure is supplied, the water level lowers, and when the valve releases the pressure, the water level rises. The periodic pressurization and depressurization causes an oscillation of the water column with a sinusoidal pattern. A total of seven pressure transducers in later surveys, two in the source well and five in the receiver well, are connected to a datalogger which in turn sends the data to the computer. A grounding rod is connected to the datalogger to minimize interference from off-site electrical equipment. The computer data can be analyzed to determine changes in the amplitude and phase of the sinusoidal wave as a function of source and receiver location.

MOGs were collected in the fall of 2006 with the single-channel receiver. HT-3 was used as the source well and HT-1 was used as the receiver well. Due to the time involved for a single survey with the single-channel receiver, only five MOGs were collected. The five were chosen at varying depths to attempt to roughly characterize the whole area between these two wells. The maximum range of measurement in the well ranged from a depth of 12.31 m (40.4 ft) to a depth of 21.15 m (69.4 ft). The maximum depth was limited by the total depth of the well, and the

minimum depth was limited by attenuation from the overlying clay material. MOGs were collected at source elevations of 237.8 m (Fig. 5), 236.6 m (Fig. 6), 235.4 m (Fig. 7), 234.5 m (Fig. 8), and 233.4 m (Fig. 9). The target elevation for the final MOG was 233.25 m, but material had filled in the bottom of the source well. The well was purged in the spring of 2007 to remove this extra material. These first five MOGs were repeated in the spring of 2007 with the multi-level receiver for comparison to the single-channel receiver data. The phase shifts between source and receiver transducers for each MOG are presented in Figures 5-9.

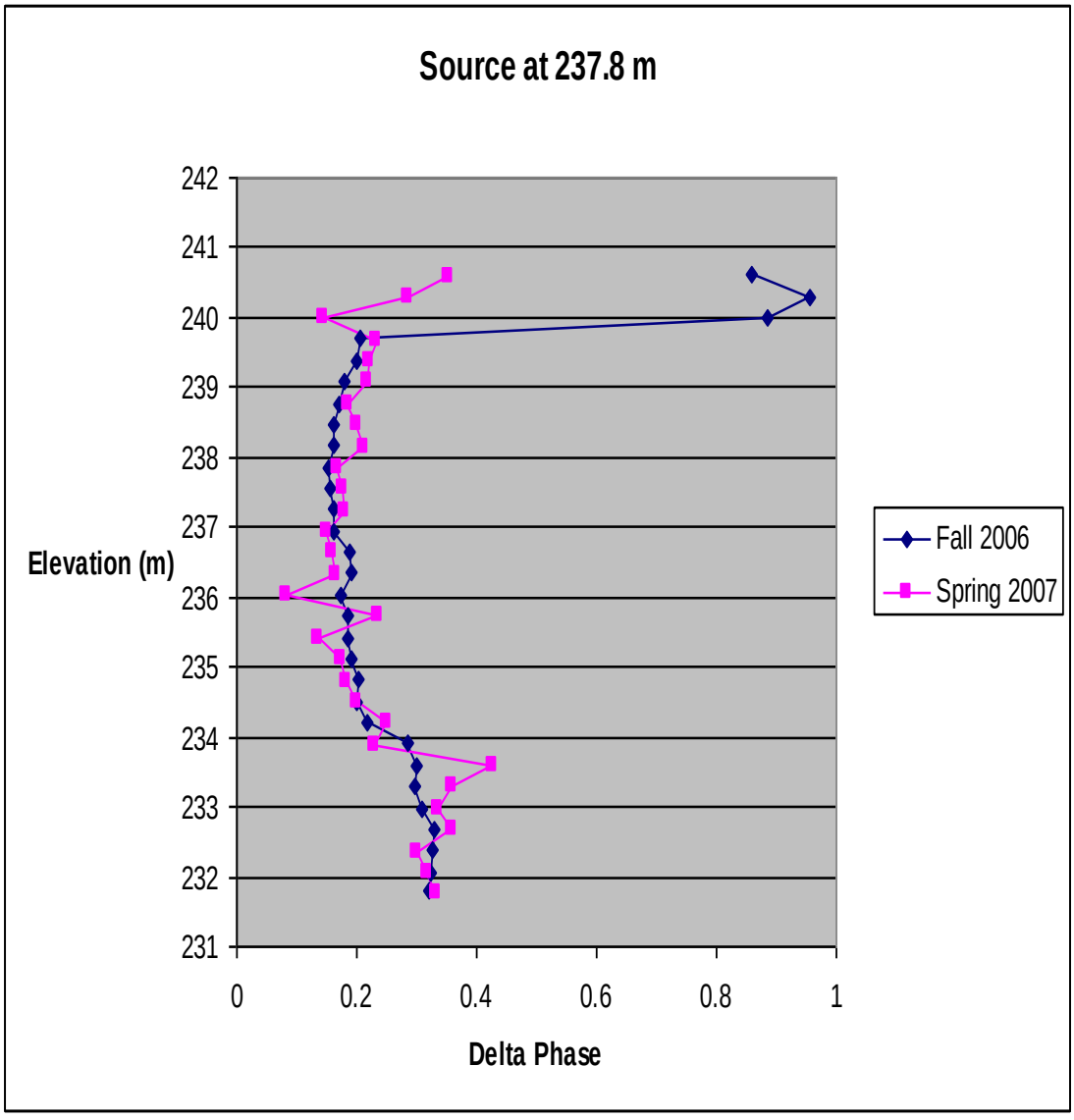

Figure 5: Comparison of fall and spring MOGs from a source elevation of 237.8 m.

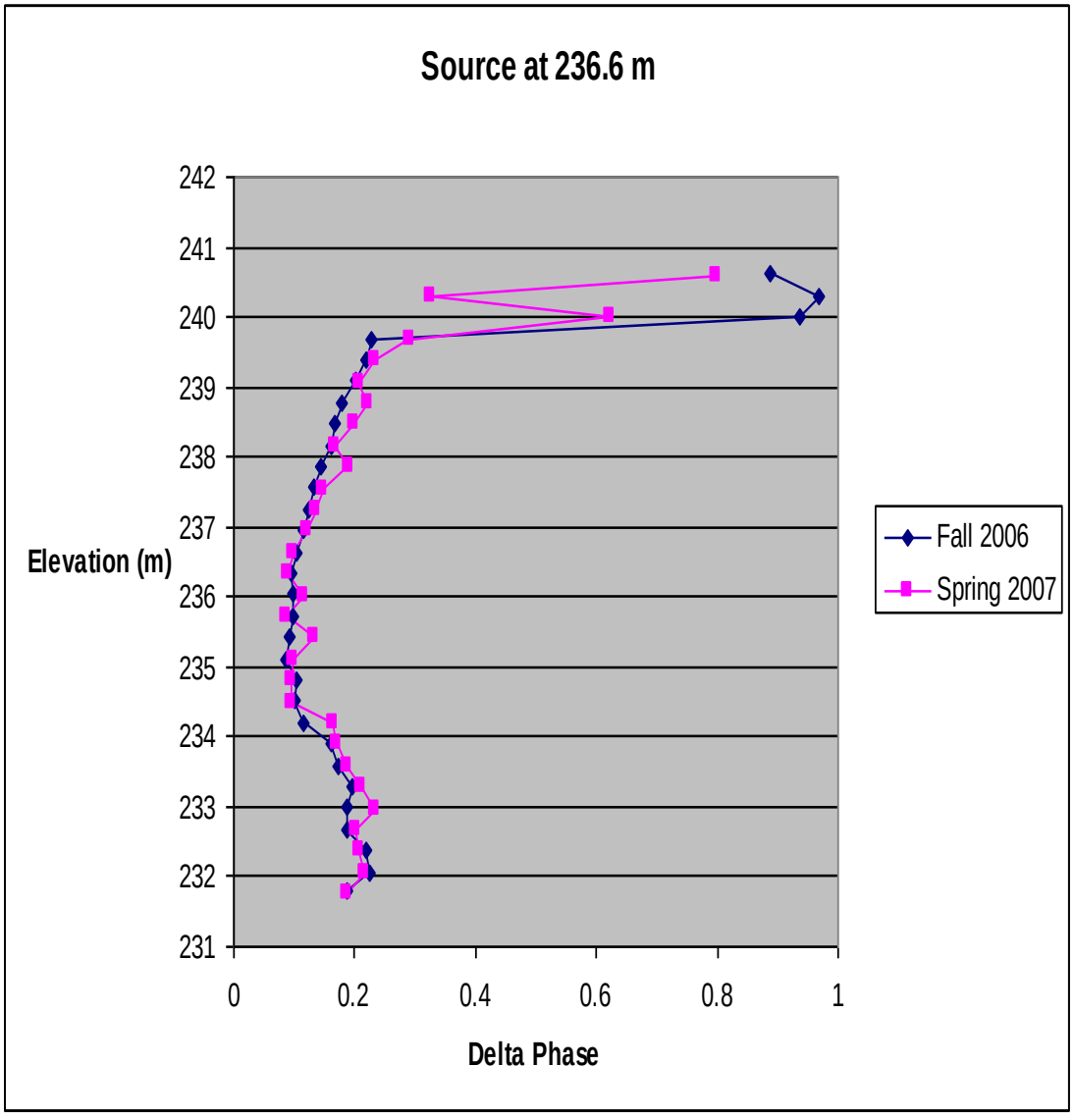

Figure 6: Comparison of fall and spring MOGs from a source elevation of 236.6 m.

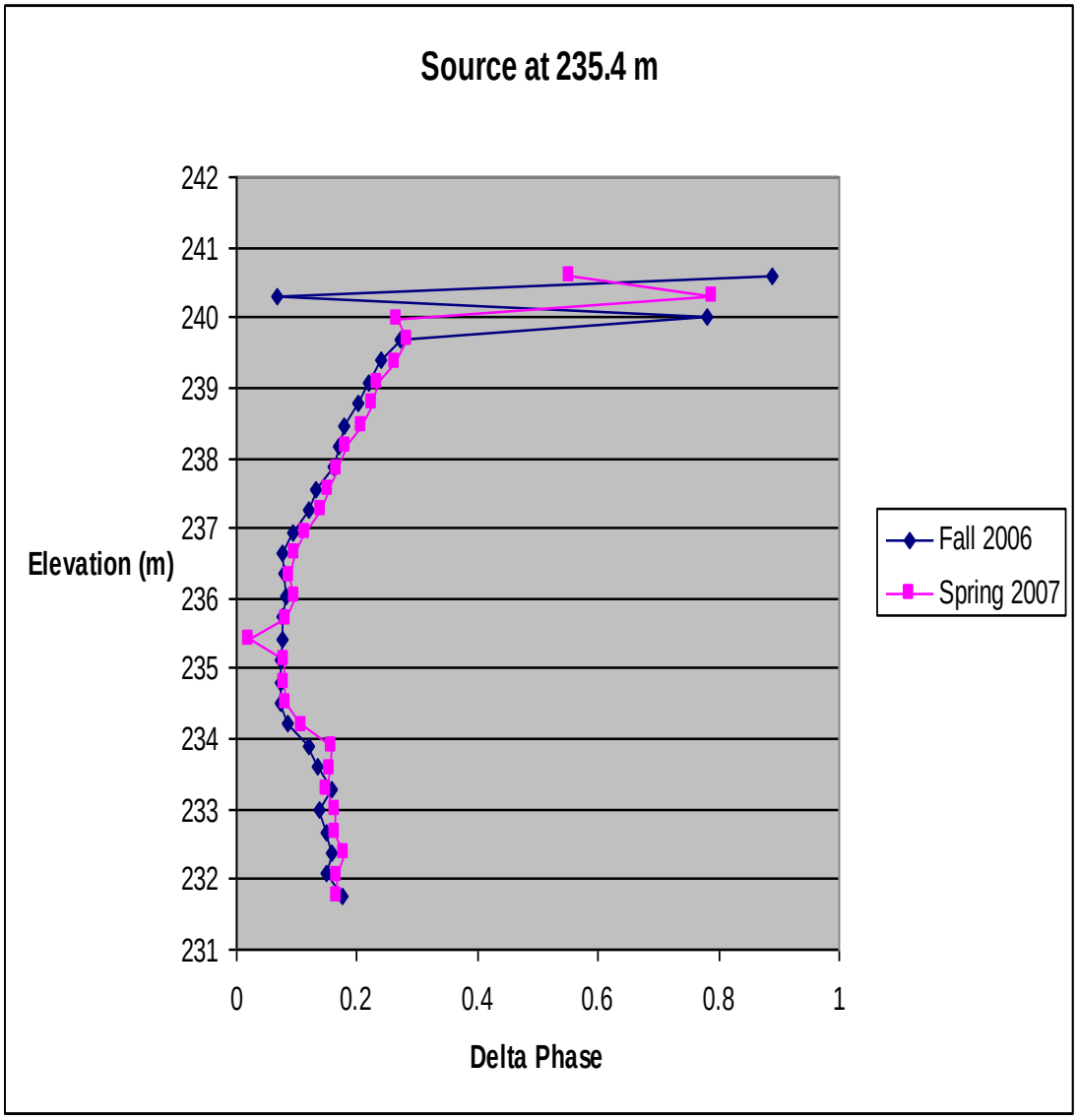

Figure 7: Comparison of fall and spring MOGs from a source elevation of 235.4 m.

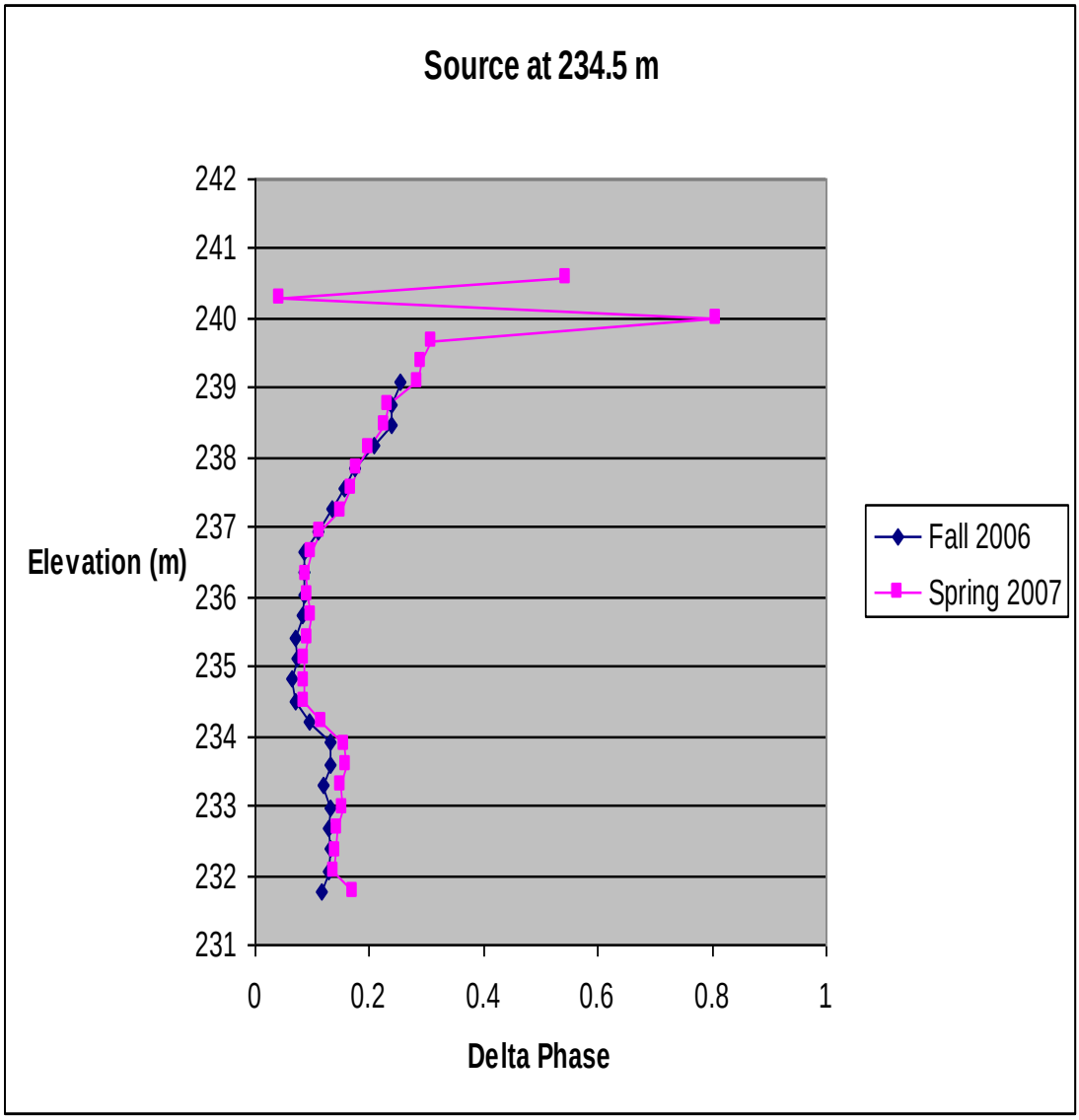

Figure 8: Comparison of fall and spring MOGs from a source elevation of 234.5 m.

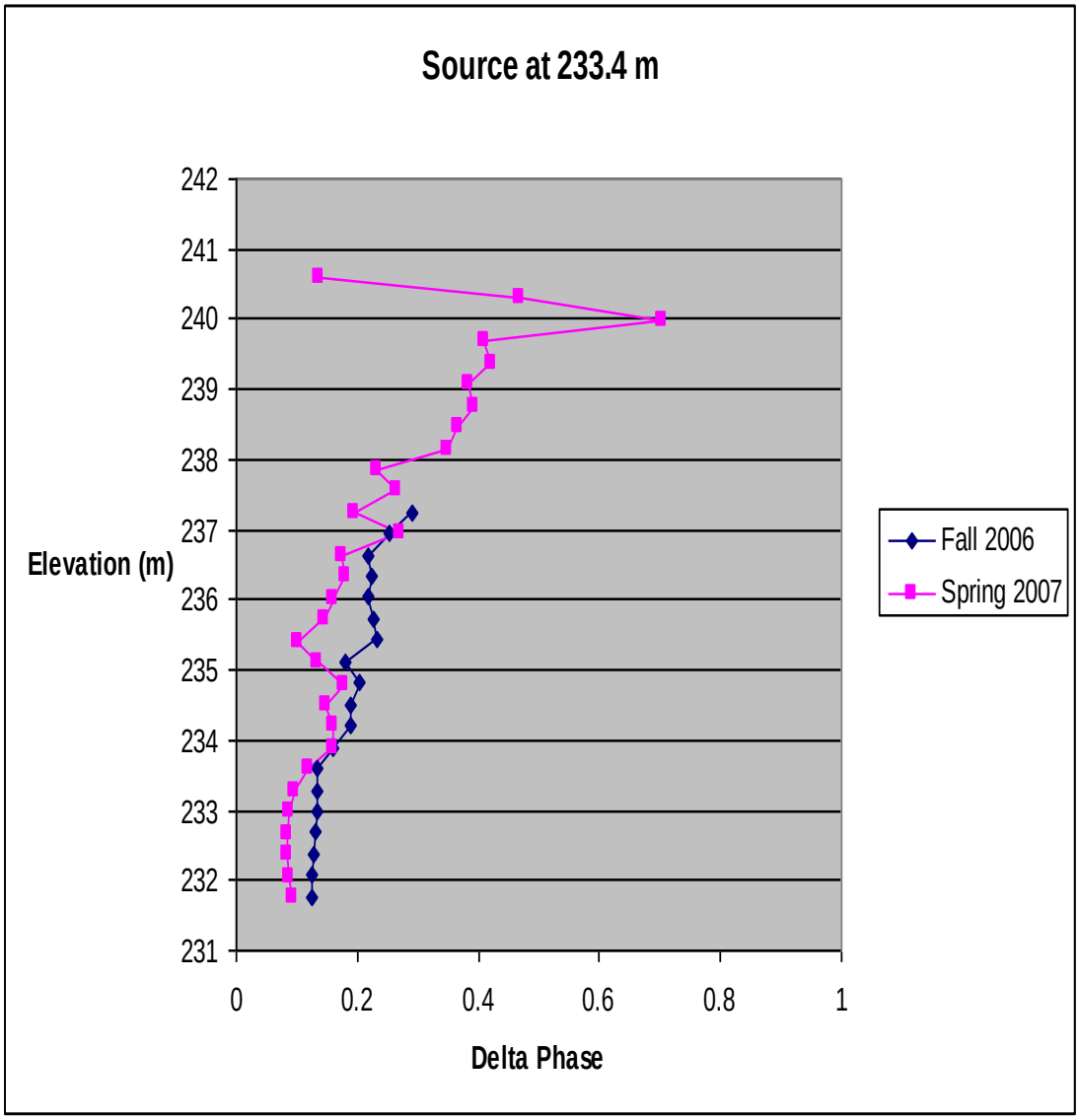

Figure 9: Comparison of fall and spring MOGs from a source elevation of 233.4 m.

The delta phase values between source and receiver from spring 2007 match those taken in fall 2006 closely. The poorer fit in Figure 9 could be caused by a series of nitrogen leaks which began in late spring 2007. The curves are different at

each source location, but the results within any given source location are similar enough to assume that the multi-level receiver is functioning properly.

Early in the summer of 2007, data were collected using the multi-level receiver with HT-3 as the source well and HT-1 as the receiver well, to compare to the MOGs collected the previous year with the single-channel receiver. Shortly after putting the equipment in the wells, a series of nitrogen leaks were discovered in the multi-level receiver. The phase shift values between the source and receiver wells should plot as a parabola due to the path lengths of the rays when the source is centered along the receiver locations.

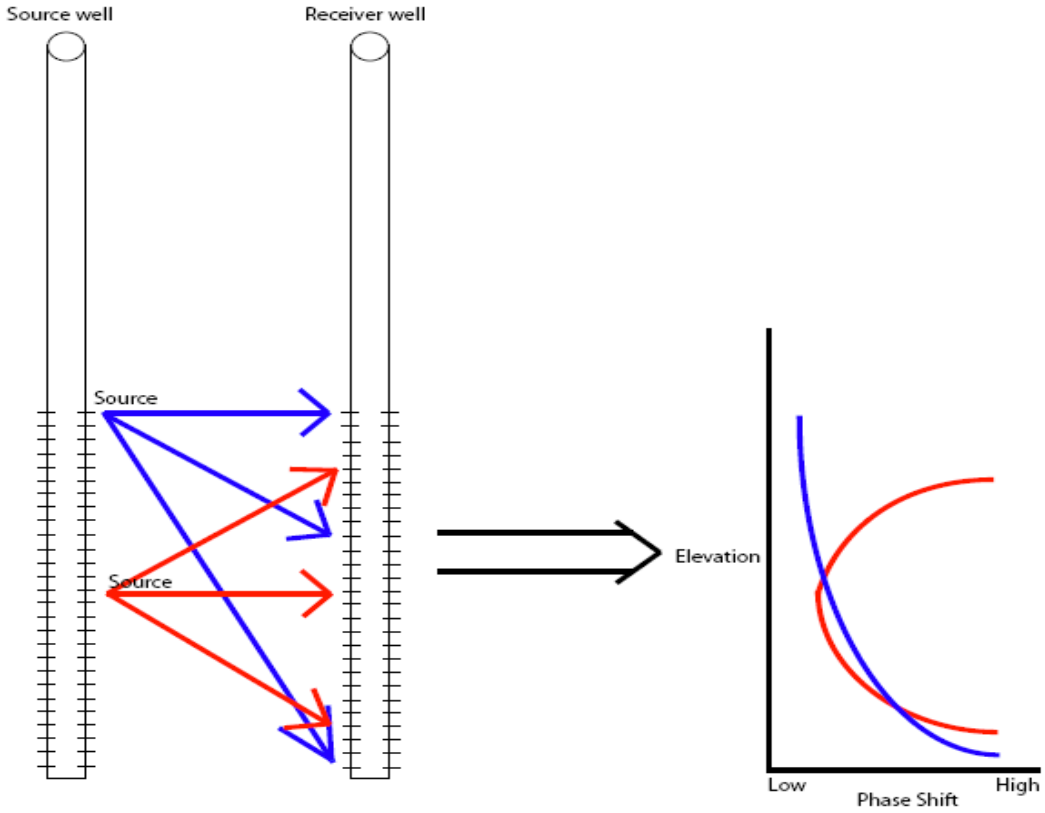

Figure 10: Path lengths are greater for farther offsets. Larger phase and amplitude changes occur at these larger offsets.

If the source is in the middle of the well, the greatest distance and therefore greatest change in amplitude and phase should occur when the receiver is at the top or bottom (Figure 10). The shortest distance is when the source and receiver are at the same depth. When the source is at the top, the shortest distance is to the receiver location at the same depth and the greatest distance is to the receiver location at the bottom of the well. The curve should therefore have a half-parabola shape when the source is at the top of the well. The same is true when the source is at the bottom of the well. The curves produced from the multi-level sensor array with the nitrogen leak showed the overall expected shape but had multiple outliers. In the field, gas could be heard leaking from the receiver and water was being pushed out of the top of the receiver well when the nitrogen was turned on. A full nitrogen tank only lasted for at most two source locations with a complete set of receiver locations. The equipment was pulled from the wells after completing this well pair and taken back to the lab for repairs. Lab tests indicated air leaking from the inflation tube connecting the packers to the nitrogen tank. A short copper inflation tube connects directly to the packers, and this in turn was connected to the plastic inflation tube going to the nitrogen source. The plastic inflation tube was cracked while the copper inflation tube appeared to have no leaks, so additional copper tubing was used in place of the plastic inflation tubes. Some of the brass connections for the copper inflation tubes had cracked, so these were also replaced. The outsides of some packers were leaking at a few places, so clamps were added or replaced as needed to the ends of the packers.

Once the multi-level receiver had been repaired, it was taken back to the field with HT-3 still as the source well and HT-2 now as the receiver well. Ray paths were collected from every source location to every receiver location. No leaks could be heard and no water flowed out from the top of the well. A tank of nitrogen lasted for several source locations compared to at most two source locations before, so data collection became much more efficient. The data showed none of the obvious outliers present before fixing the leaks as shown in Figures 11-13. It is unknown why the HT-3 to HT-1 data showed more scatter in Figure 12 than in Figures 11 or 13.

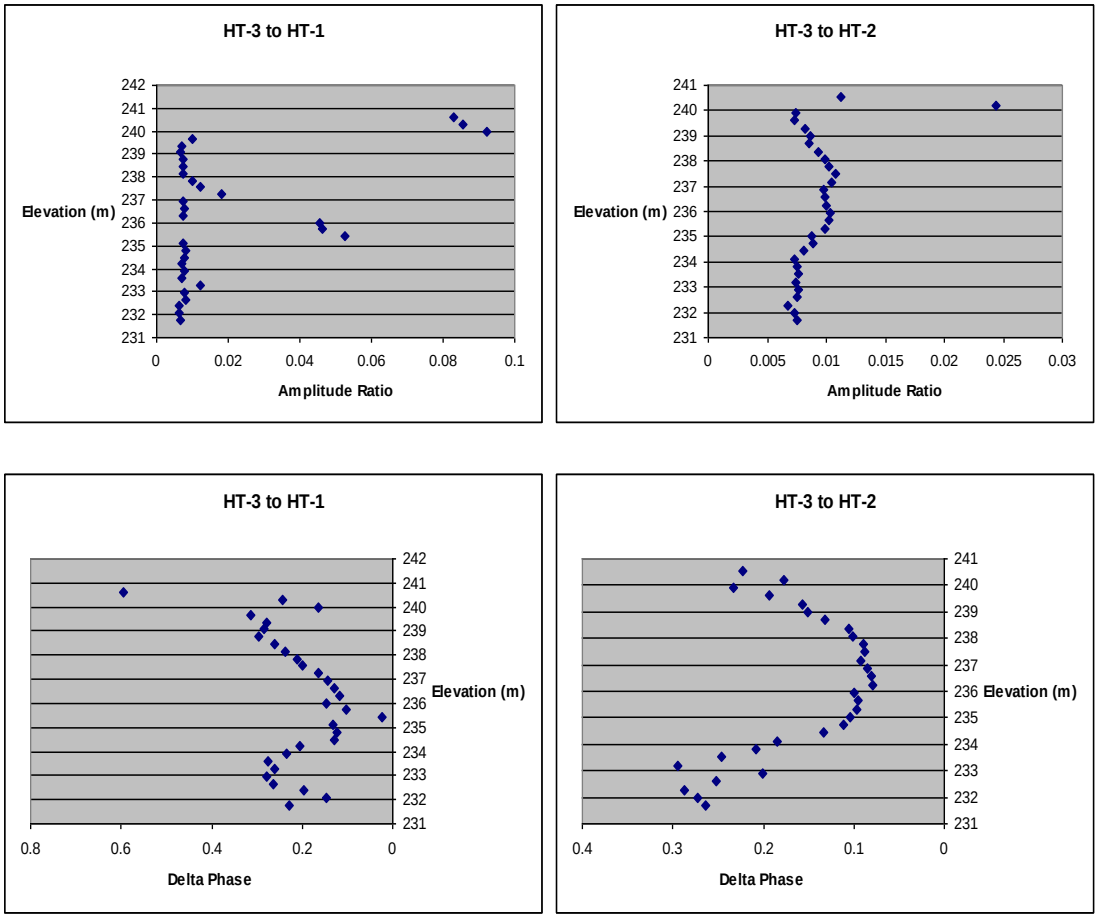

Figure 11: Comparison of parabolas from the middle of the screened interval (source elevation = 236.9 m) before fixing leaks (left) and after (right).

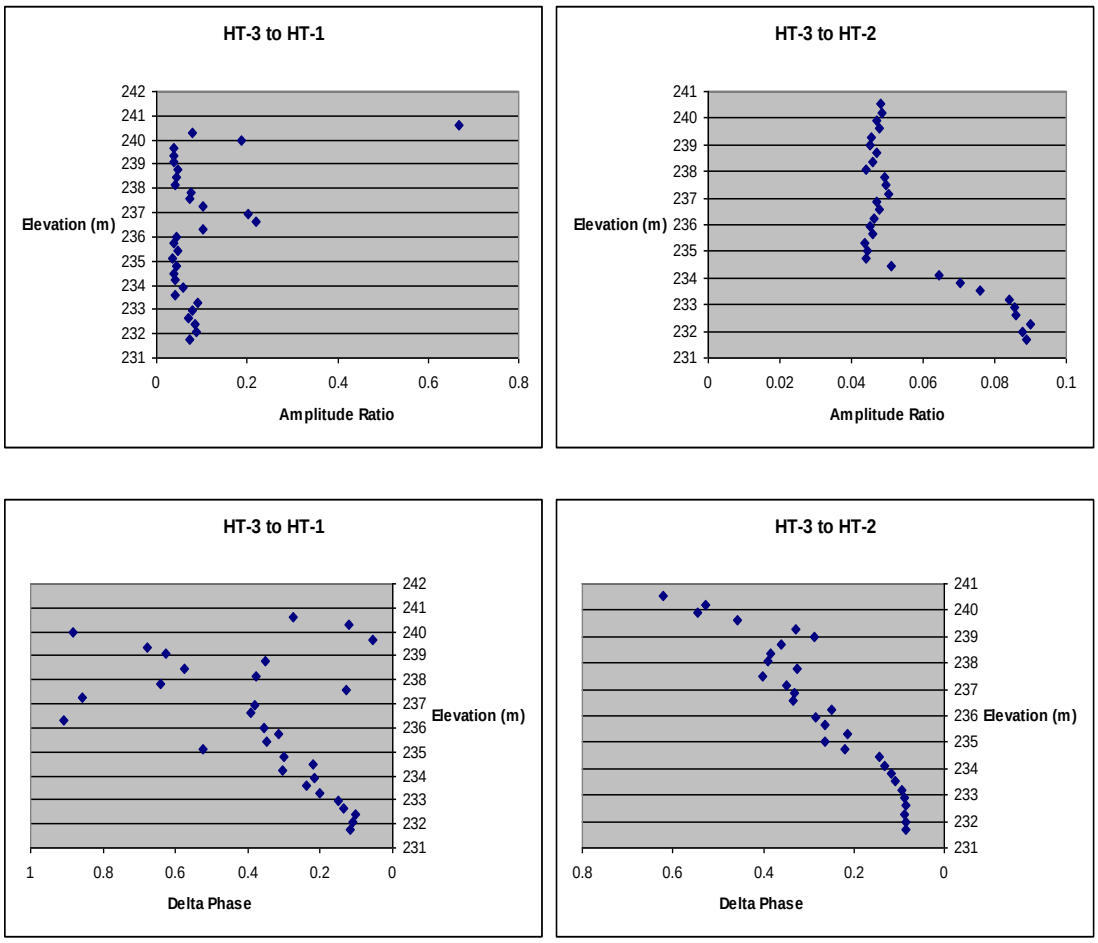

Figure 12: Comparison of half-parabolas from the bottom of the screened interval (source elevation = 232.7 m) before fixing leaks (left) and after (right).

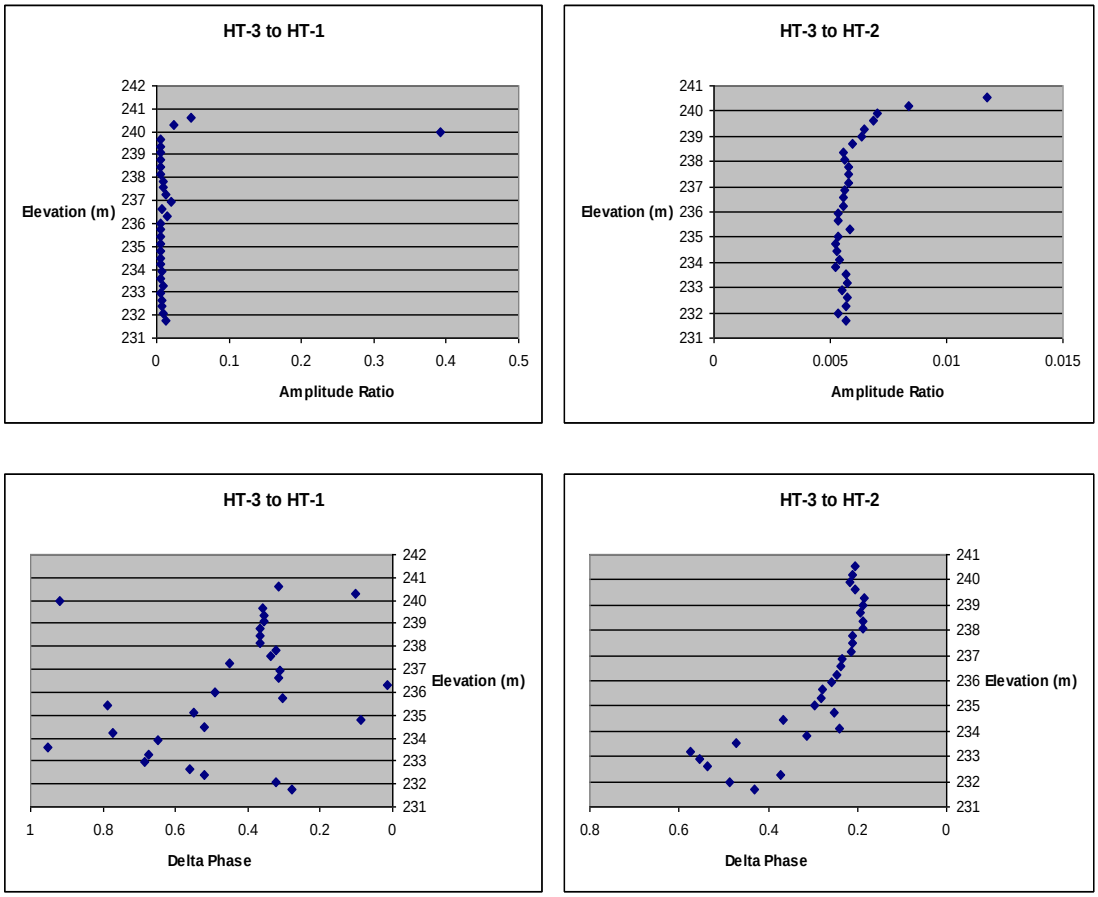

Figure 13: Comparison of half-parabolas from the top of the screened interval (source elevation = 240.0 m) before fixing leaks (left) and after (right).

B. Well Installation and Development

In the fall of 2007, three additional wells were added to GEMS. The wells were installed using the direct push method with a Geoprobe unit from the Kansas Geological Survey. In the direct push method, casing is driven directly into the ground using a combination of hydraulics and percussive force. After one section of casing is pushed into the ground, additional casing is screwed onto the previous section to proceed deeper. Once the desired depth is achieved, the outer casing holds

the hole open while the PVC casing for the well is inserted in the middle of the hole. Each well had the bottom 10.67 m (35 ft) screened with 20 slot screen, meaning that each slot is 20/1000 in (0.000508 m). The advantage of direct push over other drilling methods is that the area around the hole is less disturbed (Thornton et al., 1997). There was a possibility of sand heaving, filling the casing before the screen could be set, but this problem was minimized by filling the casing with water pumped from another well at GEMS while removing the first 6.1 m (20 ft) of drive casing. The water maintained pressure around the PVC casing and kept sand from entering. Once the drive casing had been completely removed, the annulus around the well was first filled in with sand, and then with bentonite.

After installing the wells, they were purged and developed to ensure a proper connection with the aquifer. Total depth measurements indicated that material had flowed into each well, reducing the depth by as much as half a meter. One week after drilling, the wells were developed using a method called air lifting to remove this extra sediment. An air compressor was connected to a hose placed inside the well. Air was channeled through the bottom of the hose and pushes water and sediment out through the top of the well. The hose was dropped to the bottom of the well and then was pulled up in 0.457 m (1.5 ft) increments. The hose was pulled up 24 times for a total of 10.97 m (36 ft) to account for the 10.67 m of screen. A total depth measurement after air lifting the first well indicated that material was still filling in the bottom of the well, possibly due to sediment coming into the well after the hose was raised to shallower locations. The air lifting alone failed to remove all of the

sediment, so a bailer was successfully used to remove the remainder. A bailer is simply a cylinder with a check-valve at the bottom. When dropped in a well, water and sediment fill in the bailer through the bottom. As the bailer is pulled back up, the check-valve closes to hold the water and sediment in place until they can be poured out of the bailer at the surface.

A week after air lifting, the water column in the well was oscillated for one hour per well. The period of the oscillation was within the range of periods used for the MOGs. The oscillation allowed water, and therefore also sediment, to move into and out of the well. After oscillating, total depths were measured and some sediment had again filled in the bottom of the well. The bailer was used for about an hour on each well to remove the excess sediment and achieve the proper total depth.

Following bailing, wells were pumped using a submersible pump. The first well, HT-4, was pumped starting at the top of the screened interval and dropped incrementally to the bottom until the water was mostly clear of sediment; pumping began at the top of the screen in an attempt to avoid sediment clogging the pump. In spite of attempts to avoid clogging, the pump did clog when sitting on the bottom of the well. Air lifting was resumed for 40-50 minute periods at the bottom of each new well to try and remove some of the sediment. Following an unclogging of the pump in the lab, it was taken back out and placed between the top of the screen and the water level. For the first two wells pumped, HT-4 and HT-5, the pump shut off periodically due to problems with the wiring, but each time would restart immediately. Each of these two wells was pumped for 40-45 minutes. Total depth

measurements were taken to ensure that the wells remained clean. When the pump was placed in well HT-6, it shut off after about one minute of pumping but would not restart. High resolution slug tests were performed in the two wells that were successfully pumped and a pump from the Kansas Geological Survey was used to develop well HT-6. Once well HT-6 was successfully pumped, high resolution slug tests were also performed in that well and MOGs were taken with the source in each of the three new wells and the receiver in well HT-3. The receiver was kept in the same well to maximize data collection before winter. The source was moved in 0.914 m (3 ft) intervals for all three source wells, but the receiver interval varied. For the first well, HT-6, the receiver was still moved in 0.305 m (1 ft) intervals. To expedite data collection in wells HT-4 and HT-5, the receiver data collection was in 0.914 m intervals. The different intervals in each well will be compared as to their resolution capabilities. If the larger intervals can provide resolution similar to that from the shorter intervals, then less data are needed in future MOGs at the site.

Once the three new wells had been installed, the elevations of all wells in the study area were surveyed, as was the reference stake. The distances between wells were also measured. The results are presented below in Table 1.

Table 1: Surveying information for wells and distances between wells.

	Elevation (ft)	**Elevation (m)**
Stake	827.556	252.239
HT-1	830.005	252.986
HT-2	829.660	252.880
HT-3	829.705	252.894
HT-4	830.129	253.023
HT-5	829.651	252.878
HT-6	830.272	253.067
7-1	828.342	252.479
11-1	828.358	252.484
Injection well	829.794	252.921

Well	**Well**	**Radius (m)**
HT-3 to	HT-1	4.77
HT-3 to	HT-2	4.36
HT-3 to	HT-4	4.46
HT-3 to	HT-5	4.21
HT-3 to	HT-6	3.99
HT-6 to	7-1	2.70
HT-6 to	11-1	7.19
HT-6 to	Inj. Well	4.04
Inj. Well to	HT-1	4.28
Inj. Well to	HT-4	8.67
Inj. Well to	HT-5	11.55
Inj. Well to	HT-2	11.49
Inj. Well to	HT-3	7.66
7-1 to	HT-2	6.94
7-1 to	HT-5	9.18
7-1 to	HT-3	5.13
7-1 to	HT-4	9
7-1 to	HT-1	6.46
HT-6 to	HT-1	3.79
HT-1 to	HT-4	4.4
HT-4 to	HT-5	4.63
HT-5 to	HT-2	4.57
HT-2 to	HT-6	7.4

C. High Resolution Slug Tests

A slug test gives an average of the hydraulic conductivity values in the vicinity of the well. Traditional slug tests use the entire screened length of the well and therefore provide an average of K values over the vertical extent of the well. HRST provides greater vertical resolution than whole well slug tests because the K value is only averaged over the interval between the packers, which can be as low as 0.075 m (Healey et al., 2004). A slug test is performed by increasing or decreasing the water level and observing the recovery to static water level. The water level change can be achieved by adding or removing water or by adding or removing a solid object from the well. Pneumatic slug testing methods are increasingly being used. The procedure is the same as in the continuous pulse test. The water column can be depressed with air pressure and then allowed to return to its static level.

The high resolution slug testing (HRST) uses some of the same equipment as the MOGs, but is modified for a different type of experiment. A nitrogen-inflated double packer system is used to isolate a small portion of the well. A pump or vacuum is connected to the well to either lower or raise the water level. Pressure transducers were used to measure both the air pressure and the water pressure. At each location, the initial head conditions used were +2.44, -2.44, +1.22, and -2.44 m (+8, -8, +4, -8 ft) of head. After making these initial head adjustments, a valve was opened to release extra pressure and start the slug test. There were 30 locations measured in each well to span the length of the screened interval.

D. Data Processing

Data processing for the single-level receiver was done with FitAmpPhaseV8, a program written in Visual Basic by Carl McElwee. The program fits sine waves to the transducer data taken in the field and generates plots of the amplitude ratio and phase shift (x-axis) between the source and receiver transducers. All of the values are plotted against location (y-axis). The program analyzes data for a single source location at a time. A fixed value of 10^{-5} was used for S_s based on the literature (Fetter, 2001) and a calculation using equation (8) from the Introduction (Engard, 2006). It is necessary to use a calculated value because of the difficulty measuring S_s in situ. For each MOG, the amplitude ratio and phase shift between the two source transducers should plot as a vertical line, as there is no change in material within the well itself. As stated previously in the Field Methods section, the amplitude ratio and phase shift between the source and receiver should both plot as nearly parabolas or half-parabolas. If the source location is near the middle of the well, the shape will be a full parabola, and the shape will only be half a parabola if the source is near either the top or bottom of the well. The shape should be perfectly parabolic assuming no change in aquifer material, so any deviations from the overall parabola must be due to changes in K.

Data processing for the multi-level receiver was done with FitAmpPhaseV10HT, another program developed by Carl McElwee in Microsoft Excel using Visual Basic. This version of the program analyzes all five receiver transducers at once. Aside from accounting for multiple receiver transducers, the

program is based on the same algorithms as FitAmpPhaseV8. Plots are generated for the receiver location versus both amplitude and phase shift. The raw data and the fitted sine wave for a single receiver location are shown below in Figure 14.

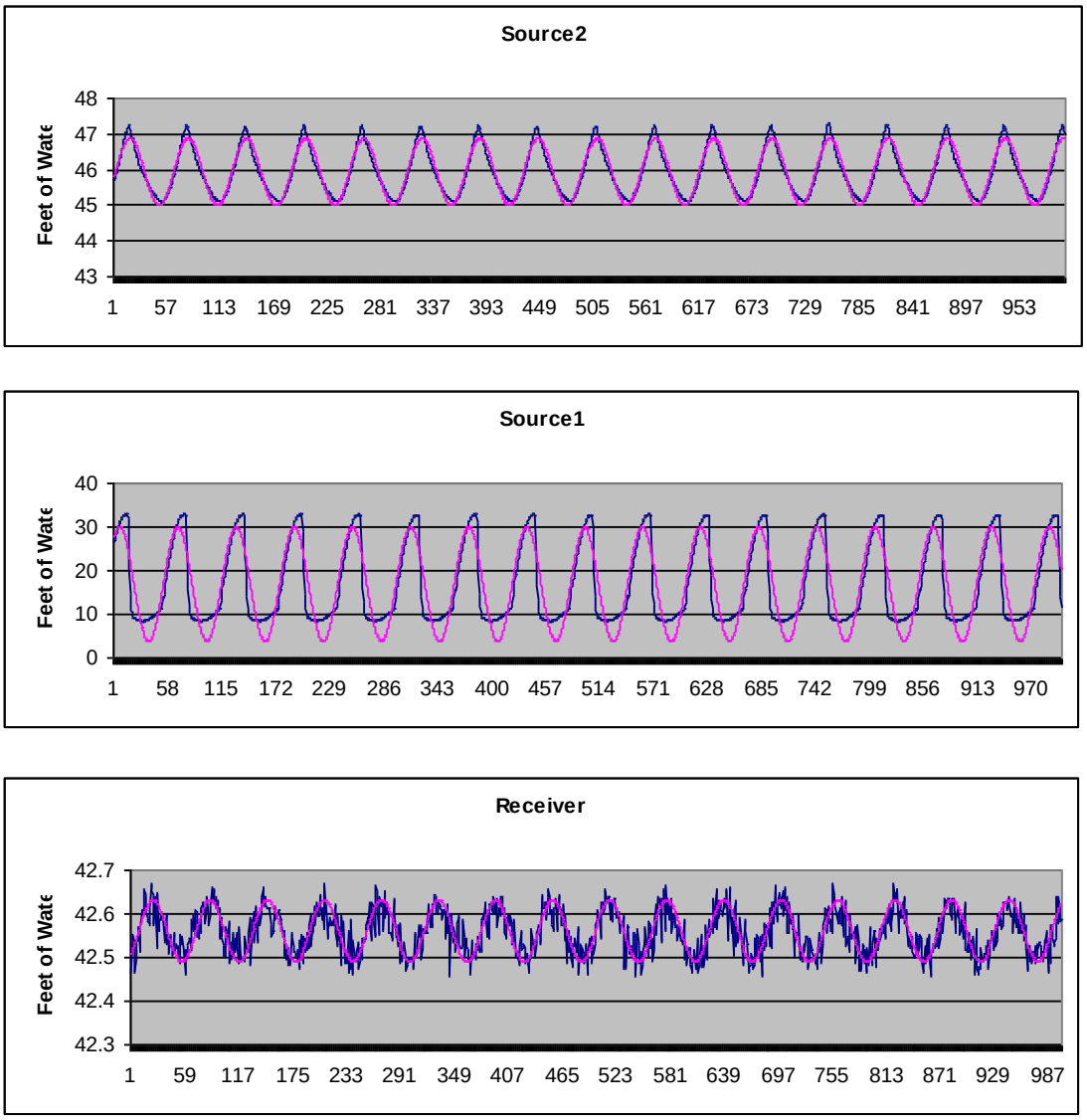

Figure 14: The data for one particular receiver location in the FitAmpPhaseV10HT program. Three plots are shown: one plot for each of the two source transducers and one plot for a receiver transducer. The raw data are shown in blue while the fitted sine wave is shown in pink.

HRST data were processed using the program NLSLUG (McElwee, 2000), developed by Carl McElwee using Fortran and run from Microsoft Excel. The values from the water and air pressure transducers must be added together before beginning the program. The pressure transducer in the well reads total pressure and should show little change as the initial height is established without adding in the air pressure. For each record, a time break is chosen to begin measuring time, and static values at long times are subtracted from all head values in order to center the records of differing initial heads at a static value of zero. The time break serves as time zero so that each record starts at the same time. The point for the time break is chosen by examining the head values and choosing the last point of induced initial head before it begins to decrease due to initiation of the test. If the results are independent of head and behave linearly, all four records will lie on top of each other. If the results are independent of direction and repeatable, the records from three initial head conditions (+2.44, -2.44, -2.44 m) should lie on top of each other. Usually the records do not line up, so there can be problems with both directionality, i.e. positive or negative initial head, and repeatability. Mobile fine sediments could explain both problems (McElwee and Zemansky, 2005). Slug testing can cause fine sediments to be moved, and these sediments may move more easily into the well than away from the well, creating an annulus containing more fine material at some radius. HRST data for the wells in this study were processed by Brett Engard and Pema Deki (Appendix A, Figures 58-63). The HRST results can be used to constrain the inversion to ensure that the interwell K values remain in the range observed in HRST results.

E. Modeling

Typical hydraulic tomography inversions use nonlinear least squares fitting and iterations to get the best fit, a process that can take a great deal of time and computing power. The procedure used for this paper uses spatially weighted ray paths. The path length in each zone of differing K is multiplied by a coefficient involving K to get the phase. Ray path data were generated by Hydraulic TomAnalV19, developed by Carl McElwee in Microsoft Excel. The field area was divided into a grid system with approximately evenly spaced divisions in the horizontal and vertical directions. Each box within the grid is referred to as an element. The model was divided into a series of nodes, elements, and grid spaces (Figure 15).

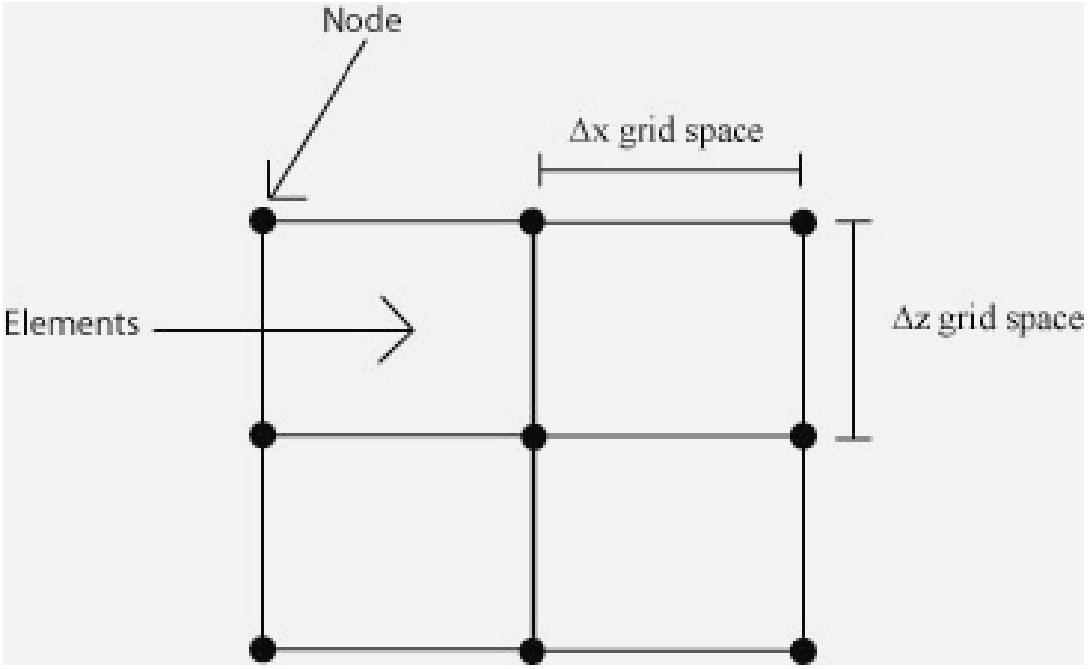

Figure 15: Depiction of a node, an element, and a grid space.

Nodes are any of the individual points throughout the grid. The vertical or horizontal spaces between two nodes, Δx and Δz, are known as grid spacing. An element is the rectangular area enclosed by four adjacent node points. The program computes the distance of each ray path through every element based on the Pythagorean Theorem. The path lengths through each element and the phase shift values are then transferred to the LeastSquareSVDV13 program, developed by Carl McElwee in Microsoft Excel. The SVD, or Singular Value Decomposition, program performs a least squares fitting inversion from phase values to K values using a set of linear equations (Aster et al., 2005). Equations used in the program do not require iterations because they are linear. The SVD method divides G, an *m* (number of ray paths and equations) by *n* (number of zones and unknowns) matrix into the following equation:

$$G = UWV^T \qquad (16)$$

where U is an *m* by *m* orthogonal matrix, W is an *m* by *n* matrix with nonnegative diagonal elements known as singular values, V is an *n* by *n* orthogonal matrix, and the T superscript indicates that V is a transpose matrix.

Modeling studies were performed to compare results from the spatially weighted ray tracing method with those from a numerical model. The first model used was one with 99 ray paths and three layers each with a thickness of 3.66 m (12 ft). K values were chosen as 0.00182 m (0.006 ft/s) for the top and bottom layers and 0.000908 m/s (0.003 ft/s) for the middle layer. The K values chosen approximate those found in the sandy region of GEMS. Deviation between the two curves occurs at the lower boundary between layers and at the upper boundary due to boundary

effects. The numerical model uses a barrier boundary rather than assuming an infinite solution, so the boundary effects are expected. Aside from the slight deviations at the boundary, the two curves are very similar (Figure 16). The good agreement between the numerical model and the spatially weighted ray trace method are one line of evidence supporting the transformation made back in equation 15.

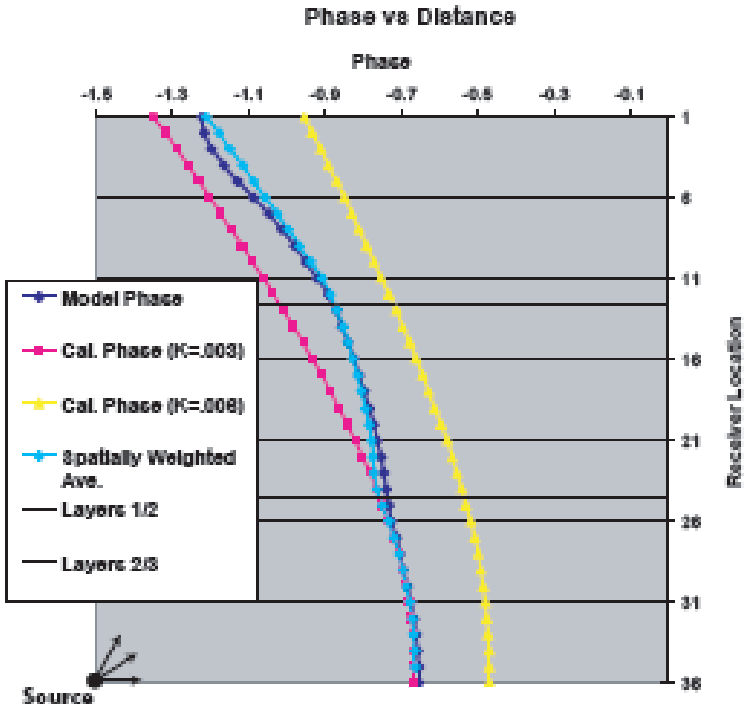

Figure 16: A comparison of phase values using a numerical model (model phase), two homogeneous analytical solutions, and the spatially weighted ray trace average for three equally sized layers.

After examining the case of three equal layers, the middle layer was collapsed to examine the resolution of the model (Figure 17). The middle layer was reduced to 0.914 m (3 ft), with the same K values mentioned in the previous example. K values

were obtained using the SVD program. Once again, the spatially weighted ray trace method was in good agreement with the numerical model except for some boundary effects. The error in K for the spatially weighted ray trace method was 2.7% for the middle layer and less than 1.5% for the other two layers.

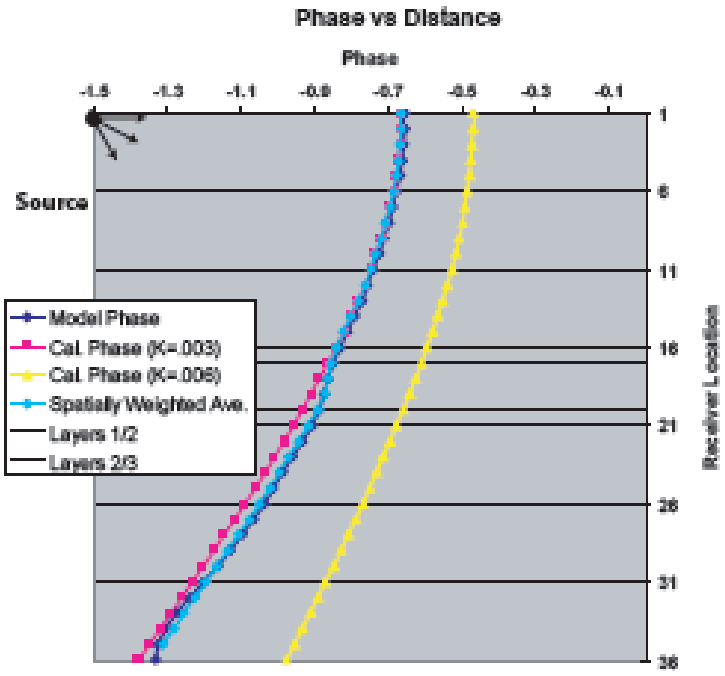

Figure 17: A comparison of phase values using a numerical model (model phase), two homogeneous analytical solutions, and the spatially weighted ray trace average for a thin middle layer.

After verifying that the model could resolve layers of about a meter in thickness, random error of up to +/- 5% was added to the phase data to approximate noise that would be present in field data. Five trials were run with different amounts of error each time. The average error in K for the thin middle layer was 13.4%, while

it remained less than 1.5% for the two thicker layers. The results indicate that layers of about one meter thickness can be resolved.

Theoretical values of phase and amplitude for more complex models were run through data processing programs before applying the programs to field data. The synthetic data set had no error built in. A model was set up with 6 grid spaces in the x direction and 10 grid spaces in the z direction, with 100 rays going through those 60 elements. The x distance was 19.2 feet and the z distance was 30 feet. K values were once again chosen as 0.00182 m (0.006 ft/s) for the top and bottom layers and 0.000908 m/s (0.003 ft/s) for the middle layer, with the middle layer being the smallest layer. The value used for S_s was 0.00018. Instability problems resulted due to a difference in ray path density. The ray path density was highest in the center of the region, so there was less resolution at the top and bottom of the modeled area. The problem can be avoided by having spatially variable element sizes across the model. The top row of elements was combined into a single element and the bottom row was also combined into a single element, reducing the 60 element model to a 50 element model shown below in Figure 18. After combining the elements in those two rows, the model became stable and the remaining section could still be resolved into blocks of about one meter on each side. The standard deviations on the K values were between 10^{-16} and 10^{-18}, implying that the inversion was almost perfect for the data with no noise.

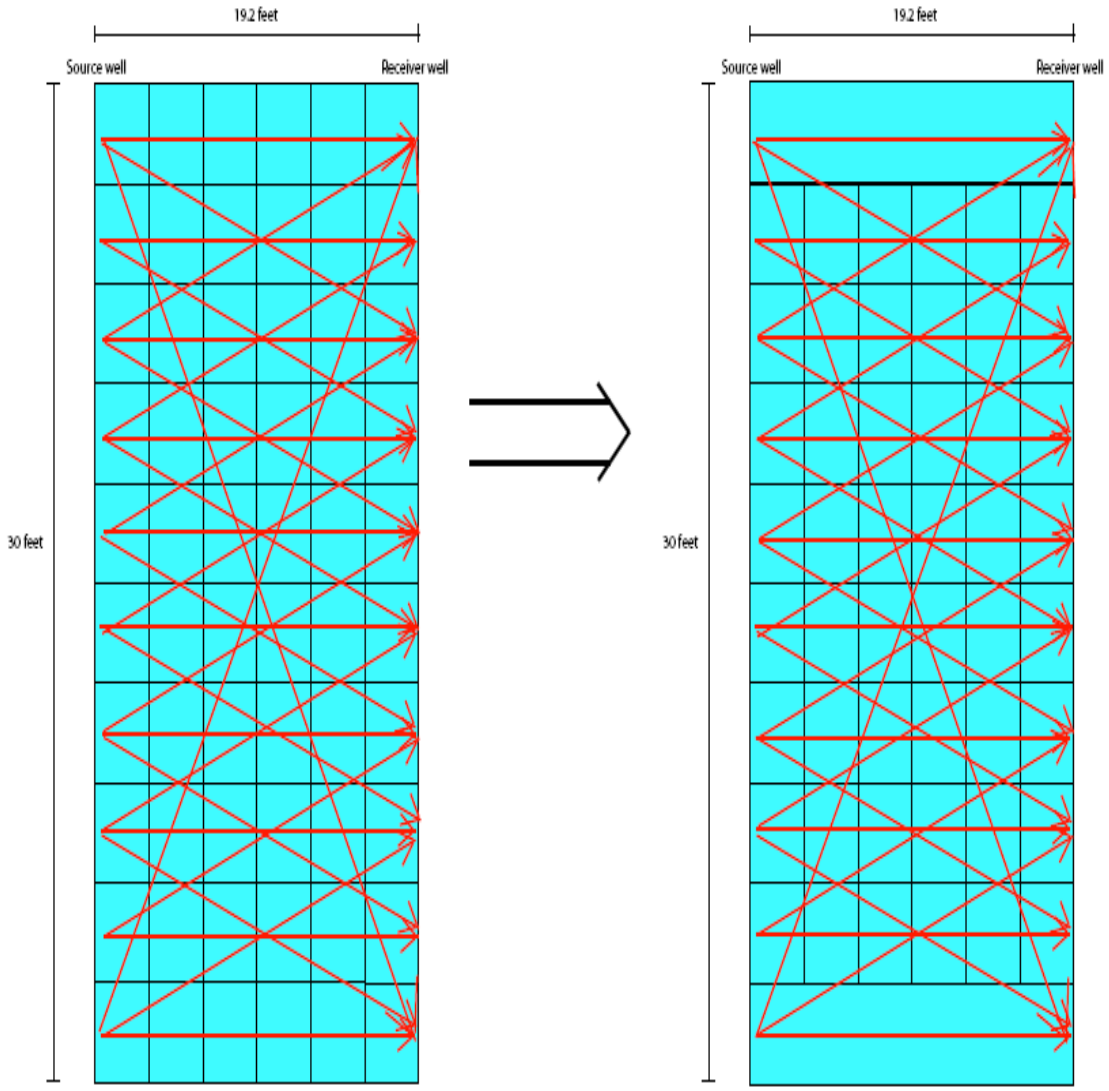

Figure 18: The 60 element model on the left was reduced to the 50 element model on the right to fix instability issues. Rays shown are conceptual and only represent a small portion of the total number of ray paths used.

Using a random number generator, values within the range of +/- 0.05 were added to the phase values. This translates to an error of +/- 5%, since the phase varies from 0 to 1. The 50 element model was again used since it had proven stable for the idealized data set. The model was unstable in each of five random error trials, with

no consistent trend as to the location or magnitude of the unreasonable K values from the inversion. The model will continue to be refined to increase stability.

The model was also initially unstable when using the program on field data. The grid dimensions were slightly different than those of the theoretical data, but all sides of each element were still roughly one meter. This 36 element model used for the field data had 5 elements in the x direction and 9 elements in the z direction. The top row of elements was combined into a single element, and the bottom row was also combined into a single element. Instability problems still persisted, so the second row from the top and the second row from the bottom were each combined into single elements, as illustrated in Figure 19. After combining the first and last two rows, the model became stable and the remaining section could still be resolved into blocks of about one meter on each side, although a few K values were still outside of the range for GEMS as determined by previous studies. The anomalous K values necessitated additional modeling to increase stability and accuracy.

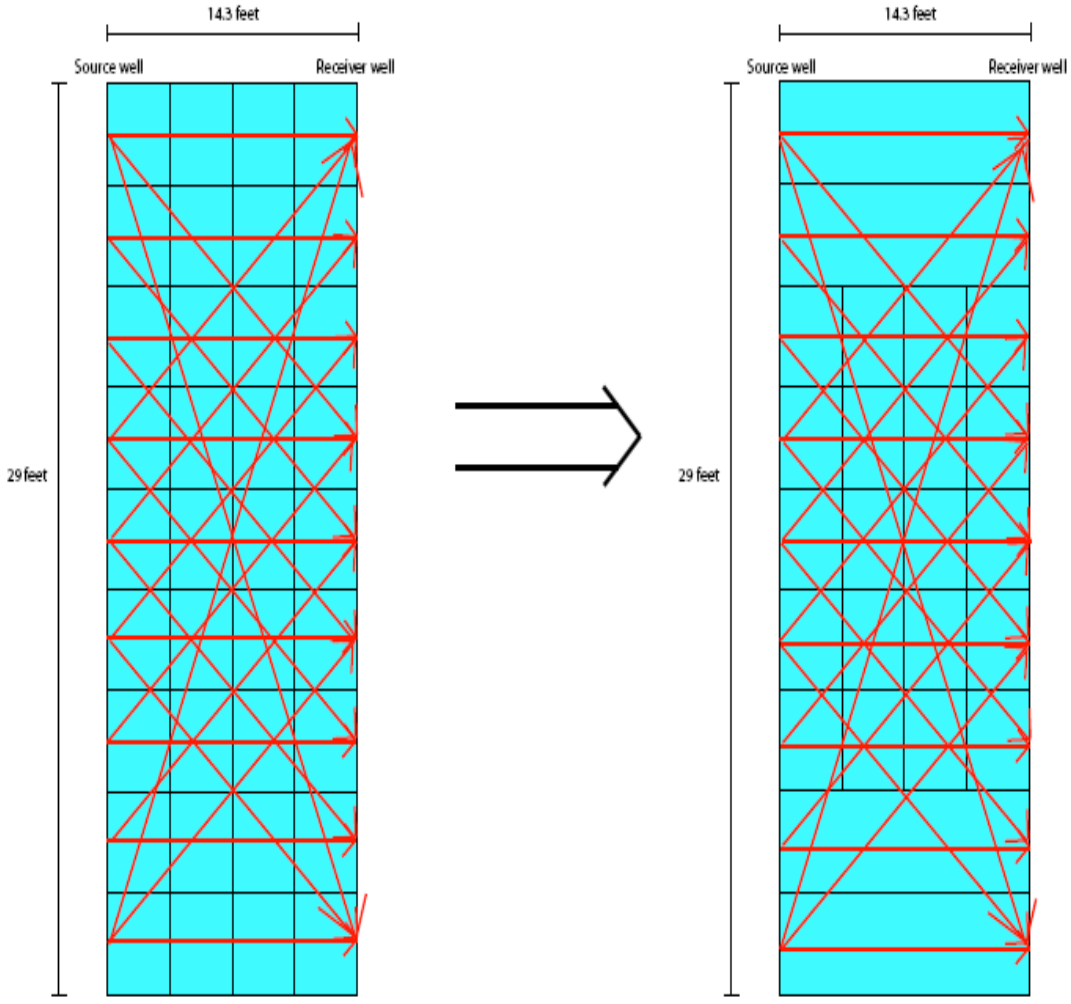

Figure 19: The 36 element model on the left becomes stable when reducing it to the 24 element model on the right. Rays shown are conceptual and only represent a small portion of the total number of ray paths used.

The Hydraulic Tomography Analysis program was updated so that K could be specified by nodes rather than just by elements. Models were run to determine the optimal grid layout. The latest versions of the processing programs offer the ability to specify K by zones, which are formed by one or more nodes or elements and must be input manually. The purpose of the zones is to provide variable resolution across

the model, with finer zones towards the center and coarser zones at the edges of the grid where fewer rays are crossing. The current version of the SVD program also has the ability to perform Monte Carlo simulations, rather than running individual simulations for random error. The Monte Carlo simulations were run with both +/- 1% and +/- 5% noise for 1000 simulations. 1% random noise more closely approximates the expected variation in the field due to instrument precision and noise, but the 5% trial is run to demonstrate how the model performs under the worst possible noise. The variables investigated were: the number of nodes in the X direction (either 6 or 7), whether K was specified by elements or nodes, and the number of zones. The different combinations of input parameters resulted in a total of 16 different models. All initial models used 100 ray paths, consisting of 10 source locations and 10 receiver locations, and an S_s value of 0.00018. K values were arbitrarily chosen to start at 0.000914 m/s (0.003 ft/s) in zone 1 and gradually increased with depth to 0.00213 m/s (0.007 ft/s) in zone 16. Although the K values were arbitrarily chosen for the modeling phase, they all fall within the range observed at the site (0.000305 m/s to 0.00305 m/s) from HRST and other methods. The results of the modeling studies are presented in Table 2 below in order of increasing average error based on 1% random noise:

Table 2: Maximum and average error in K for a series of model input parameters (S_s = 0.00018) for two amounts of random noise.

K determined by	**# of X nodes**	**# of Zones**	**Max error - 1% noise**	**Avg. error - 1% noise**	**Max error - 5% noise**	**Avg. error - 5% noise**
elements	6	16	2.80	1.57	14.10	7.97
nodes	7	15	3.65	1.73	18.96	8.79
elements	6	20	2.67	1.75	14.18	9.12
elements	7	26	6.19	2.95	38.61	15.84
nodes	6	20	5.13	3.01	28.04	15.64
nodes	7	23	6.19	3.32	34.12	17.87
elements	7	24	10.11	3.58	103.08	21.60
elements	7	34	10.78	5.26	121.94	34.03
nodes	7	25	11.98	5.61	325.62	51.41
nodes	6	26	23.36	9.34	3156.65	406.65
nodes	6	24	22.98	9.72	3065.35	514.80
elements	6	34	18.52	10.29	2898.41	701.16
elements	7	52	41.37	17.49	3160.57	1465.70
elements	6	42	80.92	31.18	3145.44	1610.62
nodes	6	30	2868.10	1331.84	3160.65	2046.83
nodes	7	37	3159.82	1700.53	3145.48	1942.04

The Hydraulic Tomography Analysis program calculates the length of each ray path through a particular element or nearby a given node. The total amount of length through each element or associated with each node was calculated by adding the lengths from each individual ray path of the 100 rays used. The ray path sums give a measure of the sensitivity of a given model to the K value in an element or near a node. These sums are presented below:

Table 3: Grid layout of ray path length sums in each element for four models used ($\Delta x = 4.36$ m, $\Delta z = 8.84$ m).

7 x 11 nodes (60 elements)

Elements

10.11	8.12	6.44	6.44	8.12	10.11
21.78	29.45	20.86	20.86	29.45	21.78
20.64	48.58	36.99	36.99	48.58	20.64
20.60	51.32	55.49	55.49	51.32	20.60
20.47	49.73	67.43	67.43	49.73	20.47
20.47	49.73	67.43	67.43	49.73	20.47
20.60	51.32	55.49	55.49	51.32	20.60
20.64	48.58	36.99	36.99	48.58	20.64
21.78	29.45	20.86	20.86	29.45	21.78
10.11	8.12	6.44	6.44	8.12	10.11

Nodes

0.00	4.13	2.16	1.78	2.16	4.13	0.00
0.00	27.62	15.47	13.45	15.47	27.62	0.00
0.00	43.33	33.24	27.95	33.24	43.33	0.00
0.00	45.70	49.68	44.86	49.68	45.70	0.00
0.00	44.45	57.43	63.04	57.43	44.45	0.00
0.00	43.94	58.43	72.23	58.43	43.94	0.00
0.00	44.45	57.43	63.04	57.43	44.45	0.00
0.00	45.70	49.68	44.86	49.68	45.70	0.00
0.00	43.33	33.24	27.95	33.24	43.33	0.00
0.00	27.62	15.47	13.45	15.47	27.62	0.00
0.00	4.13	2.16	1.78	2.16	4.13	0.00

6 x 11 nodes (50 elements)

Elements

10.22	8.73	7.73	8.73	10.22
24.86	31.02	23.90	31.02	24.86
26.56	53.88	42.95	53.88	26.56
25.64	65.29	64.59	65.29	25.64
25.04	65.72	85.47	65.72	25.04
25.04	65.72	85.47	65.72	25.04
25.64	65.29	64.59	65.29	25.64
26.56	53.88	42.95	53.88	26.56
24.86	31.02	23.90	31.02	24.86
10.22	8.73	7.73	8.73	10.22

Nodes

0.00	4.33	2.35	2.35	4.33	0.00
0.00	29.39	17.12	17.12	29.39	0.00
0.00	49.92	36.20	36.20	49.92	0.00
0.00	56.73	56.82	56.82	56.73	0.00
0.00	56.41	72.84	72.84	56.41	0.00
0.00	55.75	78.63	78.63	55.75	0.00
0.00	56.41	72.84	72.84	56.41	0.00
0.00	56.73	56.82	56.82	56.73	0.00
0.00	49.92	36.20	36.20	49.92	0.00
0.00	29.39	17.12	17.12	29.39	0.00
0.00	4.33	2.35	2.35	4.33	0.00

The sums are extremely small in the top and bottom rows, particularly for models where K is assigned to nodes. In the node cases, taking the whole first or last row as a zone still results in very small zone sums. The model was bounded by constant K nodes at each well based on HRST results. These constant values do not contribute to the ray path sums, as indicated by the zeroes in the left and right columns in the node examples.

Ultimately, the results based on 5% random noise were not taken into consideration because, as stated previously, this was likely much higher than the

amount of noise in the field data. The amount of error produced by a given set of input parameters had to be balanced with the amount of resolution provided by that particular model. Increasing the number of zones increases the resolution, but only at the cost of increased error. The best compromise of error and resolution seems to occur somewhere in the middle of Table 2. Good resolution can be obtained with either 6 or 7 nodes in the X direction. For models with a comparable number of zones, there is less error when K is determined by elements. The 50 element model with 16 zones resulted in the least amount of error of the models studied here, but some of the models with more zones also produced acceptable amounts of error. The 34 zone model provides a good compromise between error and resolution for the 60 element cases, while the 20 zone model provides a good compromise for the 50 element cases.

The 34 zone, 60 element model and the 20 zone, 50 element model discussed above produced too much error and instability when applied to the field data from the wells in this study. One possible cause was that the distance between wells was slightly smaller in field data than in the modeled data. The problem was first investigated by using a model with only 5 nodes in the X direction, producing a 40 element model with 16 zones. Results were similar to those obtained with 50 elements with a comparable number of zones. The second variable investigated was S_s. Initial theoretical models used 0.00018 for S_s but changing to a more field appropriate value of 0.00001 resulted in consistent increases in the amount of error, as shown in Table 4. A good balance of error and resolution when S_s equaled

0.00001 was achieved with a 16 zone, 50 element model (6 X nodes). The average error was 7.79% in the presence of 1% noise. The 16 zone model with 6 X nodes will be used in all following discussions.

Table 4: Maximum and average error in K for a series of model input parameters ($S_s = 10^{-5}$) for two amounts of random noise.

K determined by	**# of X nodes**	**Zones**	**Max error - 1% noise**	**Avg. error - 1% noise**	**Max error - 5% noise**	**Avg. error - 5% noise**
elements	6	8	4.48	3.52	23.35	18.61
elements	6	10	8.83	4.96	66.94	30.25
elements	6	12	8.91	5.18	63.43	31.03
elements	6	14	12.32	7.11	489.26	128.90
elements	6	16	13.84	7.79	2975.59	533.84
elements	6	20	12.89	8.76	2876.63	381.94
elements	5	16	18.61	8.87	3087.28	664.41
elements	5	18	11.00	8.88	564.10	99.57
elements	4	16	15.19	9.92	3095.25	695.15
elements	5	22	23.02	13.70	3155.61	1277.53
elements	5	20	24.74	13.93	3160.06	1399.58
elements	5	26	25.50	14.63	3160.68	1265.16
nodes	6	20	25.38	14.87	3034.25	1377.35
elements	7	26	34.91	15.64	3153.50	1105.79

Similar to the sums presented by elements and nodes previously, the sum of ray path lengths going through each zone of the chosen model for the suite of rays used was also calculated. The grid layout is shown in Figure 20 and the zone sums for each well pair (each with a different radius) are presented in Figure 21.

46	47	48	49	50
41	42	43	44	45
36	37	38	39	40
31	32	33	34	35
26	27	28	29	30
21	22	23	24	25
16	17	18	19	20
11	12	13	14	15
6	7	8	9	10
1	2	3	4	5

Figure 20: The grid shows the division of elements into 16 zones.

In Figure 20, each of the 50 elements is numbered, with element 1 at the bottom of the source well and element 50 at the top of the receiver well. The greatest resolution is provided in the middle of the grid while the top and bottom have the least resolution. The zone sums presented below in Figure 21 were calculated using field geometry and the actual number of rays collected in the field for each well pair, and they represent a measure of the sensitivity of the model to the K value in each zone.

(a). HT-3 to HT-2 (750 rays)

823.77		
1228.00		
630.15	405.42	537.70
667.15	548.02	523.73
664.30	546.10	526.06
616.21	404.27	545.03
1213.79		
820.19		

(b). HT-3 to HT-1 (780 rays)

1154.96		
1434.27		
691.30	472.55	597.74
707.20	612.89	585.77
704.63	580.72	591.74
651.07	416.50	605.51
1278.80		
807.51		

(c). HT-4 to HT-3 (100 rays)

139.51		
166.25		
75.58	52.77	75.72
75.27	72.18	75.30
75.07	73.41	75.05
75.94	54.72	75.81
170.54		
152.43		

(d). HT-5 to HT-3 (190 rays)

143.02		
211.02		
150.46	71.51	75.04
148.99	124.07	102.38
140.86	144.98	160.69
136.40	123.90	199.25
403.52		
362.43		

(e). HT-6 to HT-3 (300 rays)

361.10		
454.76		
209.34	143.64	214.51
211.15	202.04	212.24
211.16	210.42	209.94
216.29	158.90	211.12
487.74		
456.77		

Figure 21: The sums of ray paths in each zone for well pairs HT-3 to HT-2 (a), HT-3 to HT-3 (b), HT-4 to HT-3 (c), HT-5 to HT-3 (d), and HT-6 to HT-3 (e).

In each well pair, the center of the model prior to zoning had the highest sum of ray path lengths because the most ray paths passed through those areas. Other nodes or elements were combined together to produce zones with sums comparable to the value in the center. Zone sums may differ by a factor of two but should not vary by as much as an order of magnitude. Zone sums in a given zone are fairly similar between models with approximately the same number of ray paths. Variation occurs from one well pair to another partially due to differing radii but largely due to the changing number of ray paths.

CHAPTER 3: Results

A. ZOP Data

The first field data used for analysis included HT-3 as the source well and HT-2 as the receiver well. This particular well pair was chosen to analyze first because the data were collected with the multi-level receiver after repairing a series of nitrogen leaks. The data from this well pair were therefore assumed to have the least amount of error. The SVD program was run with the ray path data for just the horizontal rays. These are essentially ZOP data. In a ZOP, the source and receiver are both moved vertically, but they remain at the same relative elevations. The effect is the same as decreasing the number of elements, as only one average phase shift is available across any given row. As shown in Figure 22, the resulting K values produced by the program are very similar to those obtained from high resolution slug tests and continuous pulse tests taken in previous years for this well pair.

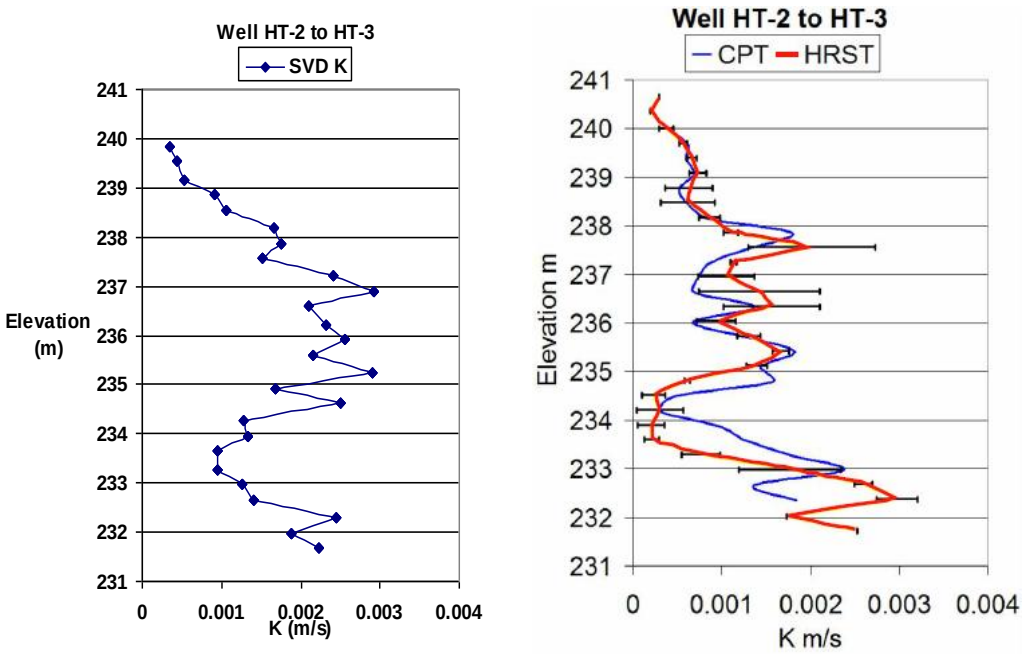

(a) (b)

Figure 22: Comparison of K values obtained by horizontal rays in the SVD program (a) and K values obtained by CPT and HRST methods (b).

The resolution limit of the spatially weighted average has been shown to be roughly 0.914 m (3 ft). One run-through of the SVD program produced only a third of the K values presented above. Data in this particular well pair were collected at a finer scale than could be accounted for by the resolution of the spatially weighted average method, resulting in a substantial amount of unused data. The problem was circumvented by running the SVD program three times. The initial run-through went to the bottom of the screened interval. Every run had the same element spacing and total depth, but each successive run positioned the bottom depth 0.3048 m shallower than the previous run. Each run-through analyzed either 8 or 9 of the 25 total ray

paths with their respective phase shifts. The K values from the three individual runs were combined together to provide the 1 ft spacing seen in Figure 22a.

B. SVD Processing

After choosing a zoning model, field data were run through the inversion program to determine K values. As stated in the Modeling section, the model chosen for this scenario was a 16 zone model where K was determined by elements and there were 6 nodes in the X direction. The data set from well HT-3 to well HT-2 was first examined because it seemed to be the best of the initial data sets. The HRST K values determined in previous tests were input as constant K nodes to help fix the other K values within a reasonable range. HRST results were processed by Brett Engard for wells HT-1, HT-2, and HT-3, and by Pema Deki for wells HT-4, HT-5, and HT-6. Plots of K values determined by HRST are presented in Appendix A (Figures 58-63).

Contour plots were made of K values plotted against elevation and the radial distance between wells using a program called QuikGrid, a public domain program. The program contours between points written in an x,y,z format, in this case corresponding to radius, elevation, and K. The contour interval chosen is 0.0002 m/s. The HRST values were chosen for the K values at each well in the plot. Interwell K values were all determined by the SVD analysis, a method of unconstrained least squares. In all of the contour plots of K, the source well is on the left side and the receiver well is on the right side.

K values in Figure 23 for the well pair from HT-3 to HT-2 are mostly within the range expected at the site. The highest K value is at the upper end of those seen at the site, but still within reason. The trend is what is expected at the site based on HRST results, with low K material near the top, a high K region in the middle, and then another high K region beginning at the bottom of the plot. The data set from HT-3 to HT-2 verified that the SVD program was working, and the program was then used to analyze the data from HT-3 to HT-1.

The data set presented in Figure 24 from HT-3 to HT-1 has several regions with K values as much as four orders of magnitude greater than those seen at the site in other investigations. The fine-scale trends in heterogeneity are masked by the anomalously large values in the center of the plot. The poorer results from this data set are likely caused by the nitrogen leaks at the time of data collection. Figure 25 shows the same data as Figure 24, but with a lower maximum value on the K scale to suppress the anomalously large value and show the same general high and low K zones seen in the first well pair. Drawing more definitive conclusions about this well pair would require collection of additional data with the current equipment, or using a different processing technique, as discussed later.

The first two well pairs produced mixed results using the unconstrained least squares analysis, but the results were still reasonable for the well pair from HT-3 to HT-2. In case the errors with the other well pair were solely due to nitrogen leaks, the unconstrained analysis was extended to the data from the fall of 2007 for the three newest wells. Limited time was left in the field season due to weather concerns, so

the data for the three newest wells were collected with larger intervals between either source locations, receiver locations, or both. The varying source and receiver intervals provided an opportunity to determine the minimum vertical sampling required for reasonable results.

The data in Figure 26 from HT-4 to HT-3 show a large low K zone at the top of the sampled area, a moderately higher K zone below it, another low K zone below that, and the highest K values at the bottom. The trend from HT-4 to HT-3 matches the overall trend observed between HT-3 and HT-2. K values at the site have not been known to exceed about 0.003 m/s in previous studies, so values of 0.006 m/s would not be expected. Although the values are high, they are at least on the correct order of magnitude, and they occur in a section of the aquifer known for high K values.

One of the zone values in Figure 27 from HT-6 to HT-3 is an order of magnitude larger than the values should be at the site. The only clear trend is the high K region in the right portion of the plot. This particular well pair, HT-5 to HT-3, had the second lowest sampling interval of any of the well pairs sampled, with only 10 source locations and 10 receiver locations in the initial survey. An additional 90 rays were acquired from a separate survey the following day, in which the receiver was kept at a fixed location while the source was moved. All of the other well pairs had 30 receiver locations and between 10 and 25 source locations. Figure 28 presents a view of Figure 27 with the large K zone suppressed and a higher K zone visible at the bottom. Either Figure 27 or 28 demonstrates that 190 ray paths are not enough to

adequately characterize the study area or that the unconstrained processing is not adequate.

The contour plot results for the well pair from HT-6 to HT-3 are presented in Figure 29. The plot shows the same trend seen in tomography experiments between the other well pairs, as well as in slug tests. The K values are also within the expected range for GEMS. Even the highest K values at the bottom of the sample area are reasonable for the site.

The results are plausible for most of the well pairs studied. A given well pair sometimes showed unexpectedly high K values in one or two zones, but the rest of the zones had values within the range previously measured at the site. One well pair, HT-3 to HT-1, even includes a K value that exceeds the range found in both sand and gravel-sized particles. The plots all show the expected patterns of high and low K regions after adjusting the QuikGrid scale to suppress the anomalously large K values. In spite of the good fit in most zones throughout the well pairs, none of the K values should be orders of magnitude greater than the largest values known to exist at the site from HRST and the data therefore requires some sort of editing or constrained analysis.

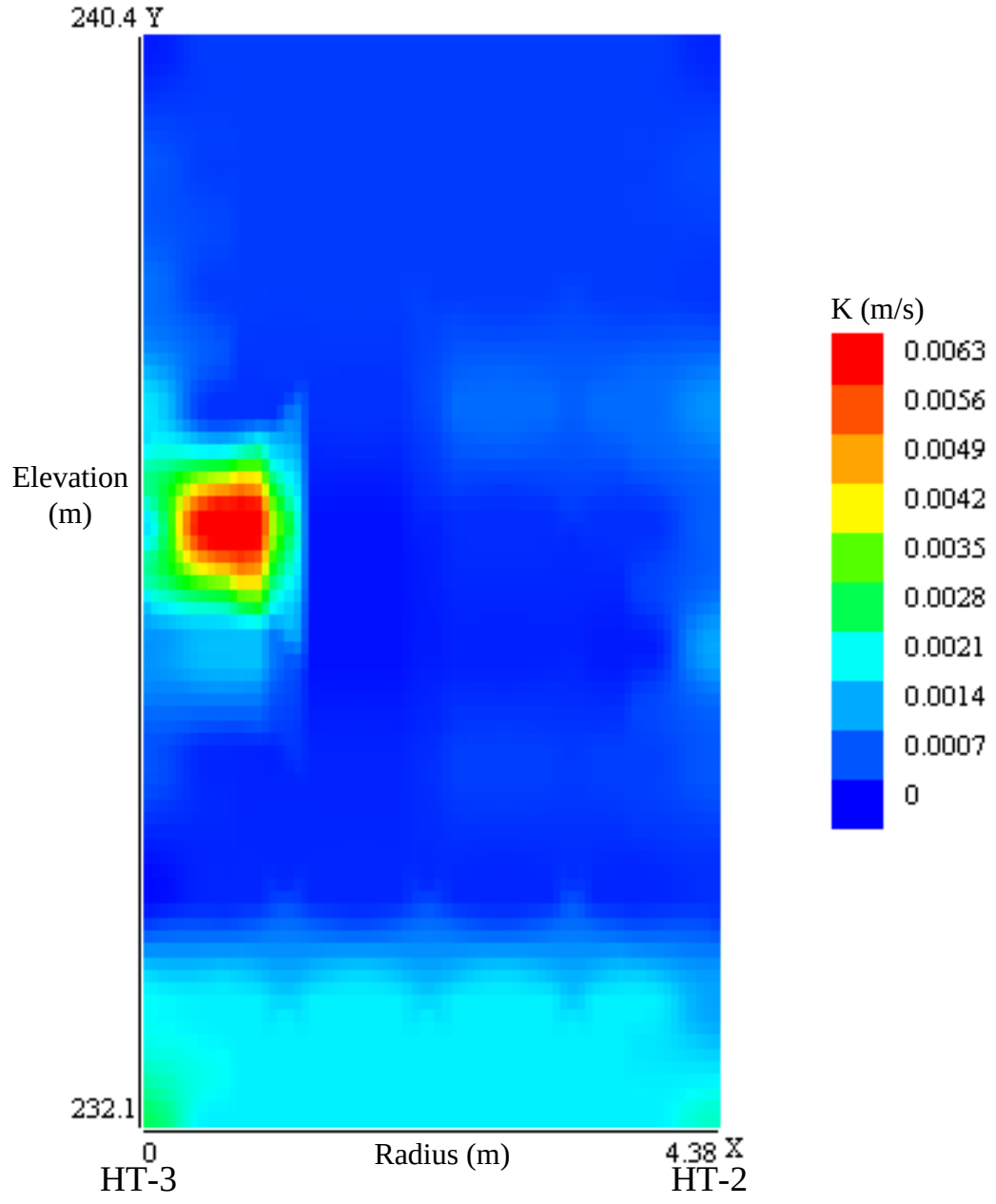

Figure 23: Interwell K values from unconstrained SVD analysis with HT-3 as the source well and HT-2 as the receiver well.

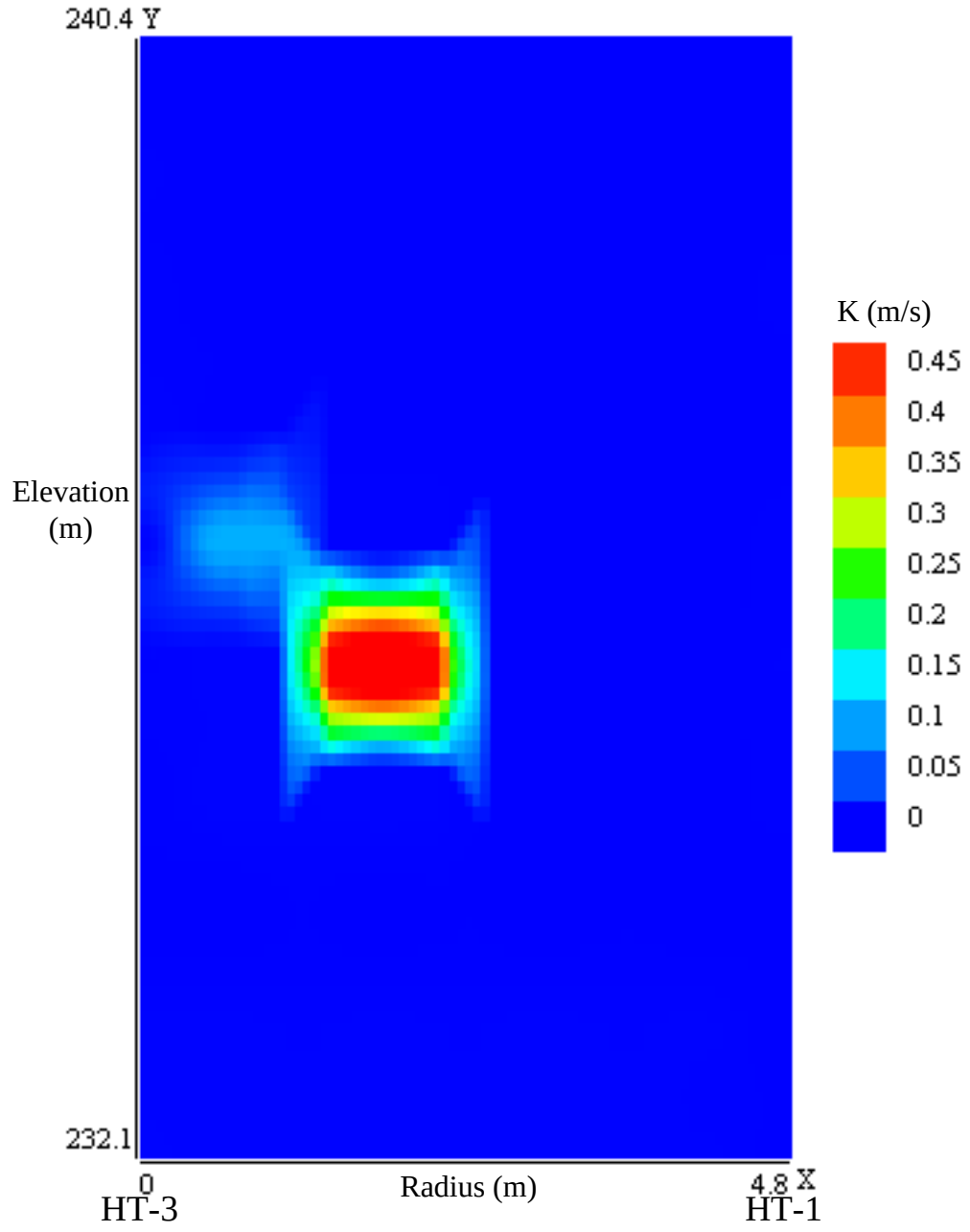

Figure 24: Interwell K values from unconstrained SVD analysis with HT-3 as the source well and HT-1 as the receiver well.

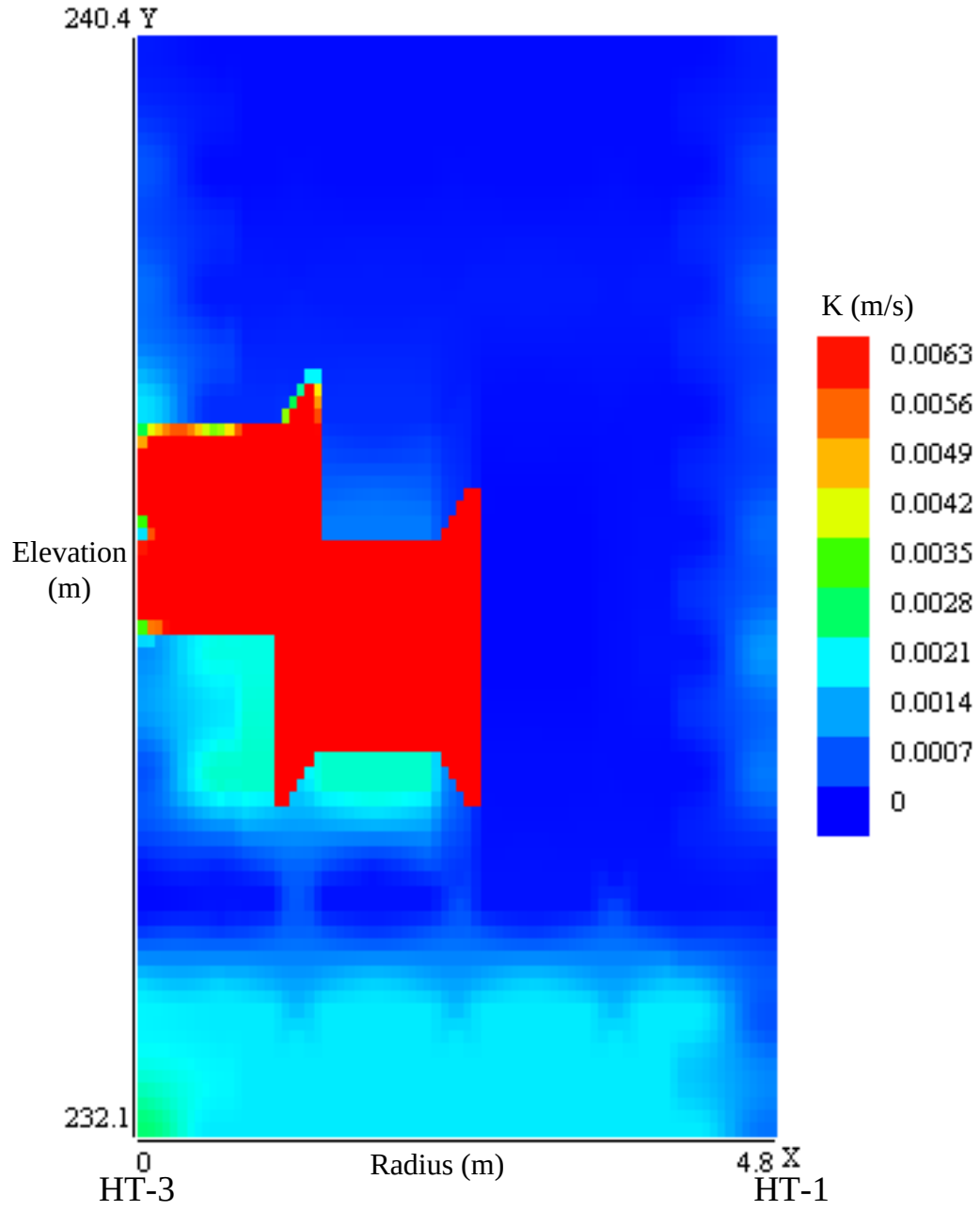

Figure 25: Interwell K values from unconstrained SVD analysis with HT-3 as the source well and HT-1 as the receiver well (with a lower maximum value on the K scale).

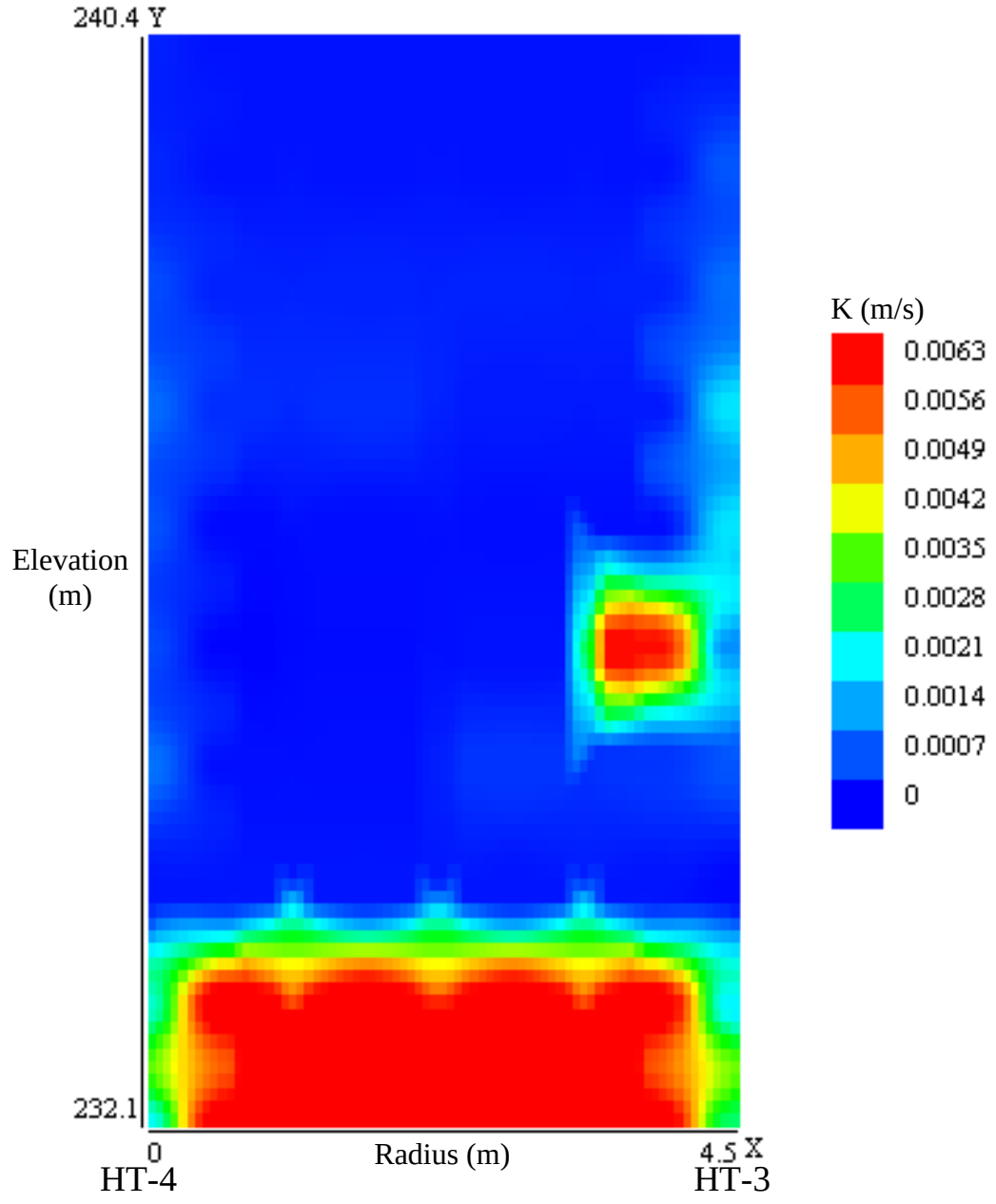

Figure 26: Interwell K values from unconstrained SVD analysis with HT-4 as the source well and HT-3 as the receiver well.

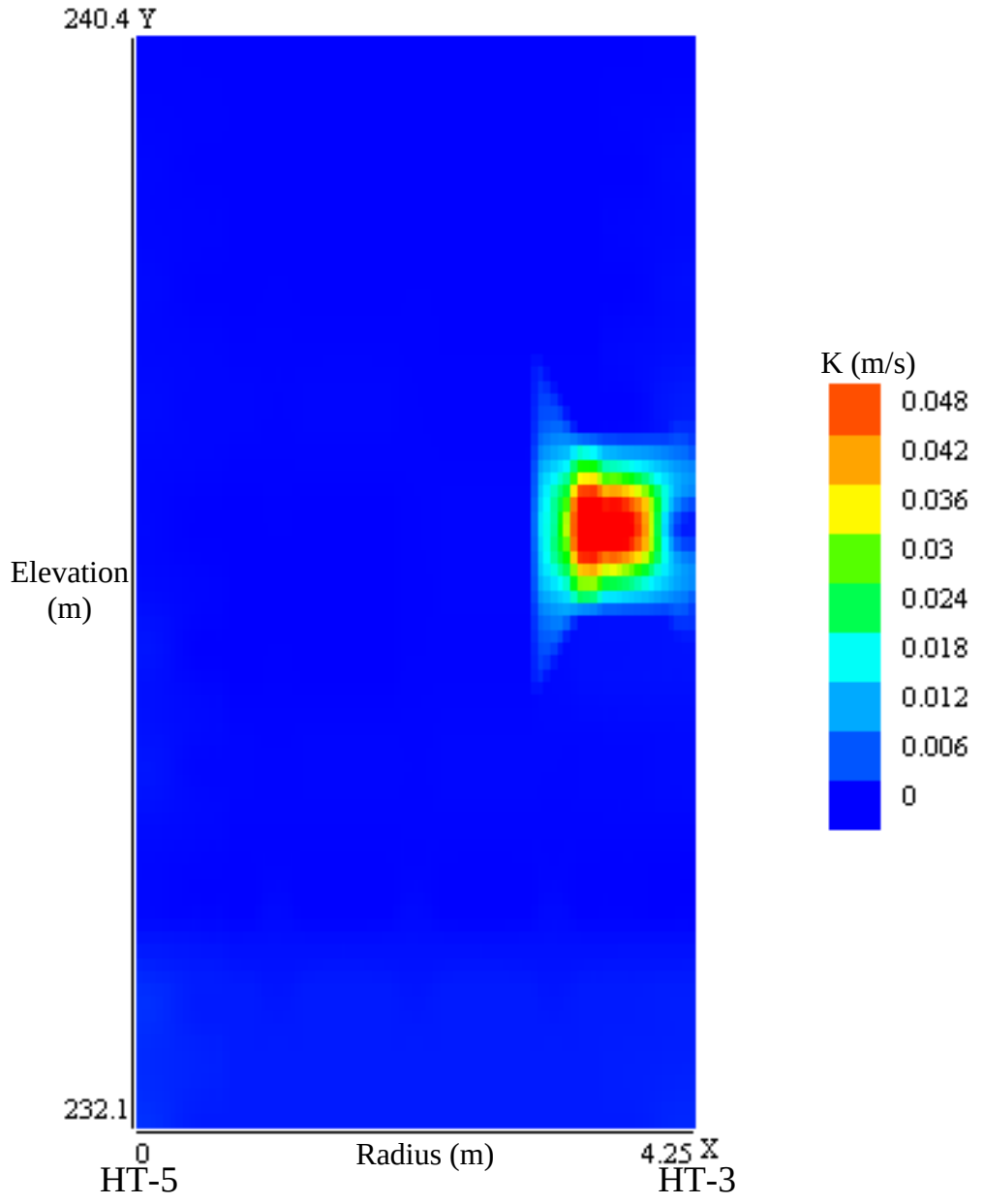

Figure 27: Interwell K values from unconstrained SVD analysis with HT-5 as the source well and HT-3 as the receiver well.

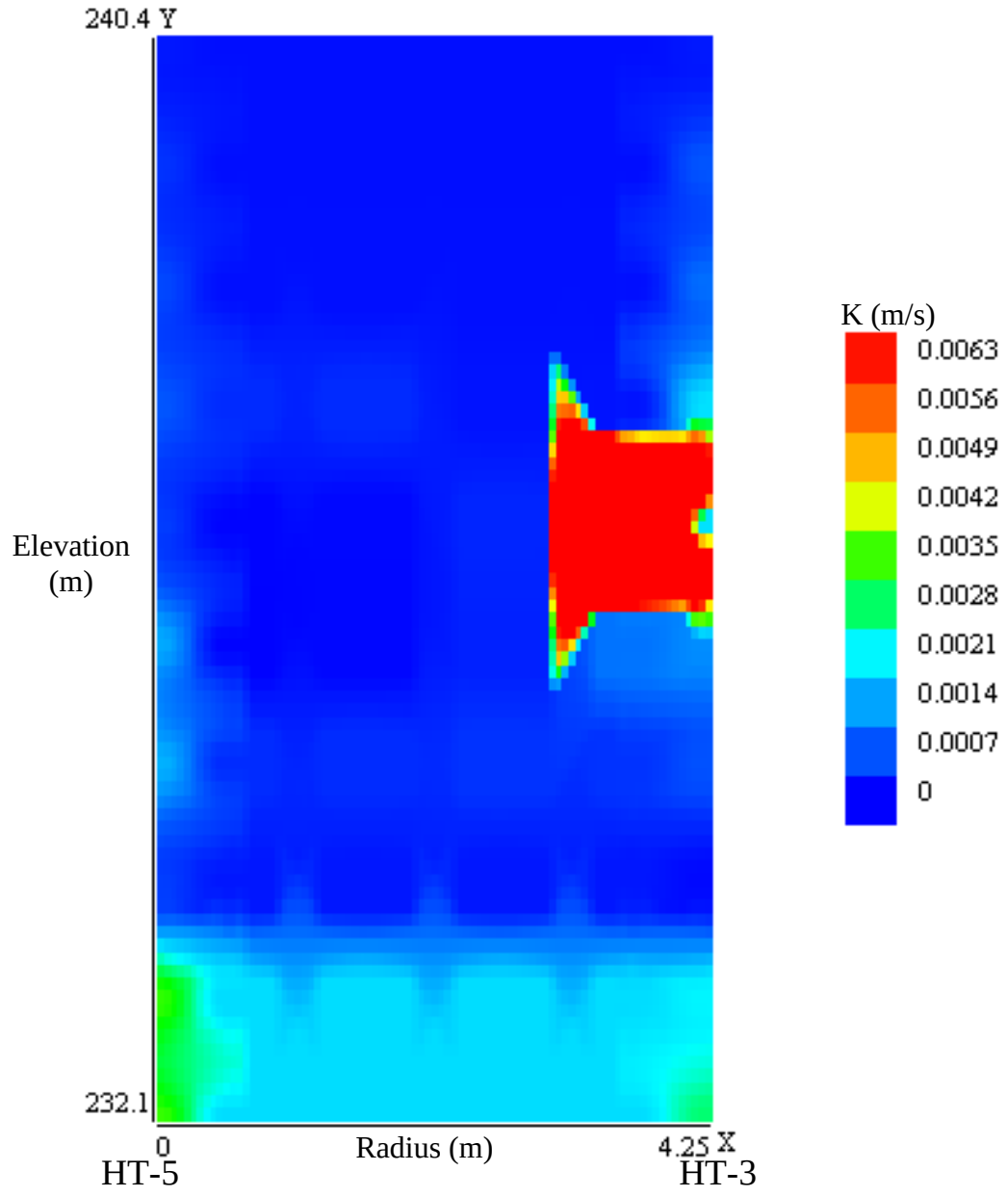

Figure 28: Interwell K values from unconstrained SVD analysis with HT-5 as the source well and HT-3 as the receiver well (with a lower maximum value on the K scale).

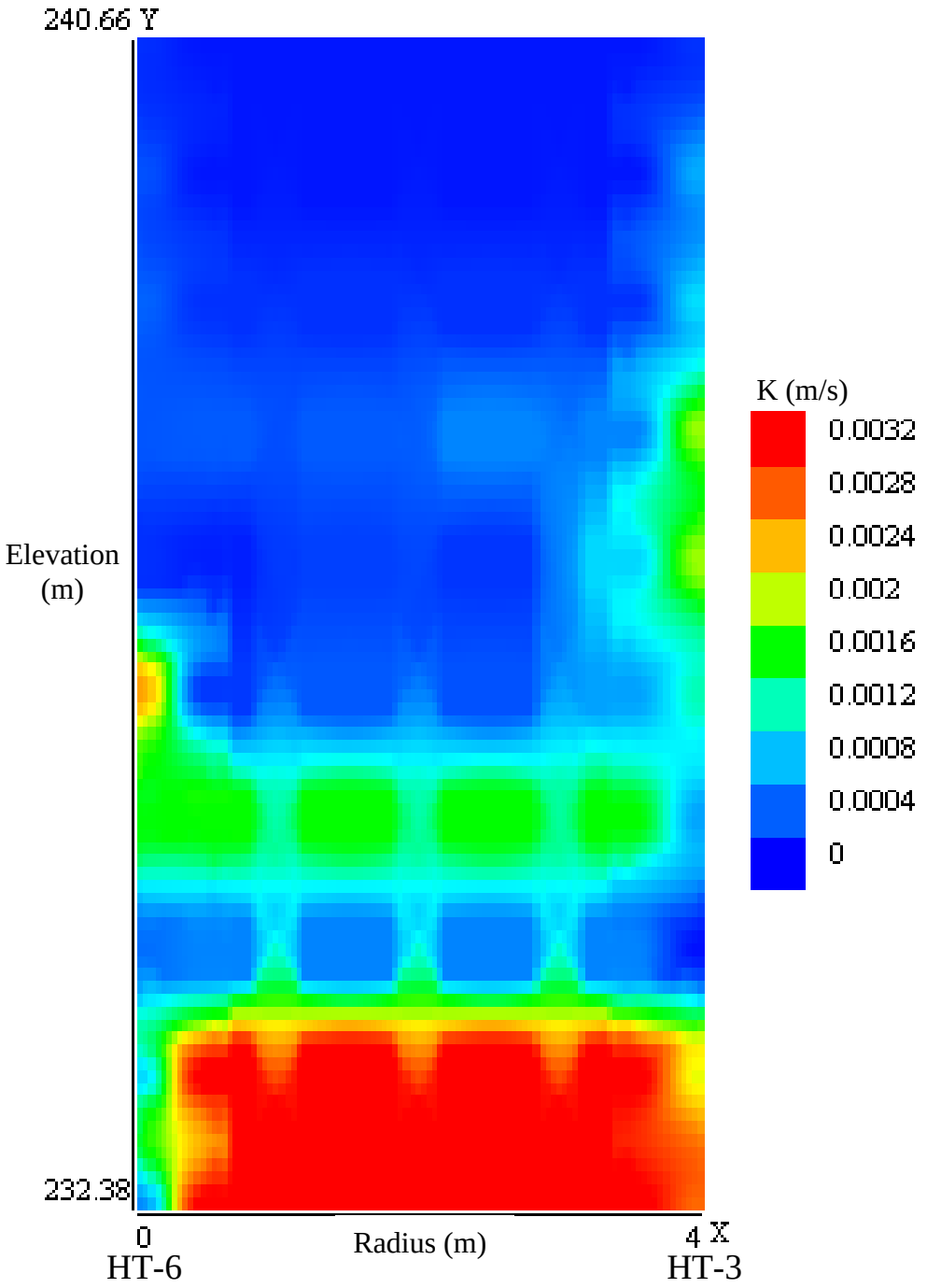

Figure 29: Interwell K values from unconstrained SVD analysis with HT-6 as the source well and HT-3 as the receiver well.

C. Phase Modeling in Heterogeneous Systems

The phase shift between source and receiver signals was expected to be at a low point when the source and receiver were at equal elevations, and greater with increasing offset between the source and receiver. Modeling studies were conducted to mirror site conditions with a 5 zone model consisting of a high K zone on the bottom, a low K zone above that, a moderately high K zone in the middle, and then two identical low K zones at the top (Figure 30). Modeling was performed for five source locations in the top half of the area. Within this framework, it was shown that the phase could also decrease if it passed through a high K zone (Figures 31-35). In two of the cases studied, the points with the lowest phases are not even where the source and receiver are at the same depth because the area is within the low K zone (Figures 33 and 34). The modeling indicates that the ability to resolve K is dependent on not only the amount of error but also upon how large or small the K values themselves are. As shown in equation 14 in the Introduction, a higher K value corresponds to a smaller phase shift, and a given error in the phase shift will cause a greater percentage change. The phase shift values are therefore more sensitive to small amounts of noise in the zones with larger K values than in the low K zones.

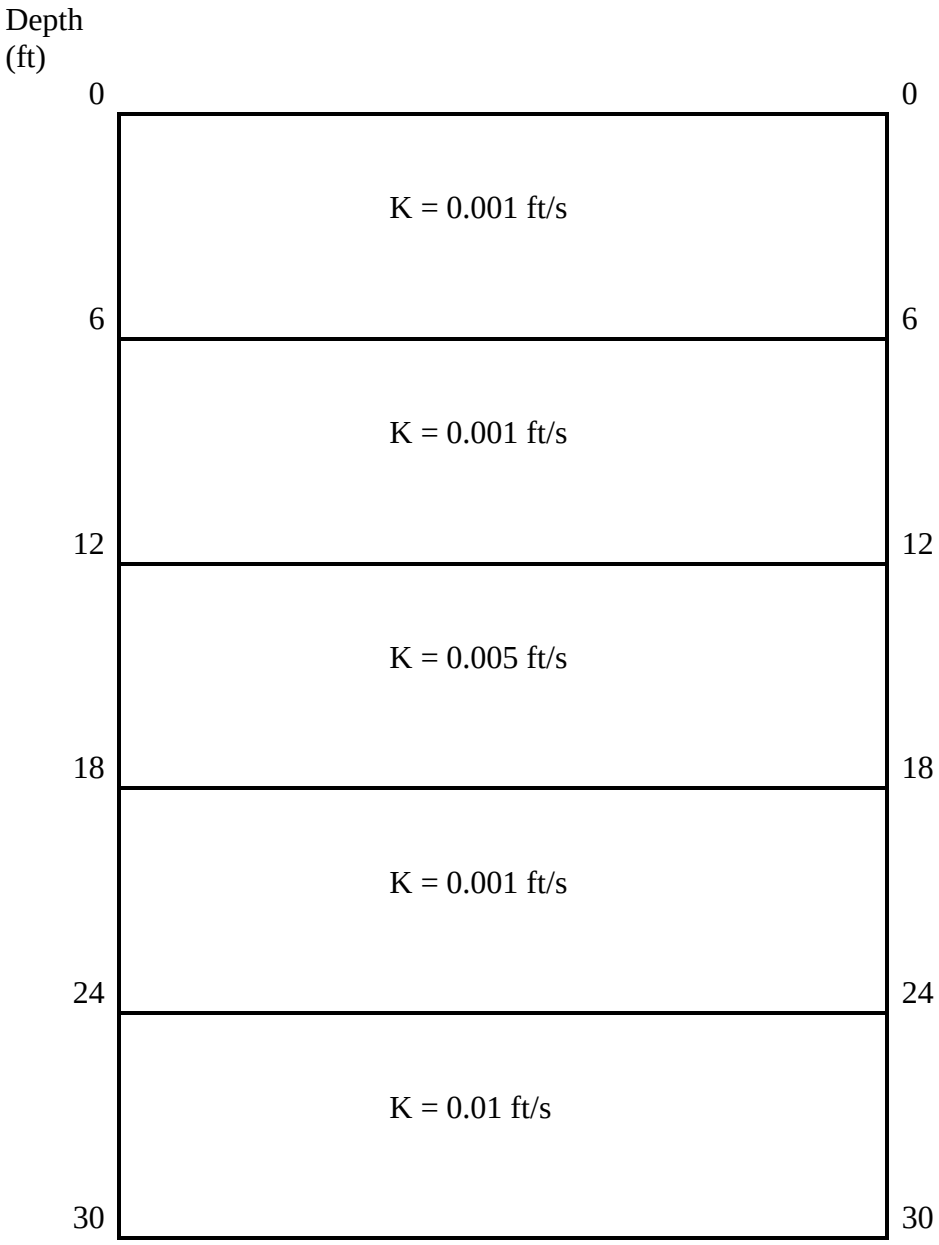

Figure 30: Diagram of 5 zone model used to investigate phase pattern.

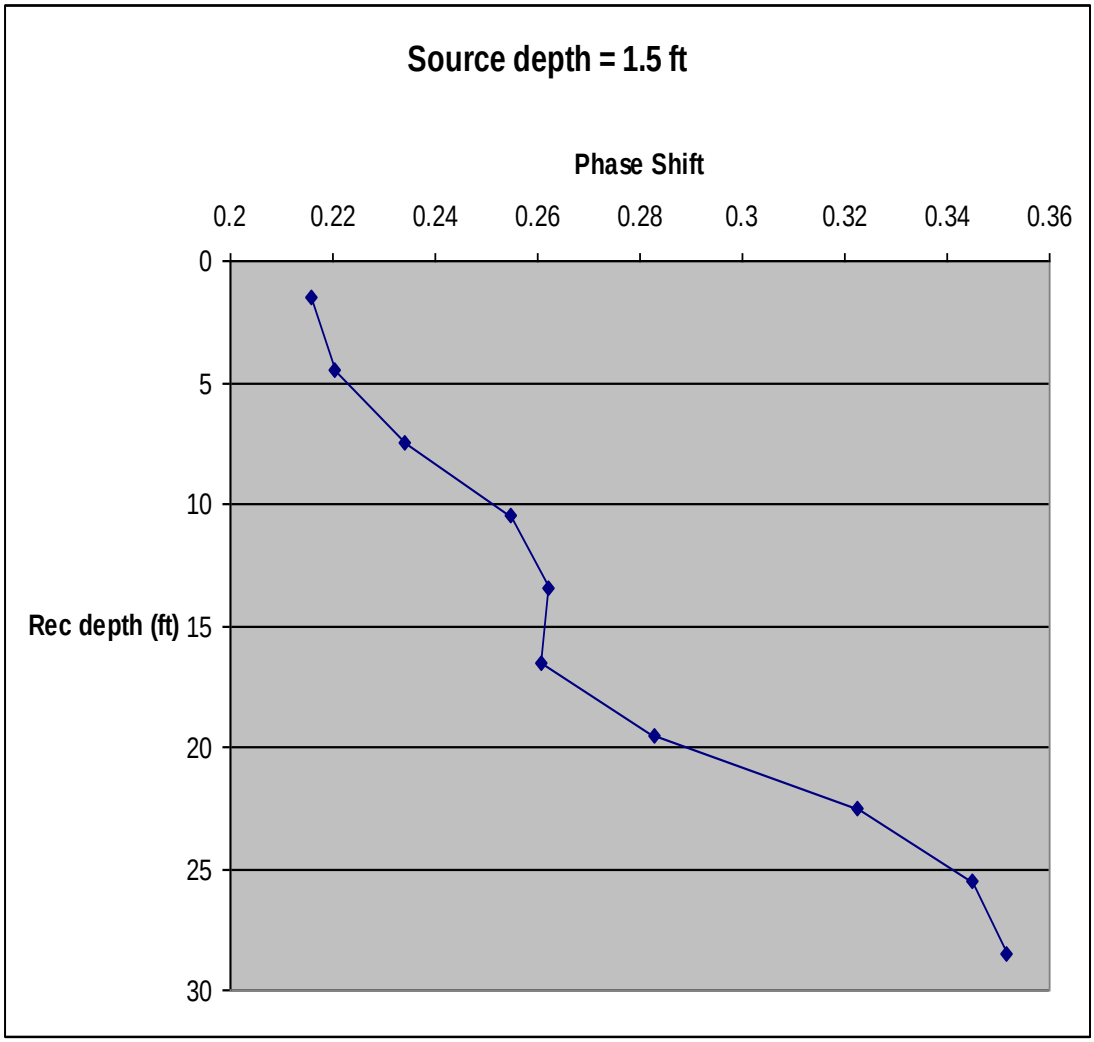

Figure 31: 5 zone, 50 element modeled data with a source depth of 1.5 ft.

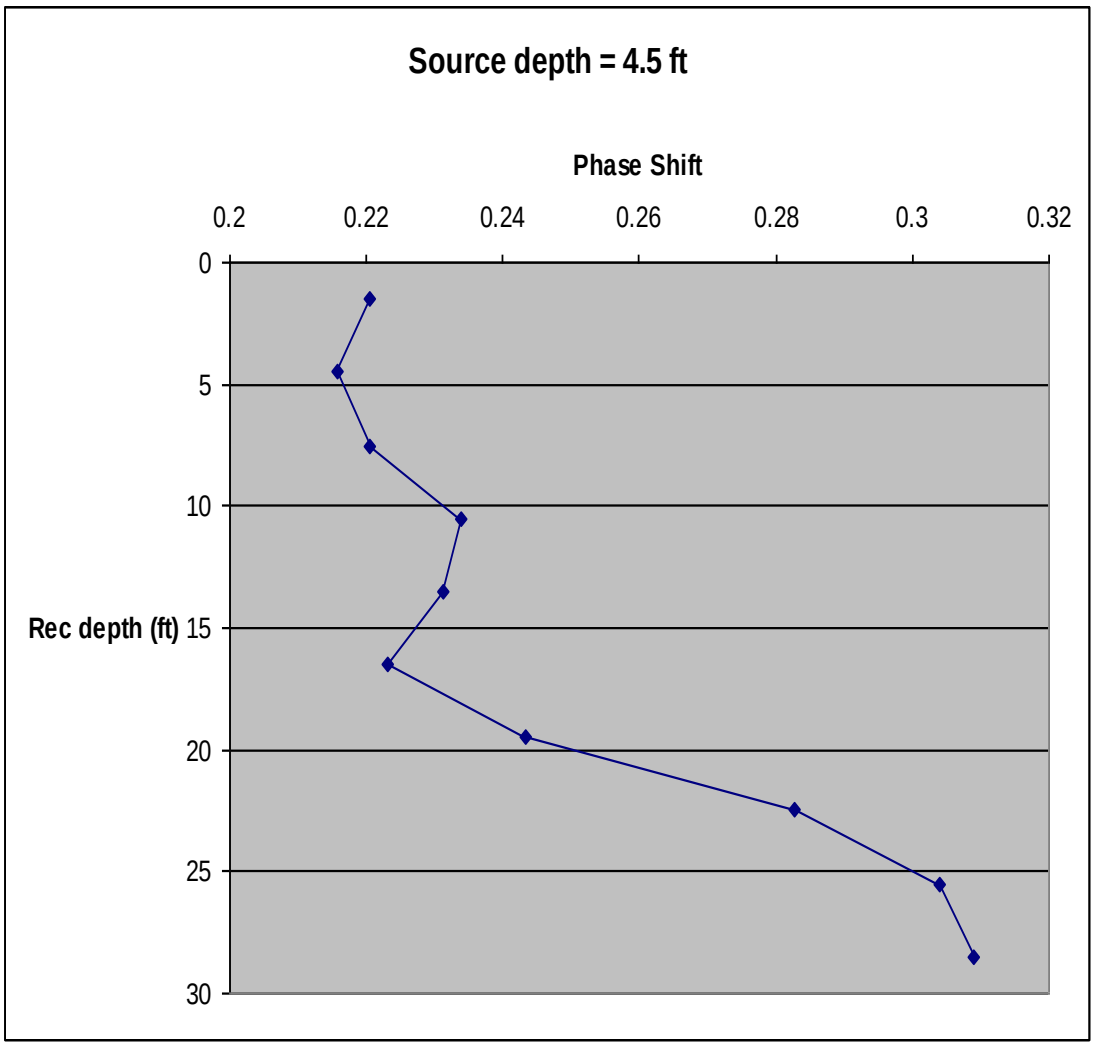

Figure 32: 5 zone, 50 element modeled data with a source depth of 4.5 ft.

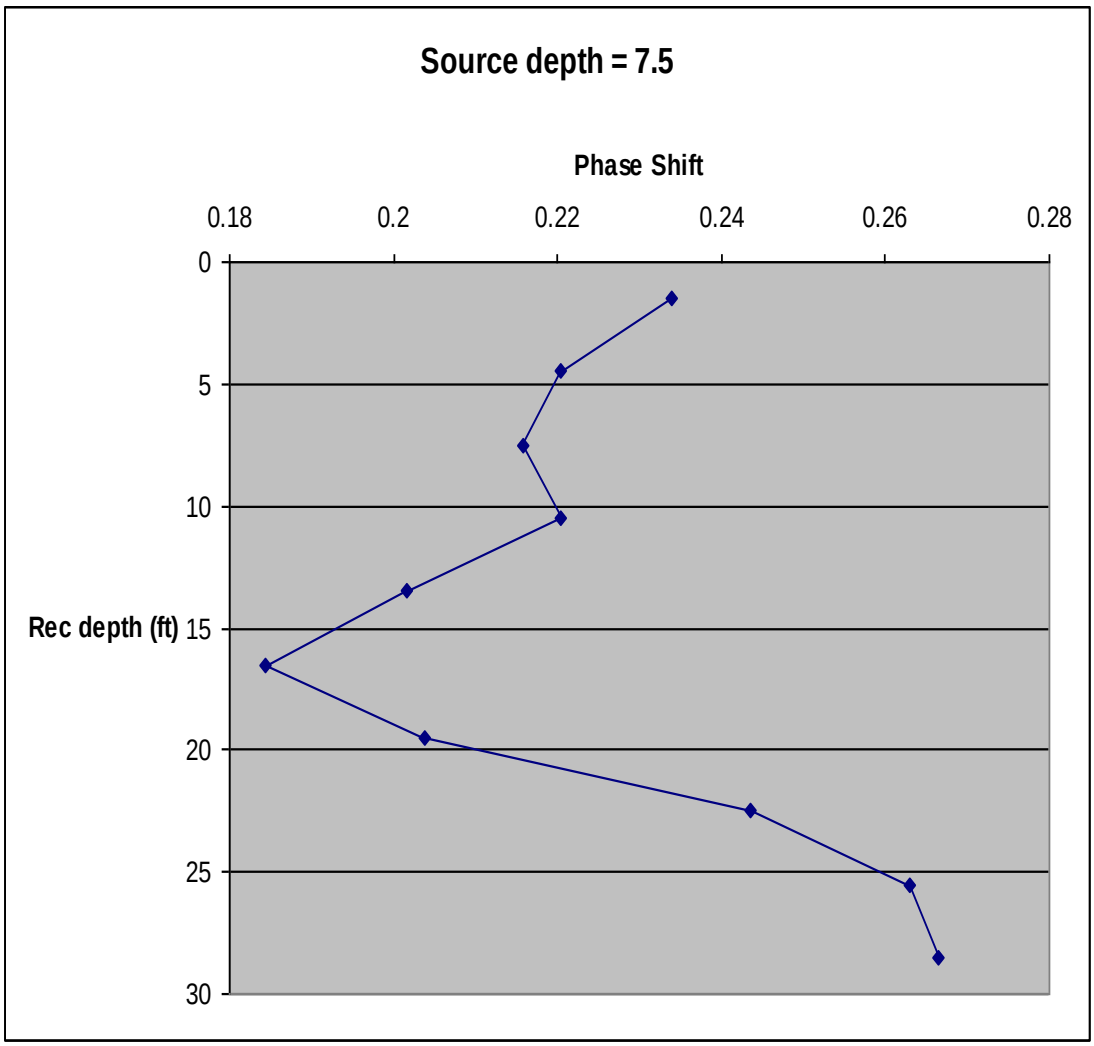

Figure 33: 5 zone, 50 element modeled data with a source depth of 7.5 ft.

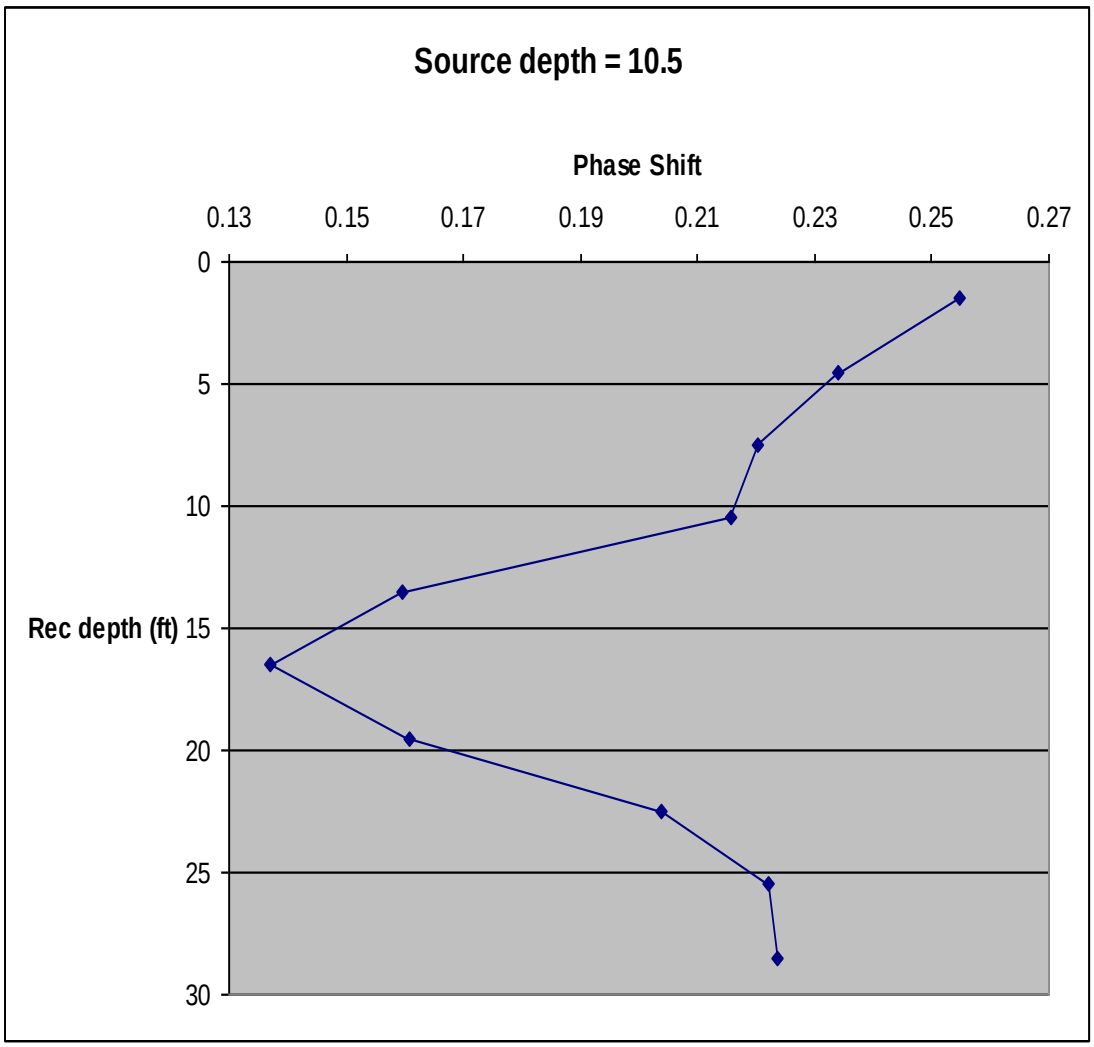

Figure 34: 5 zone, 50 element modeled data with a source depth of 10.5 ft.

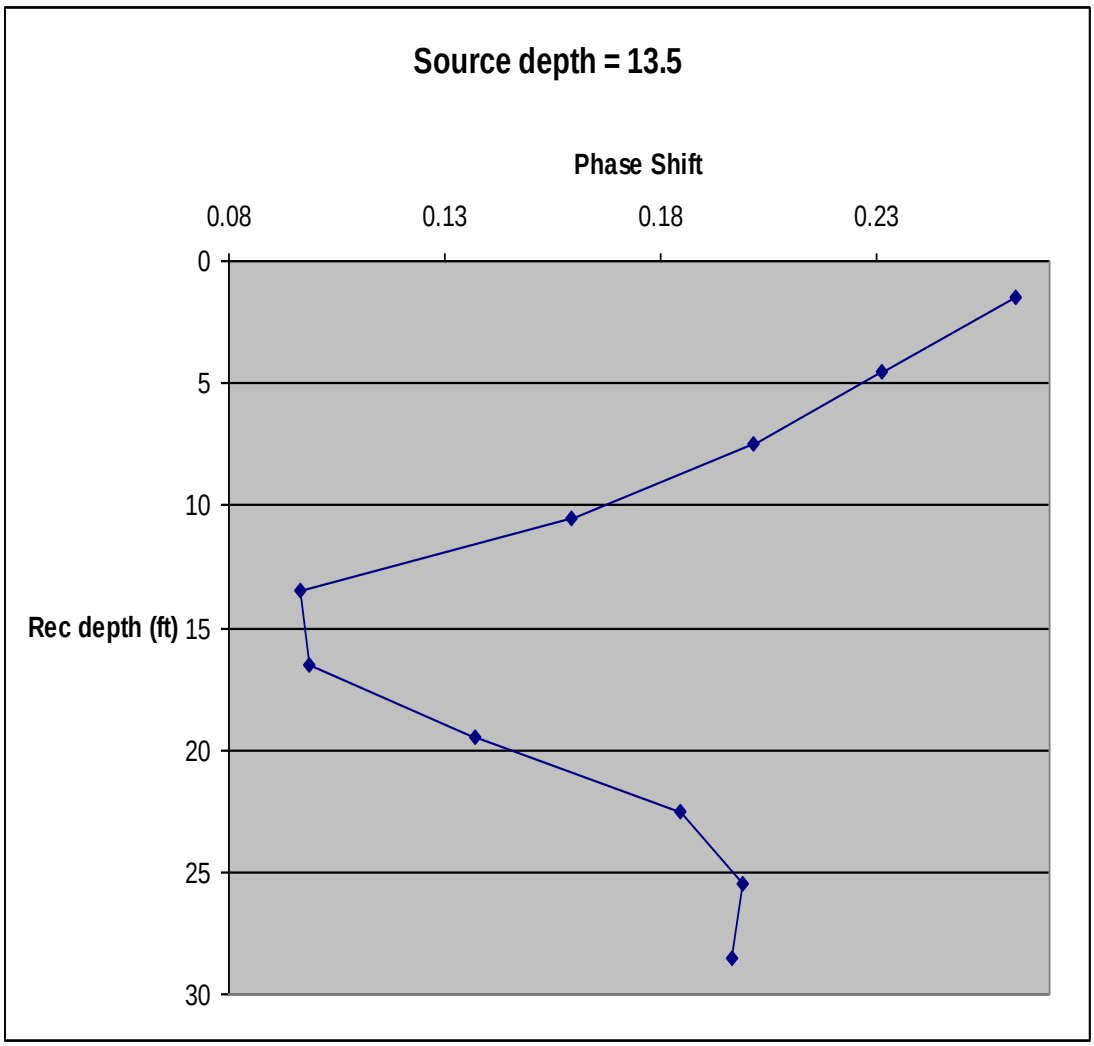

Figure 35: 5 zone, 50 element modeled data with a source depth of 13.5 ft.

D. Editing of Data

The SVD inverse program performs perfectly without noise, so it must be much more sensitive to noise in phase shift data than originally thought. To compensate for the sensitivity to noise, a seven point filter was used on the data from HT-3 to HT-2. The amplitude ratio between source and receiver had also gone

constant at some of the larger offsets, an indication that noise was stronger than the signal and therefore masking any change in amplitude. The amplitude decays as it travels, so the problems are only seen in the rays with larger offsets where the amount of noise is larger than the signal. Figures 36 and 37 depict how the amplitude ratio went constant for the data that were edited. These rays were filtered out and the SVD program was run again. As shown in Table 5 and Figures 38-41, the results after filtering and editing out some of the larger offset traces were similar to the results from the unfiltered data, with the zones of high and low K in the right order but high K values one or two orders of magnitude above the range observed with HRST. The large K value in Figure 39 had to be suppressed to observe the other zones even in the seven point filter data (Figure 40), and therefore some method of constrained analysis is required to process the data. As an alternative processing scheme, a least squares fit was employed constrained by the HRST data.

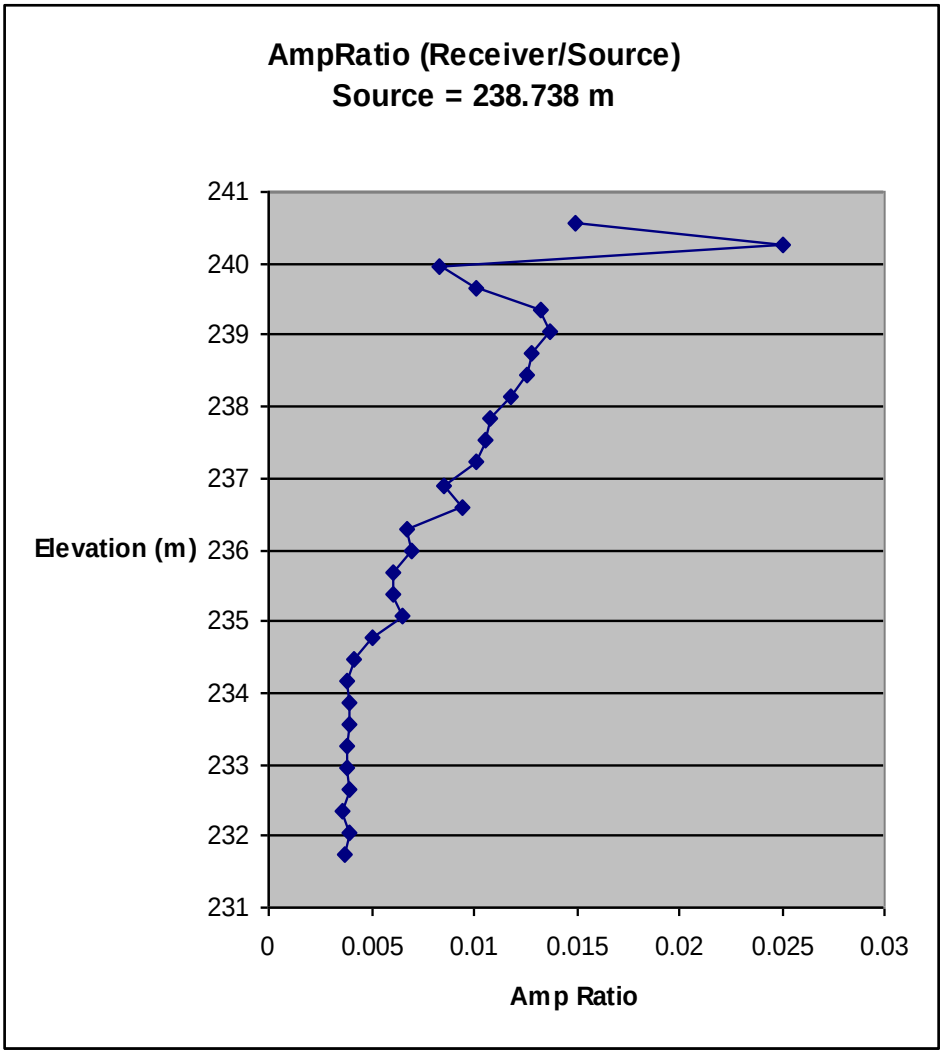

Figure 36: Amplitude ratio between receiver and source wells for a single MOG with a source elevation of 238.738 m. The nine points at the bottom of the profile have a constant amplitude ratio and were edited out.

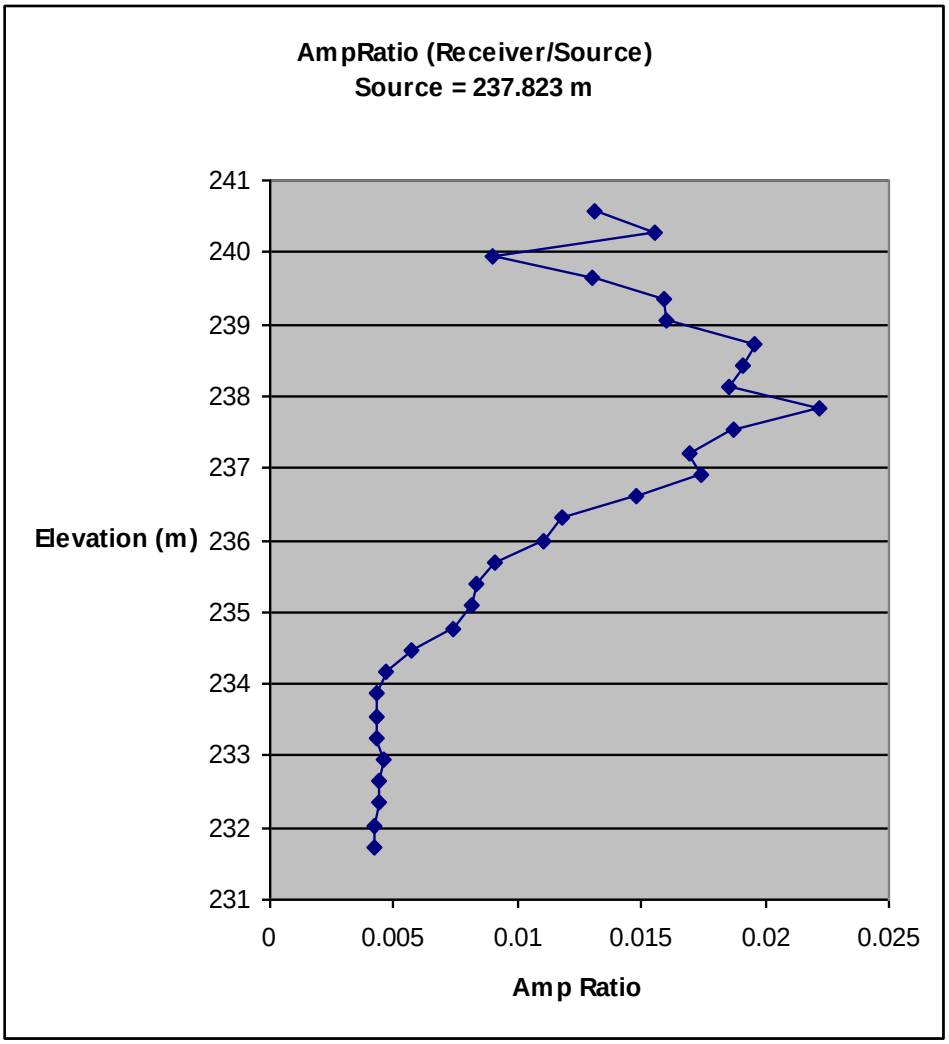

Figure 37: Amplitude ratio between receiver and source wells for a single MOG with a source elevation of 237.823 m. The eight points at the bottom of the profile have a constant amplitude ratio and were edited out.

Table 5: K values (m/s) obtained through SVD program.

Zone	HT-3 to HT-1 40elem	HT-3 to HT-2 50elem	HT-3 to HT-2 40elem	HT-3 to HT-2[(1)] 40elem	HT-3 to HT-2[(2)] 40elem	HT-3 to HT-2[(1,2)] 40elem	HT-4 to HT-3 40elem	HT-5 to HT-3 40elem	HT-6 to HT-3 40elem
1	0.00201	0.00163	0.00199	0.00235	0.00189	0.00218	0.00684	0.00188	0.003293
2	0.000150	0.000321	0.000310	0.000627	0.000314	0.000630	0.000173	0.000188	0.000556
3	0.00236	0.03197	0.000287	0.00143	0.000301	0.00115	0.000115	0.000371	0.001607
4	0.000097	0.0000345	0.000511	0.000665	0.000442	0.000700	0.000434	0.000433	0.001600
5	0.00225	0.0140	0.00159	0.00445	0.00506	0.00154	0.000036	0.000021	0.000236
6	0.519	0.00286	0.000138	0.000233	0.000175	0.000332	0.0000914	0.0000556	0.000371
7	0.0000430	0.0000214	0.000274	0.000733	0.000206	0.000465	0.000147	0.000280	0.000342
8	0.000154	0.000540	0.000215	0.000276	0.000166	0.000214	0.00627	0.000983	0.000679
9	0.110	0.00180	0.00667	0.00136	0.484	0.002635	0.0000741	0.000029	0.000127
10	0.00104	0.0000189	0.000148	0.0000954	0.000202	0.000112	0.000106	0.0000603	0.000268
11	0.0000453	0.000411	0.000369	0.00257	0.000275	0.00184	0.000101	0.000309	0.000226
12	0.000128	0.0185	0.000392	0.000563	0.000435	0.00101	0.000108	0.0575	0.000904
13	0.000372	0.000038	0.000405	0.000220	0.000429	0.000231	0.000379	0.000361	0.000378
14	0.000102	0.002456	0.000884	0.0138	0.000874	0.0131	0.000212	0.000160	0.000557
15	0.000209	0.000579	0.000492	0.000647	0.000523	0.000677	0.000278	0.000122	0.000202
16	0.0000822	0.000452	0.000502	0.000572	0.000517	0.000575	0.000150	0.000118	0.0000918

(1): Rays with constant amplitude ratio edited out.
(2): Filtered using 7 point average.

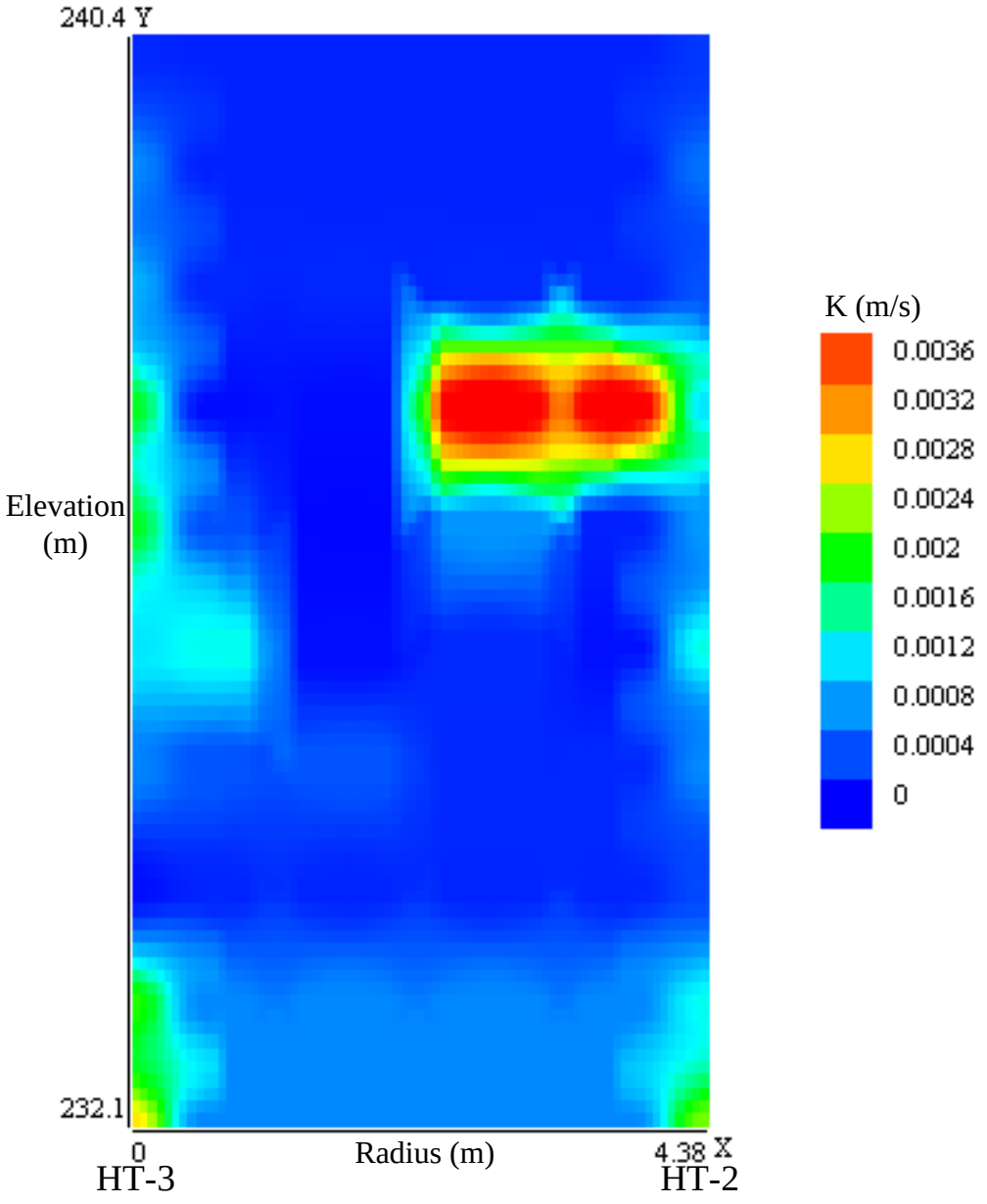

Figure 38: Interwell K values from unconstrained SVD analysis with HT-3 as the source well and HT-2 as the receiver well (with rays of constant amplitude ratio edited out).

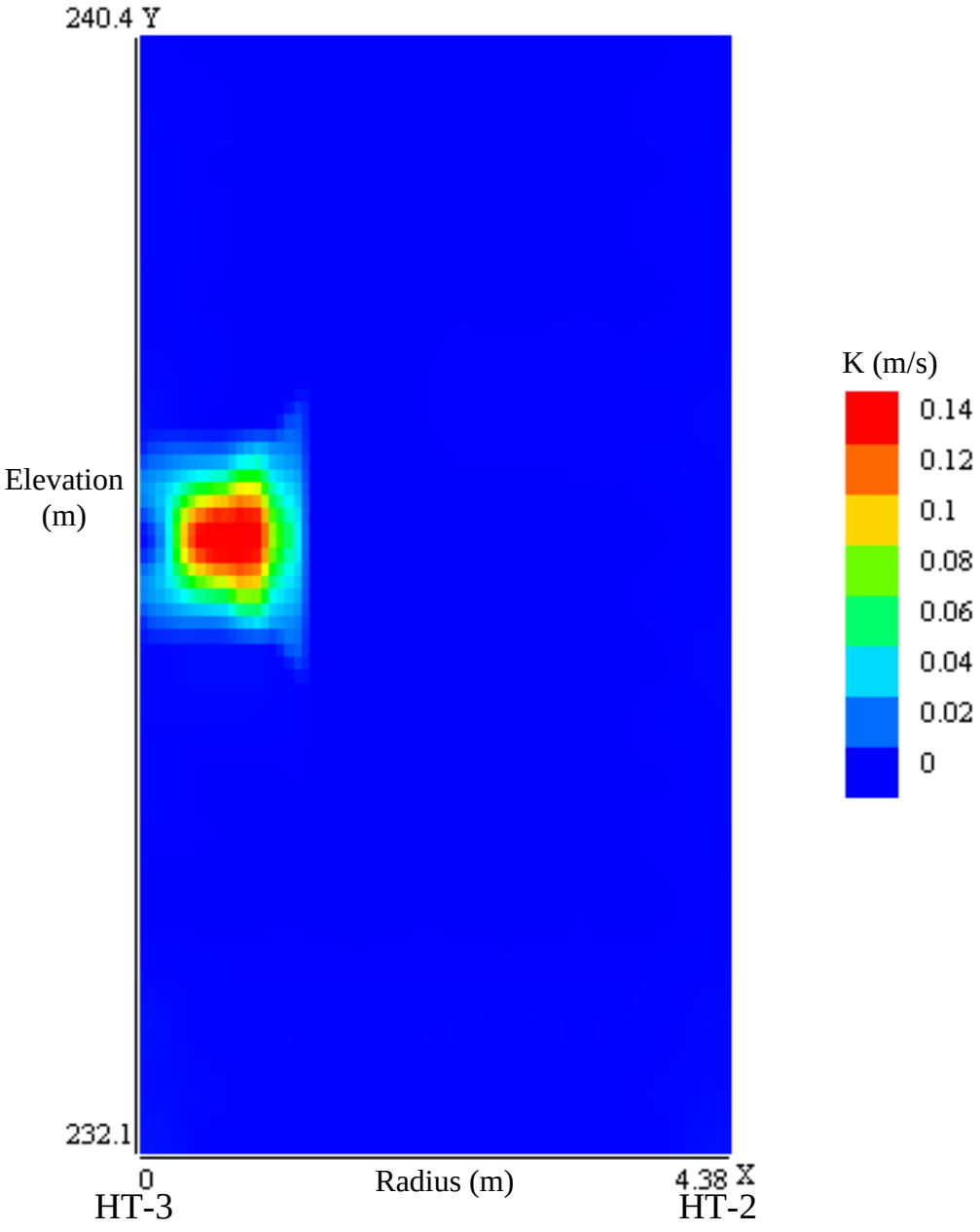

Figure 39: Interwell K values from unconstrained SVD analysis with HT-3 as the source well and HT-2 as the receiver well (with seven point filter).

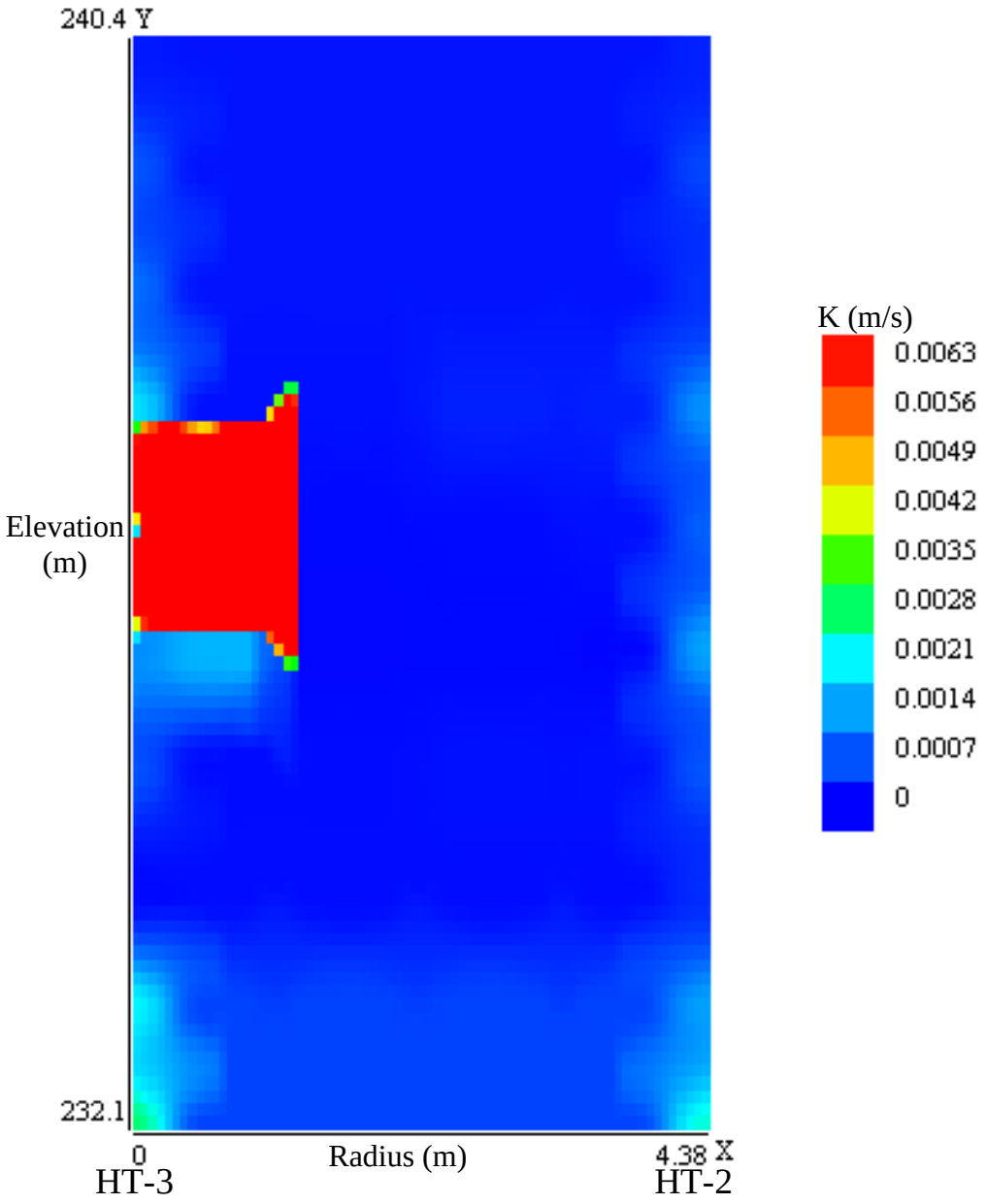

Figure 40: Interwell K values from unconstrained SVD analysis with HT-3 as the source well and HT-2 as the receiver well (with seven point filter and a lower maximum value on the K scale).

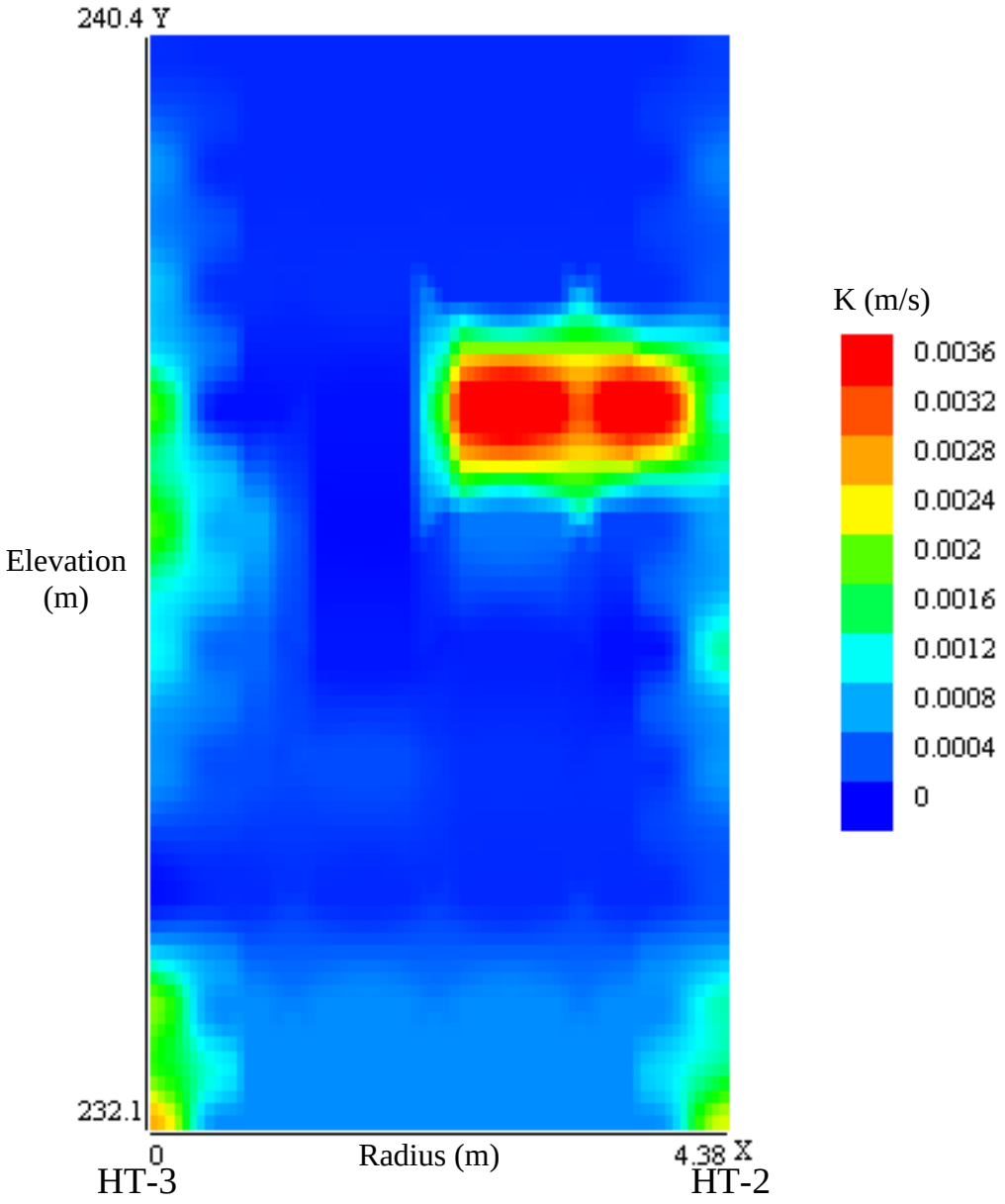

Figure 41: Interwell K values from unconstrained SVD analysis with HT-3 as the source well and HT-2 as the receiver well (with seven point filter and rays of constant amplitude ratio edited out).

E. Constrained SVD

Inverse problems are commonly constrained with data known from other sources or methods; in this case, HRST results were used to constrain the inversion for K values. Initial guesses of K in each zone were obtained through a linear interpolation of HRST values at the same elevations as each other. The sum of squared errors (SSE) was calculated by comparing the phase values measured in the field to the phase values calculated using SVD. A weighting factor is used in the latest version of the SVD program to determine to what extent the HRST results constrain the inversion. A weighting factor of zero is equivalent to the unconstrained SVD analysis, and increasing values for the weighting factor result in increasing weight given to the HRST results and therefore less deviation from HRST values. For this study, a weighting factor of 1.0 was used, which results in about equal weight of the HRST data and the tomographic data. The K value in a zone is only changed if it is still in the approximate range of values seen from HRST. The results were calculated using two values for S_s, 10^{-5} (Table 6) and 1.5×10^{-5} (Table 7).

Plots of experimental field phase values and calculated phase values versus elevation for individual MOGs are presented in Appendix B (Figures 64-88). Five MOGs are shown for each well pair, with one for a source location at the top of the well, one with the source at the bottom of the well, and three with the source in the middle of the well. The experimental and calculated phase values within individual MOGs match each other reasonably well in all the well pairs except for HT-3 to HT-1, most likely because of the previously mentioned equipment problems during data

collection. The good matches for the other four well pairs provide confidence in the constrained SVD analysis.

Table 6: K values (m/s) obtained after iterating using the constrained SVD analysis ($S_s = 10^{-5}$).

Zone	HT-3toHT-1 50elem 780 rays	HT-3toHT-2 40elem 750 rays	HT-3toHT-2 50elem 750 rays	HT-3toHT-2 50elem 270 rays	HT-3toHT-2 50elem 170 rays	HT-3toHT-2 50elem 90 rays	HT-4toHT-3 50elem 100 rays	HT-5toHT-3 50elem 190 rays	HT-6toHT-3 50elem 300 rays
1	0.004404	0.0074862	0.0058252	0.0051154	0.0051625	0.0049338	0.0060699	0.005425	0.0107446
2	0.0011044	0.0007794	0.0012579	0.0011813	0.0015434	0.0012734	0.0014829	0.0009898	0.001248
3	0.0003231	0.001476	0.0006166	0.0005975	0.0007826	0.0006126	0.003498	0.0027994	0.0037067
4	0.0004029	0.0012684	0.0010956	0.0010228	0.0010677	0.0010214	0.0024315	0.0020906	0.004816
5	0.0003207	0.00413	0.0012579	0.001162	0.0013765	0.0011777	0.0015143	0.0007947	0.0033531
6	0.0067165	0.001326	0.002753	0.0028131	0.0024481	0.0025694	0.0033182	0.005046	0.0158121
7	0.0018712	0.002018	0.0017516	0.0016532	0.0017923	0.001771	0.0065138	0.000976	0.0023381
8	0.0020057	0.0064817	0.0052522	0.0041009	0.004814	0.0036683	0.0079078	0.003463	0.0061995
9	0.0017238	0.0054021	0.0016193	0.0017939	0.0014134	0.0016523	0.0053158	0.0013502	0.0031366
10	0.0010119	0.0013811	0.0010374	0.0009865	0.0010515	0.0009151	0.007074	0.0005979	0.0012969
11	0.0019704	0.0022031	0.0035885	0.002996	0.0027921	0.0033401	0.0074449	0.00148	0.004094
12	0.0011519	0.0037096	0.0022713	0.0022118	0.0015644	0.0019312	0.0047499	0.0007769	0.001627
13	0.0012693	0.0026868	0.0031371	0.0032096	0.0032301	0.0027179	0.0040592	0.0019252	0.003049
14	0.0009069	0.0023642	0.0030193	0.0027131	0.0034024	0.0031891	0.0051039	0.0016292	0.0030399
15	0.0006855	0.0015154	0.0015675	0.0014628	0.0012573	0.0013588	0.005706	0.0004734	0.0007758
16	0.0004172	0.0014292	0.001563	0.0014545	0.001413	0.0013843	0.0040793	0.0005685	0.0004313

Table 7: K values (m/s) obtained after iterating using the constrained SVD analysis ($S_s = 1.5 \times 10^{-5}$).

Zone	HT-3toHT-1 50elem 780 rays	HT-3toHT-2 40elem 750 rays	HT-3toHT-2 50elem 750 rays	HT-3toHT-2 50elem 270 rays	HT-3toHT-2 50elem 170 rays	HT-3toHT-2 50elem 90 rays	HT-4toHT-3 50elem 100 rays	HT-5toHT-3 50elem 190 rays	HT-6toHT-3 50elem 300 rays
1	0.0059224	0.0110622	0.0083746	0.0074443	0.0078103	0.0073452	0.0098291	0.0081054	0.0165329
2	0.0018614	0.0010535	0.0019261	0.0018041	0.0023823	0.0019379	0.0019216	0.0014876	0.0016687
3	0.0003661	0.0020754	0.0007449	0.0007199	0.000909	0.0007349	0.004419	0.0037312	0.0049737
4	0.0004441	0.0017475	0.0013065	0.001226	0.001314	0.0012316	0.0028086	0.0026506	0.005839
5	0.0003943	0.0046685	0.0016376	0.0015258	0.0018896	0.0015556	0.0017495	0.0010506	0.0042925
6	0.0117715	0.0019606	0.0042273	0.0042145	0.0036413	0.0038003	0.0041749	0.0069156	0.0225553
7	0.0029366	0.0028427	0.0026044	0.0024617	0.0026194	0.0026404	0.0091596	0.0014505	0.0034871
8	0.0030084	0.0068331	0.0073598	0.0057864	0.0067727	0.0051398	0.0112893	0.0051215	0.0084238
9	0.0024074	0.0063557	0.0021918	0.0023827	0.00192	0.0022097	0.0070657	0.0017724	0.0037579
10	0.0014646	0.0020357	0.0014203	0.0013562	0.0014085	0.0012542	0.0098941	0.0008195	0.0018103
11	0.0028141	0.0030217	0.0045188	0.003851	0.0033914	0.0042758	0.0103932	0.0018801	0.0056214
12	0.0016502	0.0039212	0.0032263	0.0031156	0.0022854	0.0027373	0.0060878	0.0011181	0.0021965
13	0.0016482	0.004098	0.0040081	0.004086	0.0039623	0.0034614	0.0047432	0.0024411	0.0039505
14	0.0012285	0.0033796	0.0042178	0.0038217	0.0043313	0.0044617	0.006579	0.0021453	0.004361
15	0.0010405	0.0021742	0.0023255	0.00217	0.0018061	0.0019993	0.008918	0.0007141	0.0011548
16	0.0006021	0.001872	0.0021013	0.0019843	0.001795	0.0018571	0.0052272	0.0007761	0.0006102

Just as with the SVD inverse results, contour plots were also made of K values plotted against elevation and the radial distance between wells for the data constrained by the HRST results. The HRST values are used at the left and right ends of the plot, with the source on the left and the receiver on the right. Interwell K values in the following plots were all determined by the constrained SVD analysis. The phase is a ratio between S_s and K, so changes in S_s will also result in changes in K. This introduces a potential source of error because, due to the difficulty of measuring S_s in situ, a value was obtained from the literature rather than from field measurements. To investigate the effect of S_s, the constrained SVD analysis was conducted on all of the data using S_s values of both 10^{-5} (Figures 42-49) and 1.5×10^{-5} (Figures 50-57). A value of 1.5×10^{-5} in general results in smoother transitions between zones. The negative aspect of choosing the higher S_s value is that well pair HT-6 to HT-3, which already had higher than expected K values with the lower S_s (Figure 49), continues to increase above the expected range (Figure 57).

Based on other work at the site, and in particular HRST, K values at the site are known to range from approximately 0.0003 m/s up to 0.003 m/s. The K values in Figures 42 and 50 are all within this range. The trend also matches that seen in HRST results, with low K material near the top, a high K region in the middle, another high K region beginning at the bottom of the plot, and a low K zone between the two high K regions. The data set from HT-3 to HT-2 was once again used to verify that the program was working correctly before extending the analysis to other well pairs.

Figure 50, using a value of 1.5×10^{-5} for S_s, shows a smoother transition between points than Figure 42, which is physically a more likely scenario.

Plots were also made of the HT-3 to HT-2 data set using less than 750 rays to determine if fewer rays can provide the same results. The number of rays in each example was based on the ray path geometry of the other well pairs. The 270 ray path example used all receiver data for each source used but only every third source location, just like well pair HT-6 to HT-3. Similarly, the 170 ray path example followed the same pattern as well pair HT-5 to HT-3 and the 90 ray path example followed the pattern of well pair HT-4 to HT-3. The three following figures (Figures 43-45) show the same general trend seen in Figure 42, but the magnitudes of the K values decrease as the number of ray paths decreases. The 270 ray path scenario (Figure 43) is closest to the 750 ray path scenario. The bottom zone is about the same in the 750 and 270 ray path cases, but the K values in the bottom zone are noticeably smaller in the two cases with less ray paths. The plots using the higher S_s value (Figures 51-53) also show the same trends, but the transitions between zones are smoother.

The data set presented in Figure 46 is not as accurate as the other data sets. The amount of error between calculated and observed phases was greater than that in other well pairs. As stated previously, the problems with this data set are likely caused by the nitrogen leaks at the time of data collection. In spite of the problems, the plot shows the same general zones of high and low K seen elsewhere. Figure 54, using the larger Ss value, depicts the same zones of high and low K. The processing

program is probably not causing the problems because it has been constrained and other well pairs do not have as many problems. So, drawing definite conclusions about this well pair would likely require recollecting the data with the current repaired equipment.

Both of the initial well pairs verified the constrained processing program by showing the trends observed in HRST results, so the data from fall 2007 were then examined for the three newest wells. The vertical intervals were varied in the source and receiver wells for some of the wells pairs and offered the opportunity to determine if data were being collected at adequate spatial intervals for appropriate resolution. The data in Figures 47 and 55 show the overall trend observed between HT-3 and HT-2 and between HT-3 and HT-1. Once again, the plots demonstrate the expected trends of high and low K zones. The high K zone near the top of the plot is not seen elsewhere in that portion of the aquifer, but the values are at least within the overall range determined by other methods. This could potentially be caused by a combination of previously discussed problems of resolution in the top portion of the sampling area in combination with the low number of ray paths used for this particular well pair (100, compared to 750 for HT-3 to HT-2).

The results between well HT-5 and well HT-3 are presented in Figures 48 and 56. The difference between the two figures is that the transitions between K values are smoother in the plot using the higher value for S_s. Some of the values at the bottom of the plot are slightly above the general expected range, but still within reason. K values have been shown to slightly exceed 0.003 m/s in some of the HRST

data toward the bottom of the wells. The same trend of low K material at the top, a moderately high K zone in the middle, and high K material at the bottom is again observed in this well pair. As with the plot from well HT-4 to well HT-3, the relatively large region of very low K values at the top could be due to the lower number of ray paths for this well pair.

The contour plots from well HT-6 to HT-3 (Figures 49 and 57) show the same trend seen in tomography experiments between all the other well pairs, as well as in HRST results. The zone of very high K in the middle left side of the plot exceeds the range of expected values for the site. The location of the zone could be due to the survey design for this well pair, namely, the source locations were sampled at a coarser interval than that used for the receiver locations. This well pair is the only one examined in this study for which increasing S_s resulted in K values farther above the expected range. Despite the problem of larger than expected K values, the transitions between zones are again smoother using 1.5×10^{-5} instead of 10^{-5} for S_s.

The number of ray paths collected for a well pair correlated well with the reasonableness of the K values. The well pair with the best results, HT-3 to HT-2 (750 rays) was characterized by the most rays of any of the well pairs, with the exception of the well pair with equipment problems. The well pairs of HT-4 to HT-3 and HT-5 to HT-3 had 100 rays and 190 rays, respectively, and some of the higher elevation zones were somewhat lower than expected for the site. The results suggest that 190 ray paths are not enough for accurate results. Time constraints may not always allow for 750 ray paths, but there does seem to be a strong correlation with the

accuracy of the processing results and the number of ray paths. The work with editing ray paths for the data set from HT-3 to HT-2 also lends support for collecting as many ray paths as time permits. The resolution of K values decreased as more rays were edited out. Although it takes less time to collect 300 ray paths than to collect 750 ray paths, the additional rays will provide some increase in accuracy.

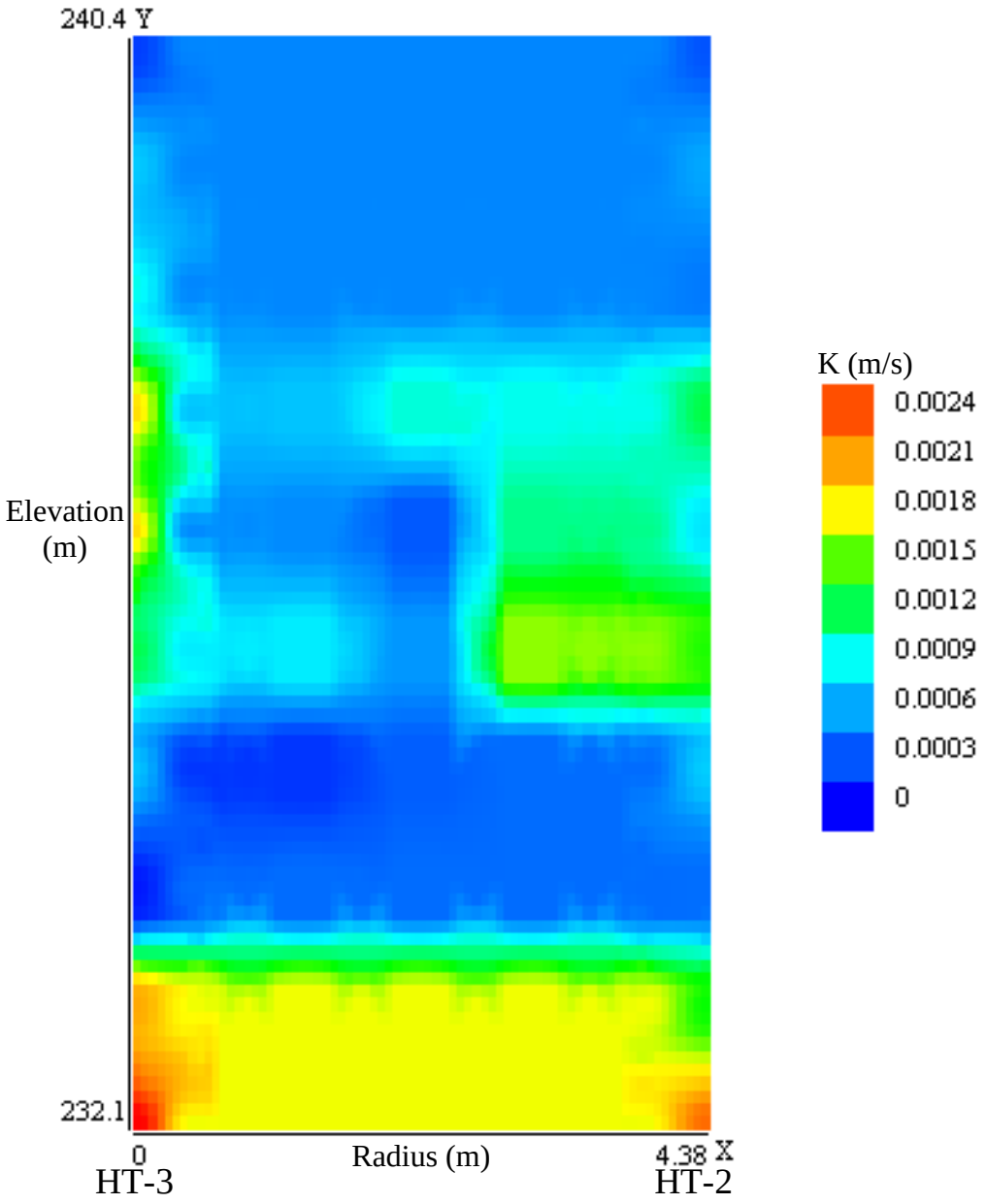

Figure 42: Interwell K values from constrained SVD analysis with HT-3 as the source well and HT-2 as the receiver well (750 rays, $S_s = 10^{-5}$).

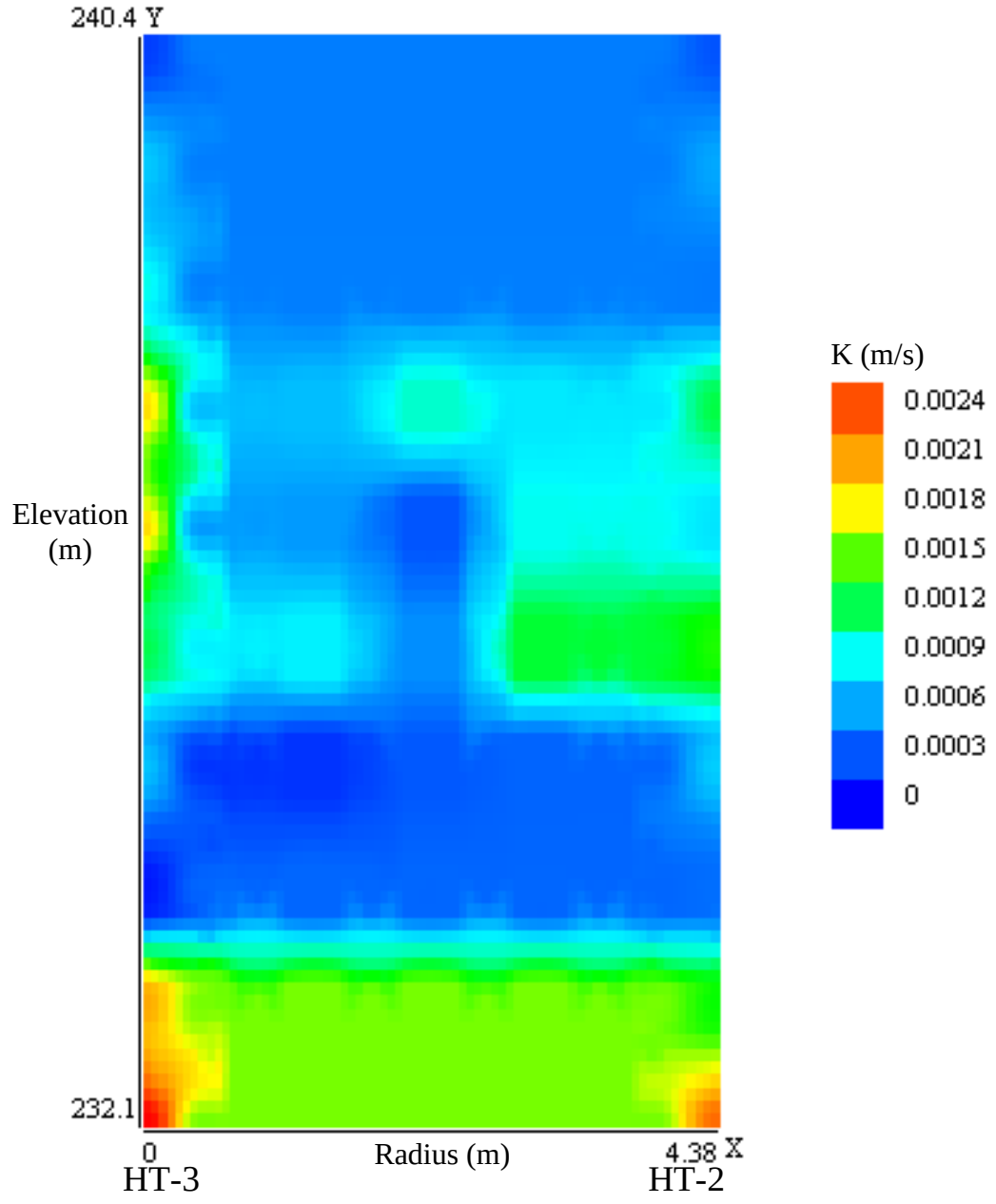

Figure 43: Interwell K values from constrained SVD analysis with HT-3 as the source well and HT-2 as the receiver well (270 rays, $S_s = 10^{-5}$).

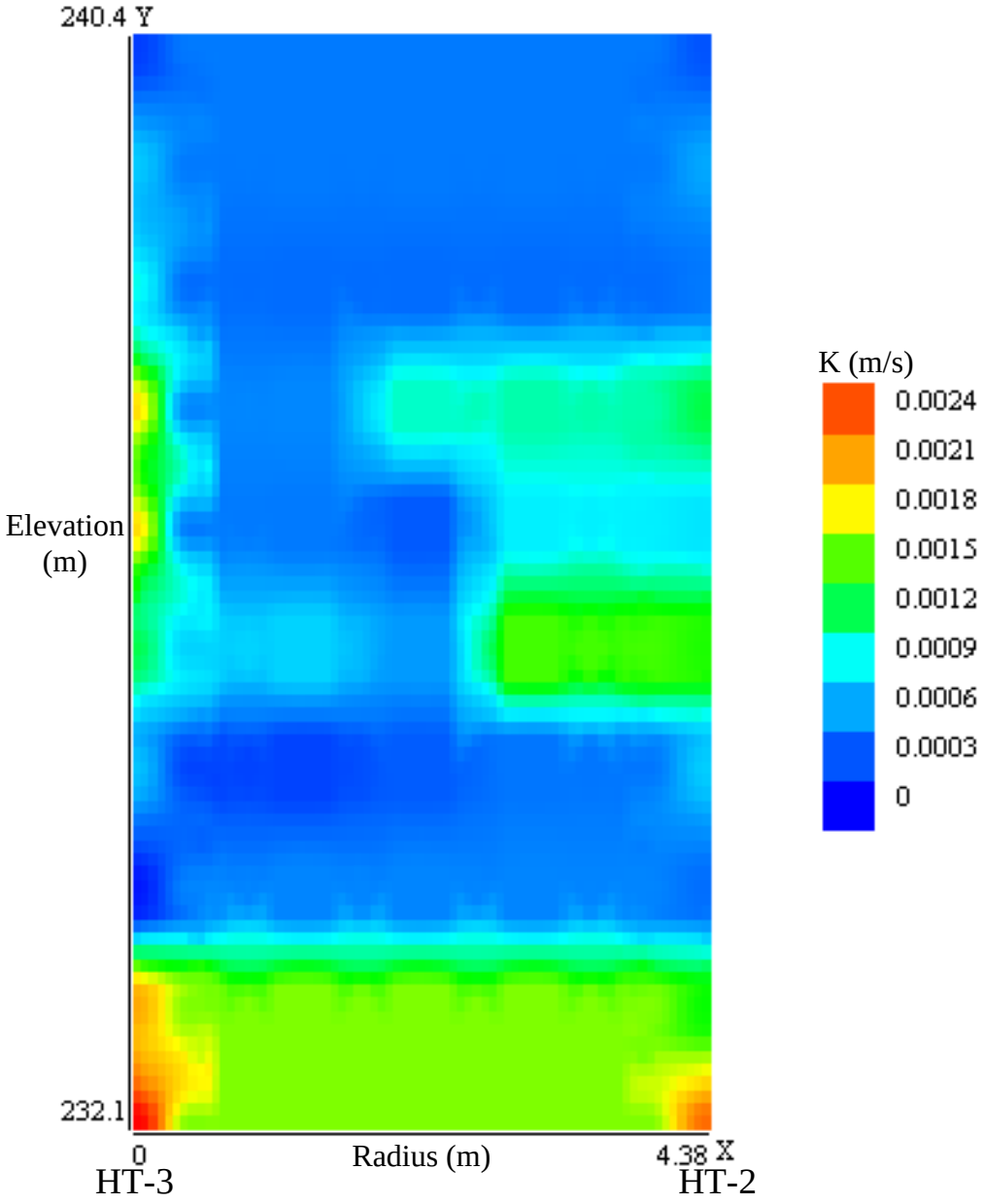

Figure 44: Interwell K values from constrained SVD analysis with HT-3 as the source well and HT-2 as the receiver well (170 rays, $S_s = 10^{-5}$).

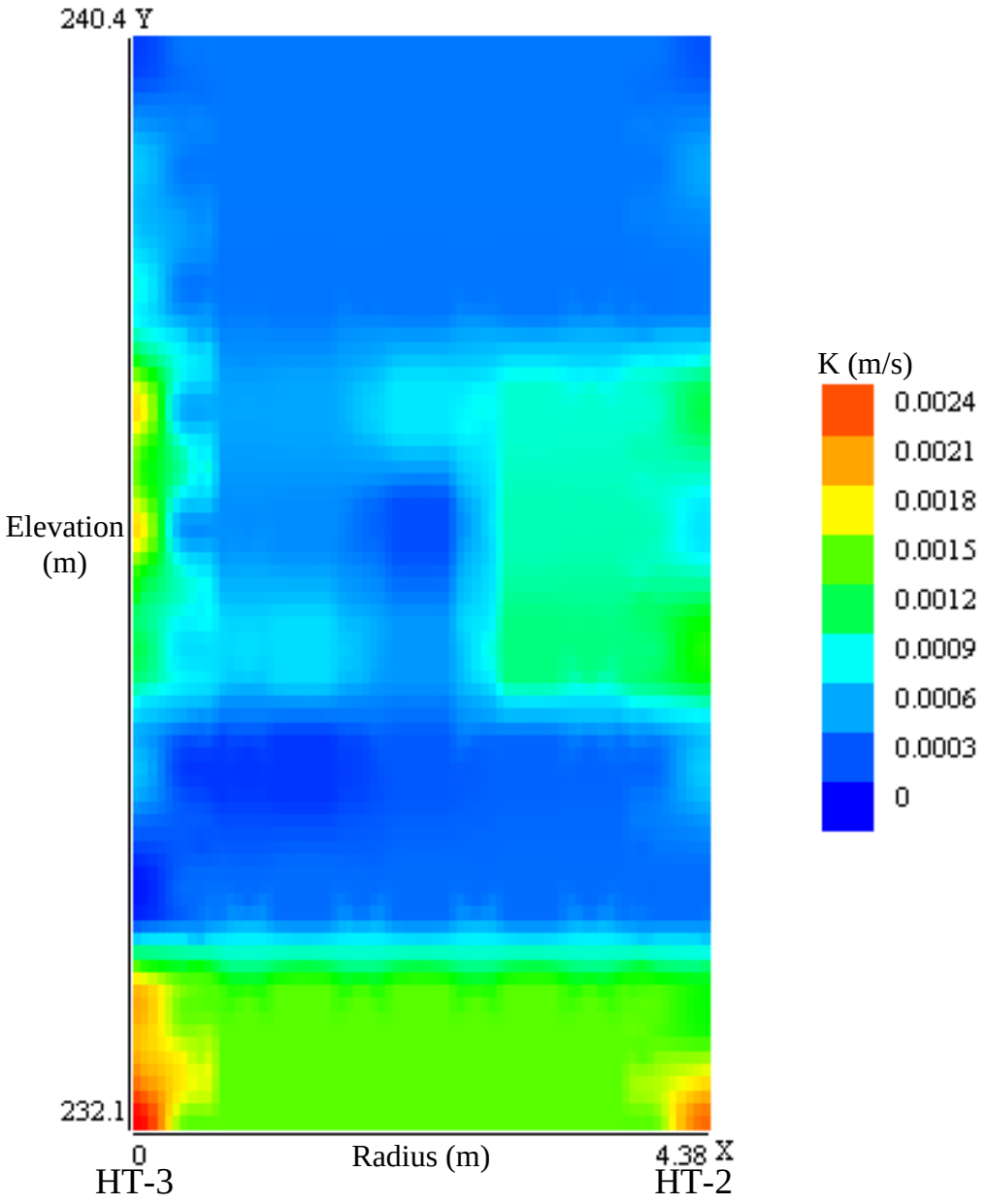

Figure 45: Interwell K values from constrained SVD analysis with HT-3 as the source well and HT-2 as the receiver well (90 rays, $S_s = 10^{-5}$).

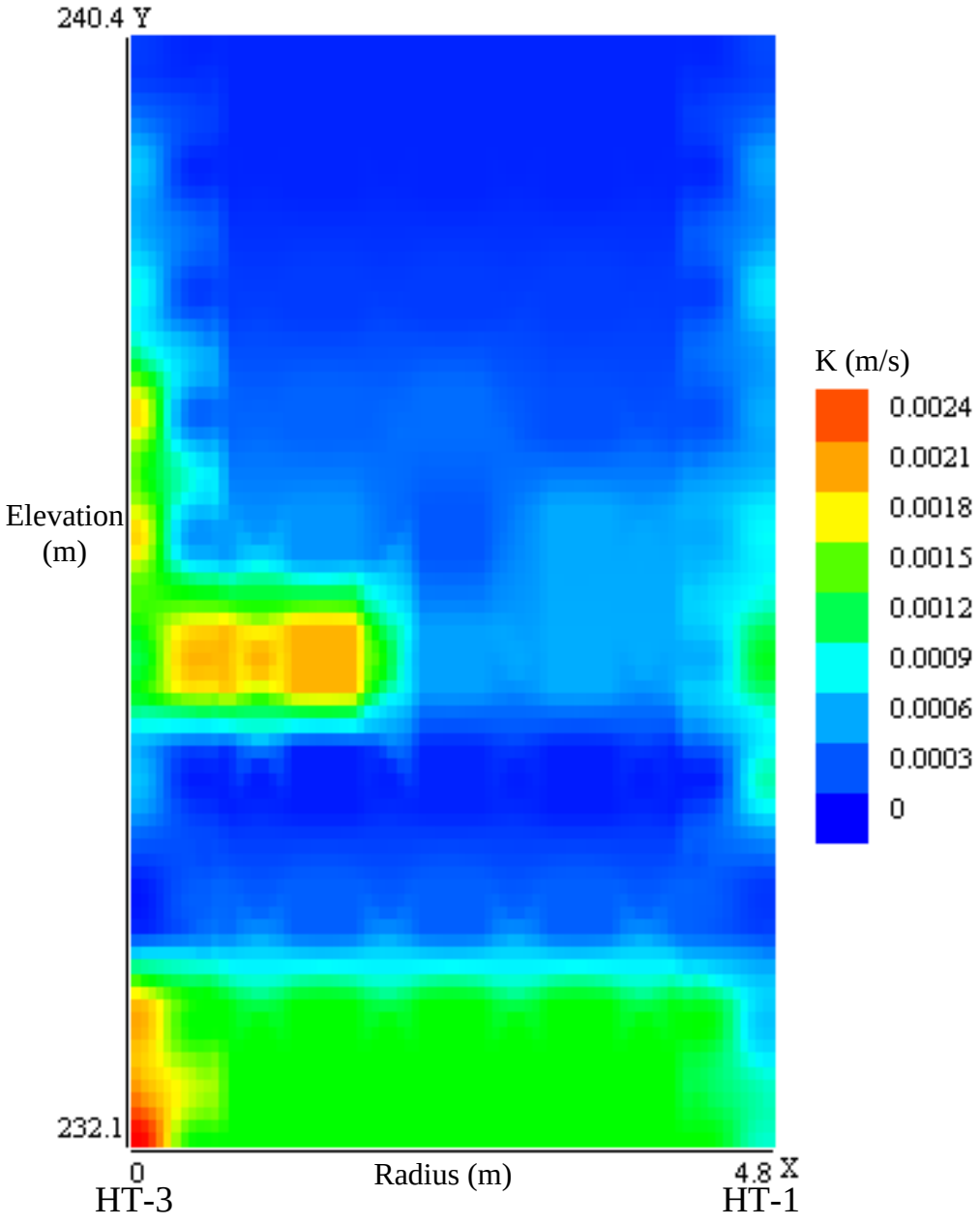

Figure 46: Interwell K values from constrained SVD analysis with HT-3 as the source well and HT-1 as the receiver well ($S_s = 10^{-5}$).

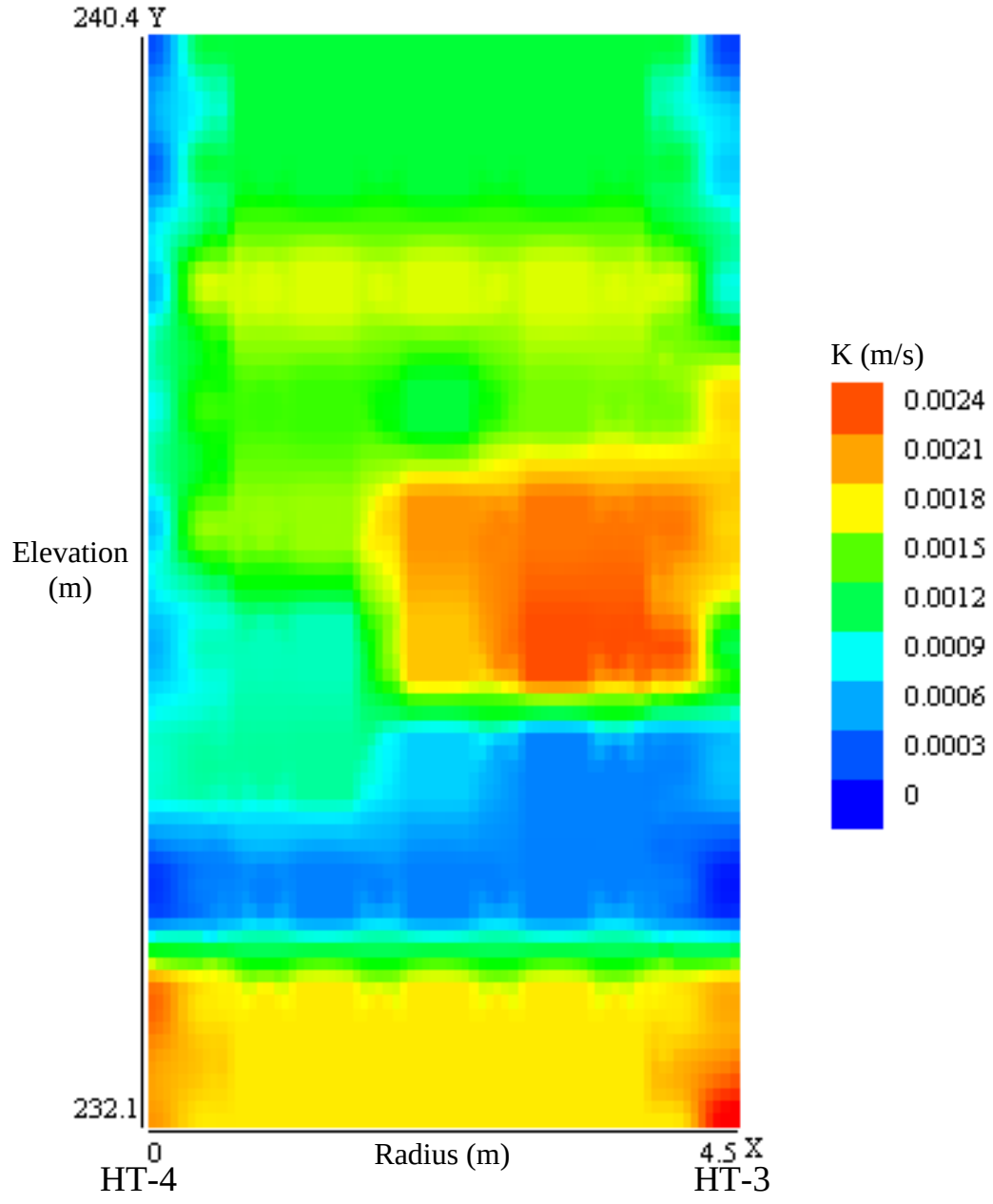

Figure 47: Interwell K values from constrained SVD analysis with HT-4 as the source well and HT-3 as the receiver well ($S_s = 10^{-5}$).

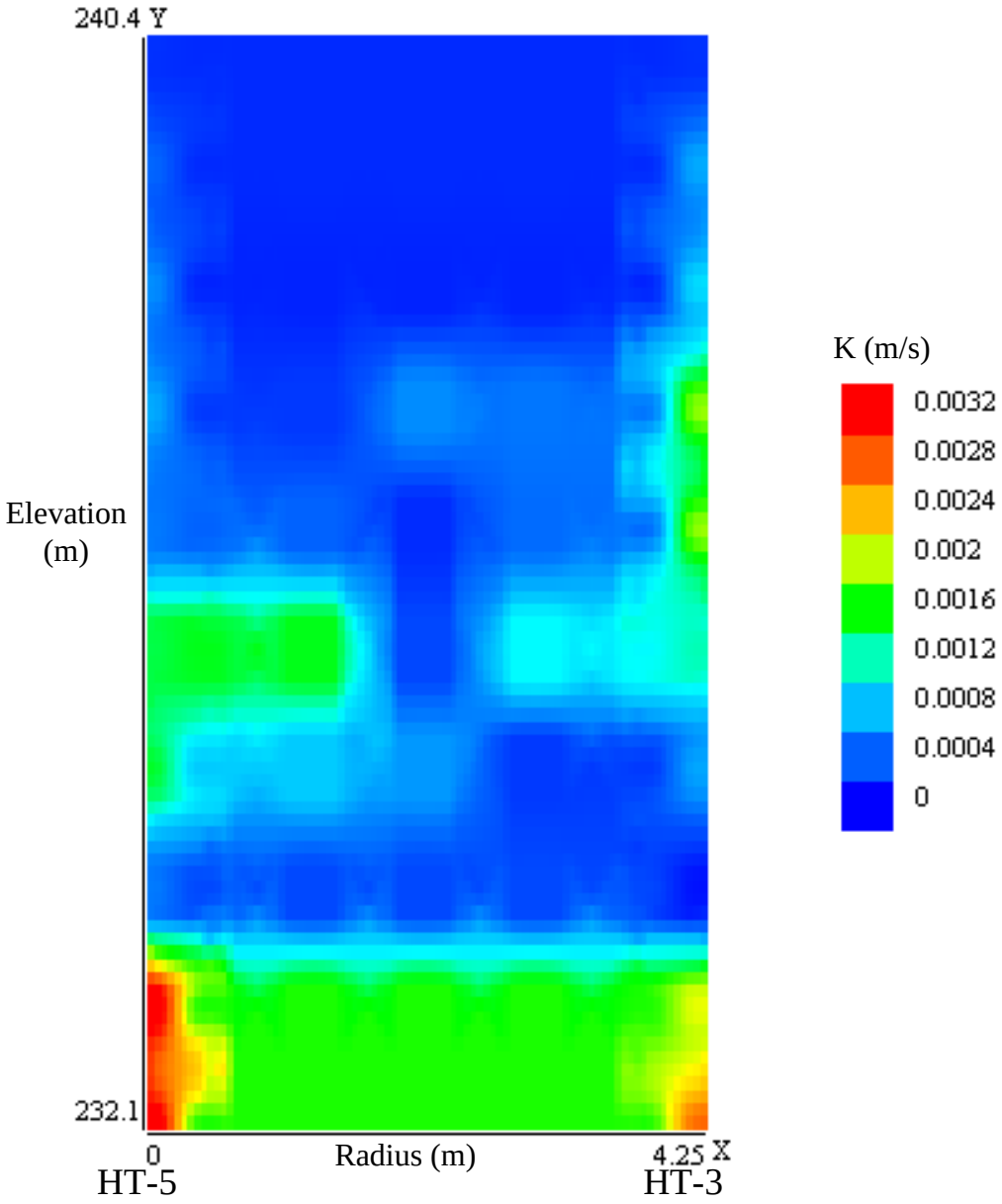

Figure 48: Interwell K values from constrained SVD analysis with HT-5 as the source well and HT-3 as the receiver well ($S_s = 10^{-5}$).

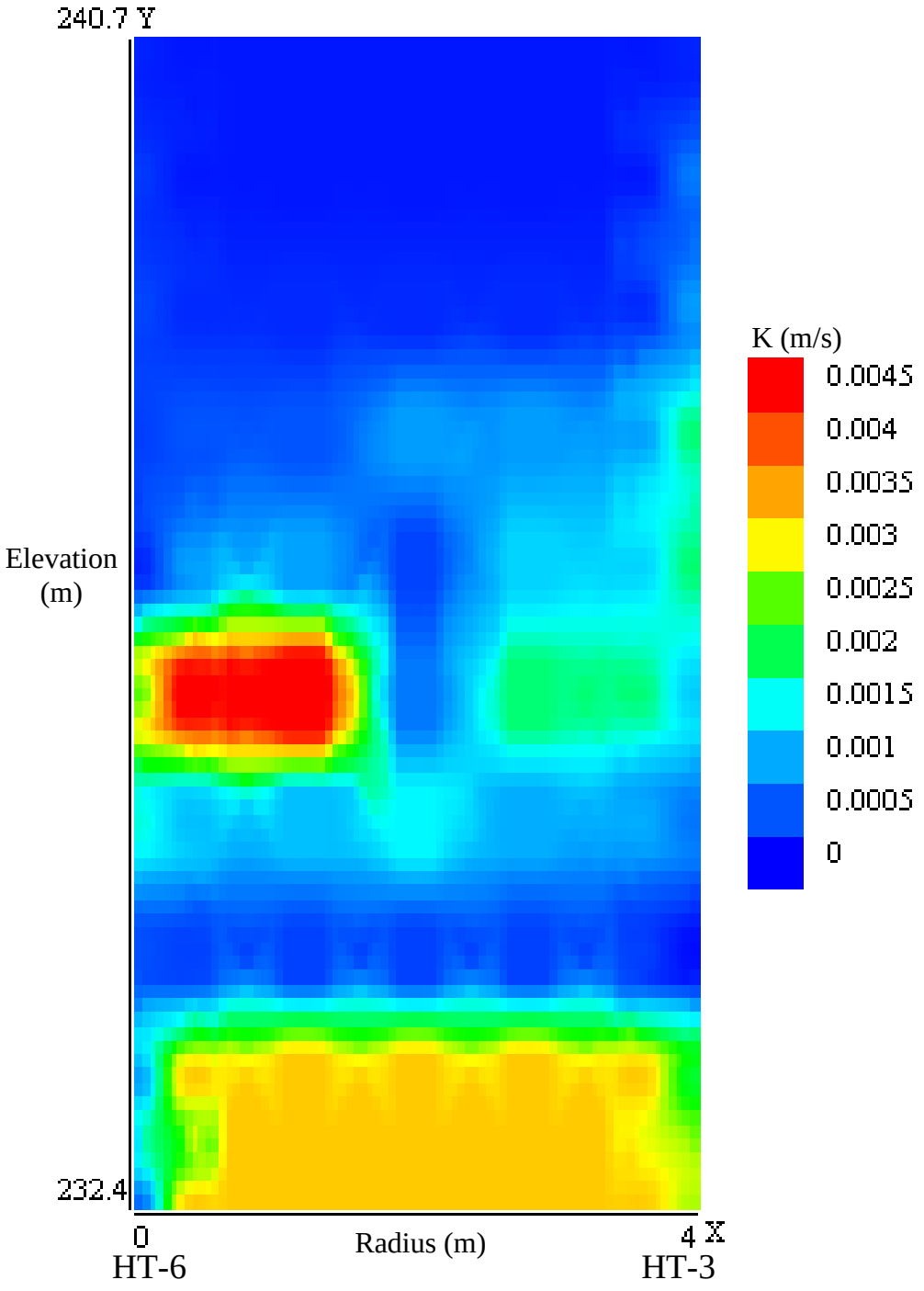

Figure 49: Interwell K values from constrained SVD analysis with HT-6 as the source well and HT-3 as the receiver well ($S_s = 10^{-5}$).

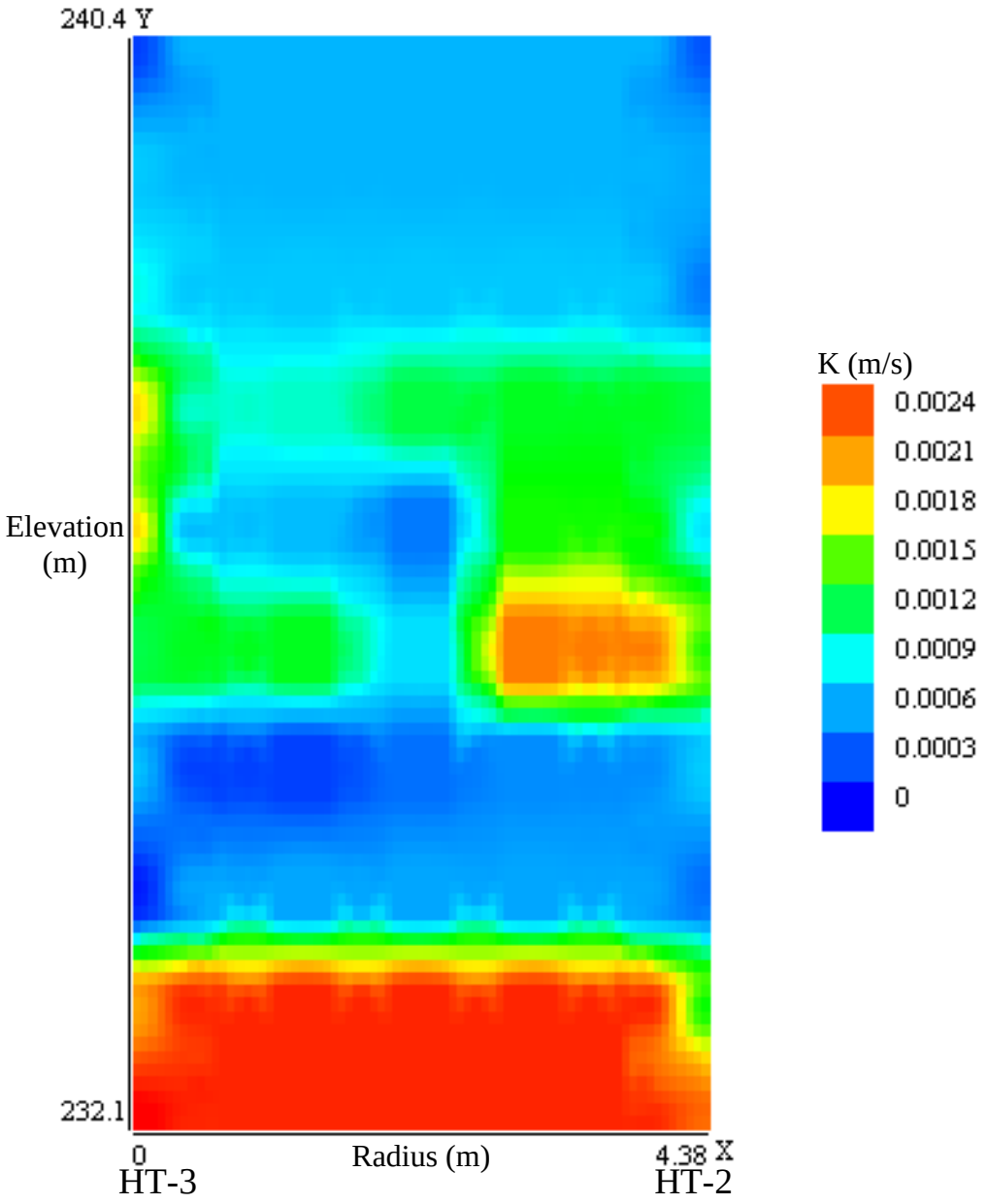

Figure 50: Interwell K values from constrained SVD analysis with HT-3 as the source well and HT-2 as the receiver well (750 rays, $S_s = 1.5 \times 10^{-5}$).

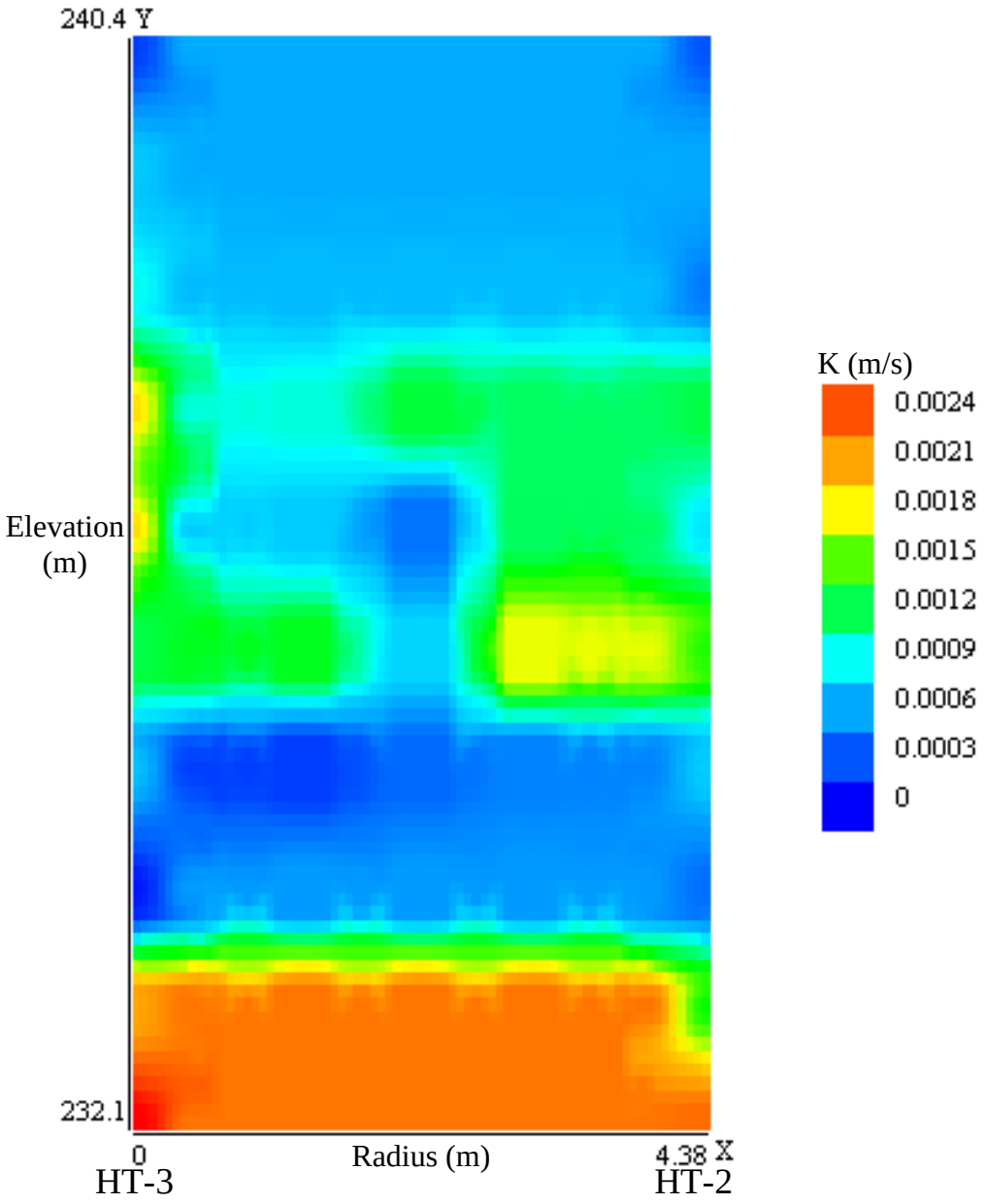

Figure 51: Interwell K values from constrained SVD analysis with HT-3 as the source well and HT-2 as the receiver well (270 rays, $S_s = 1.5 \times 10^{-5}$).

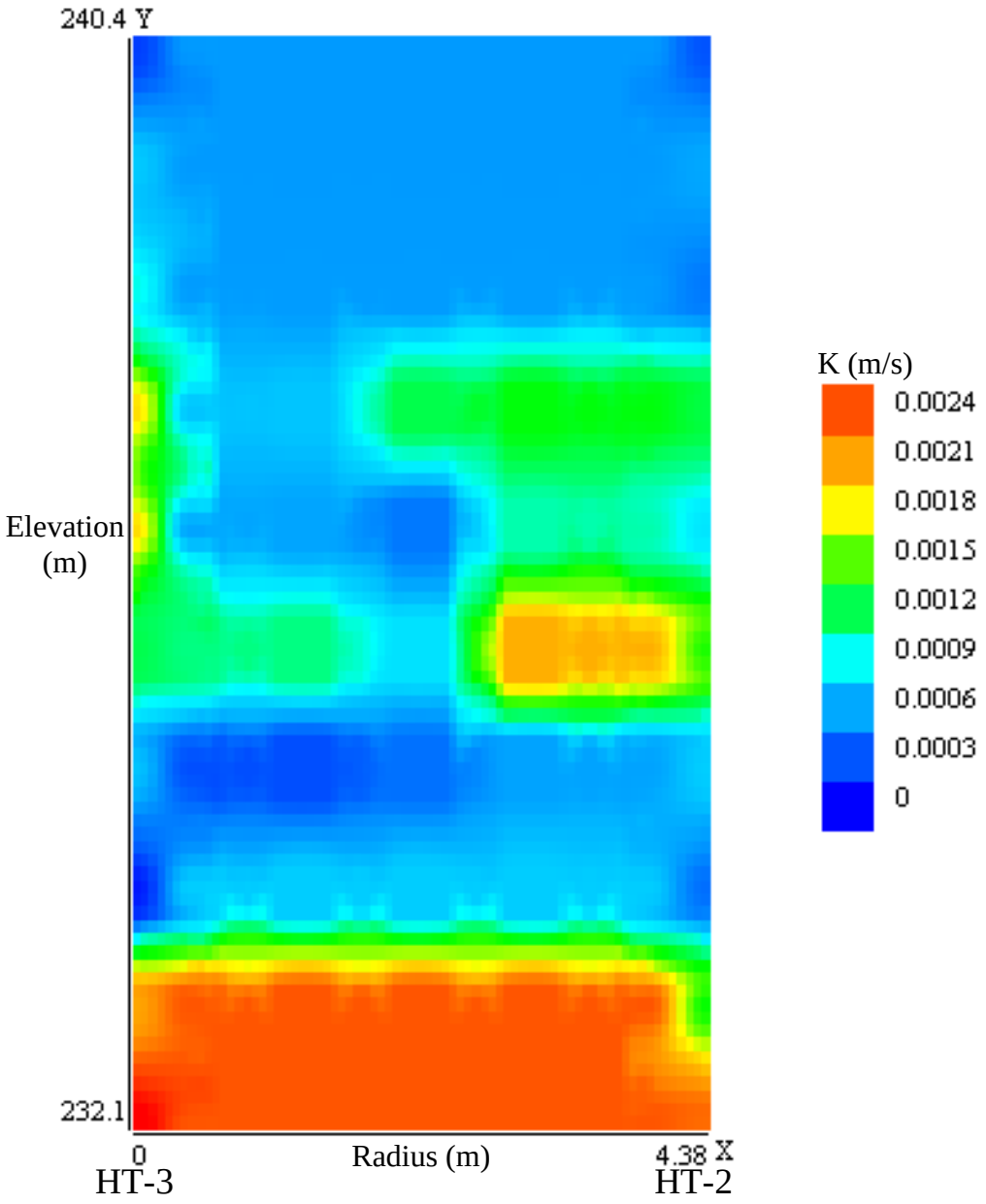

Figure 52: Interwell K values from constrained SVD analysis with HT-3 as the source well and HT-2 as the receiver well (170 rays, $S_s = 1.5 \times 10^{-5}$).

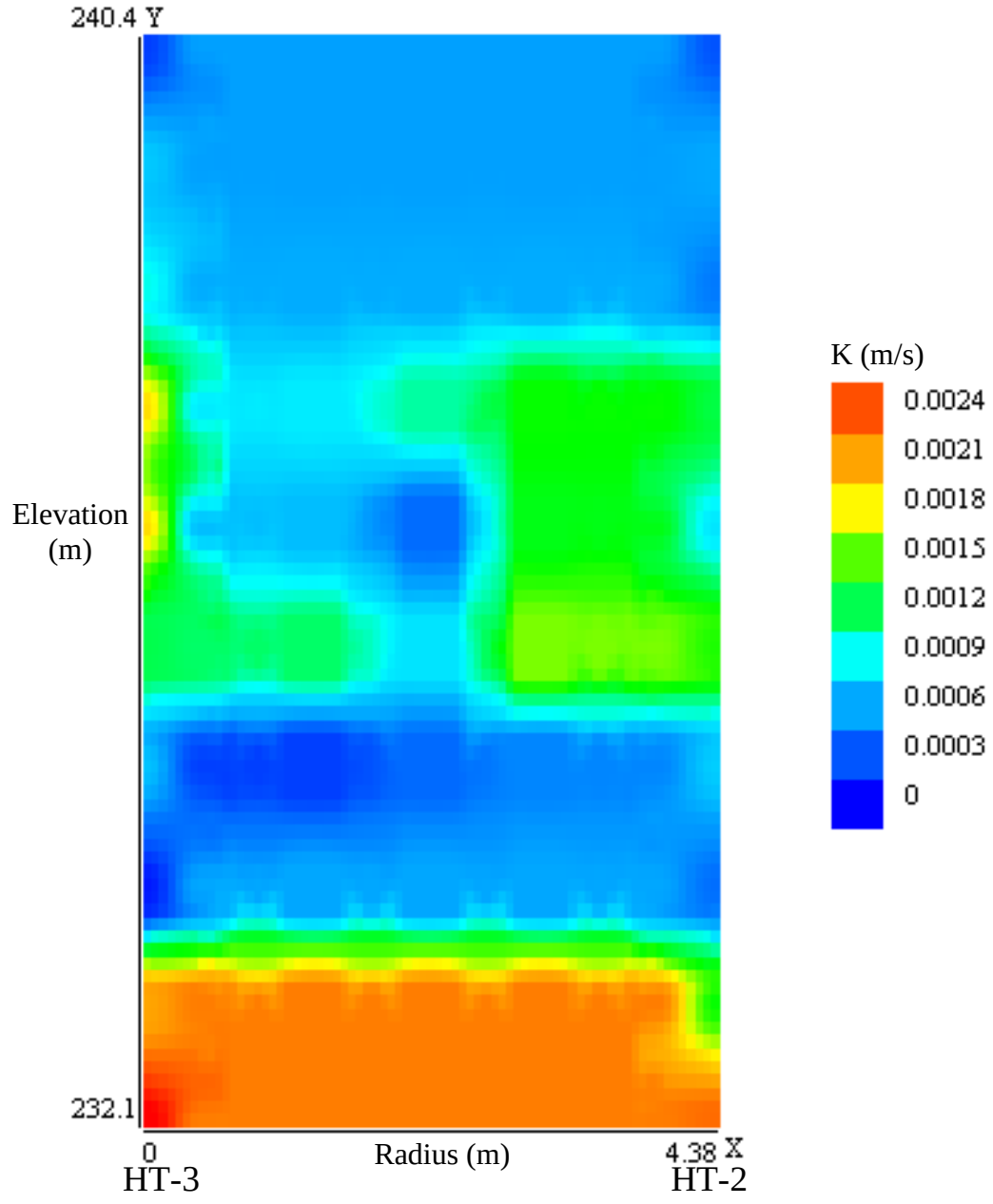

Figure 53: Interwell K values from constrained SVD analysis with HT-3 as the source well and HT-2 as the receiver well (90 rays, $S_s = 1.5 \times 10^{-5}$).

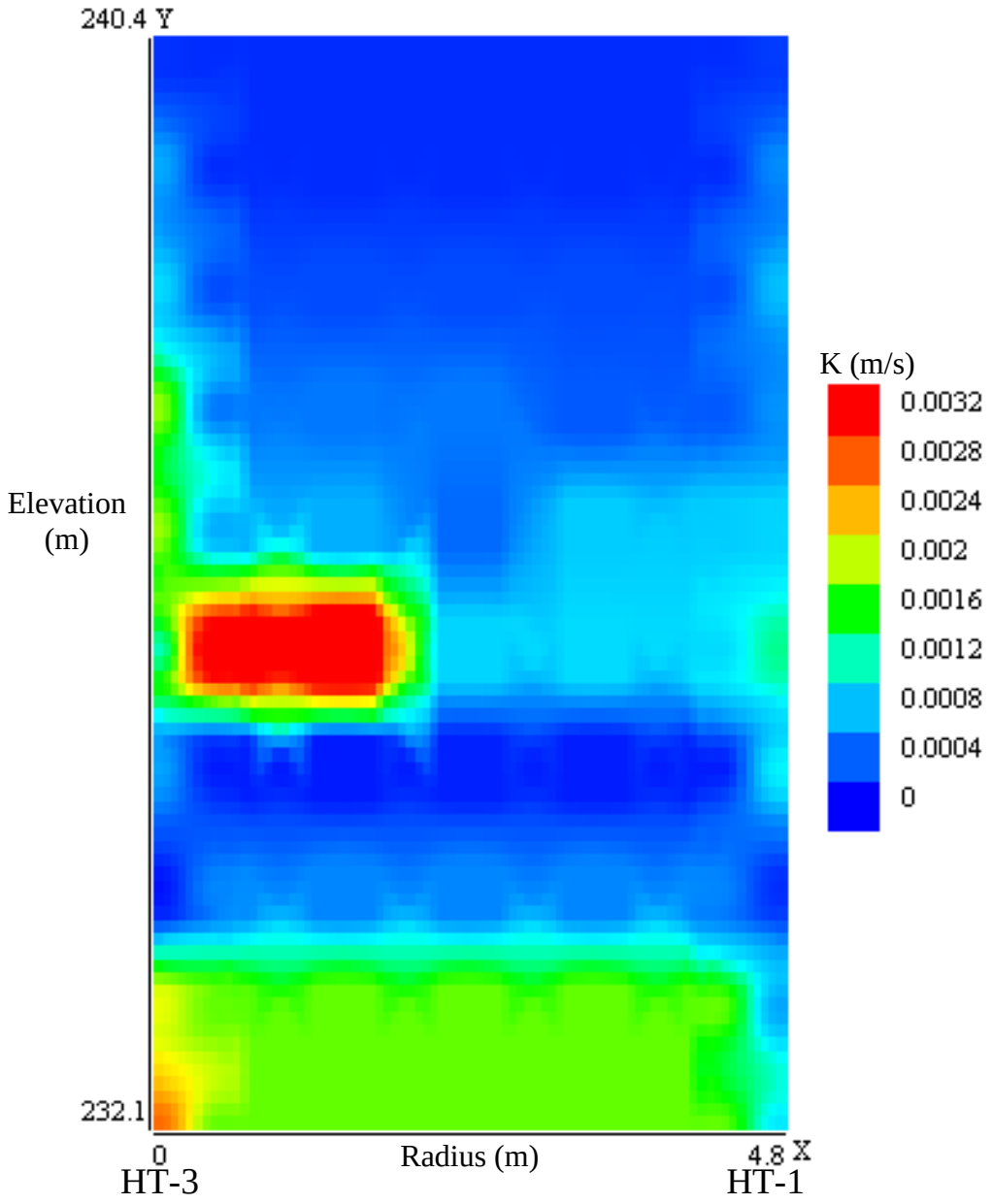

Figure 54: Interwell K values from constrained SVD analysis with HT-3 as the source well and HT-1 as the receiver well ($S_s = 1.5 \times 10^{-5}$).

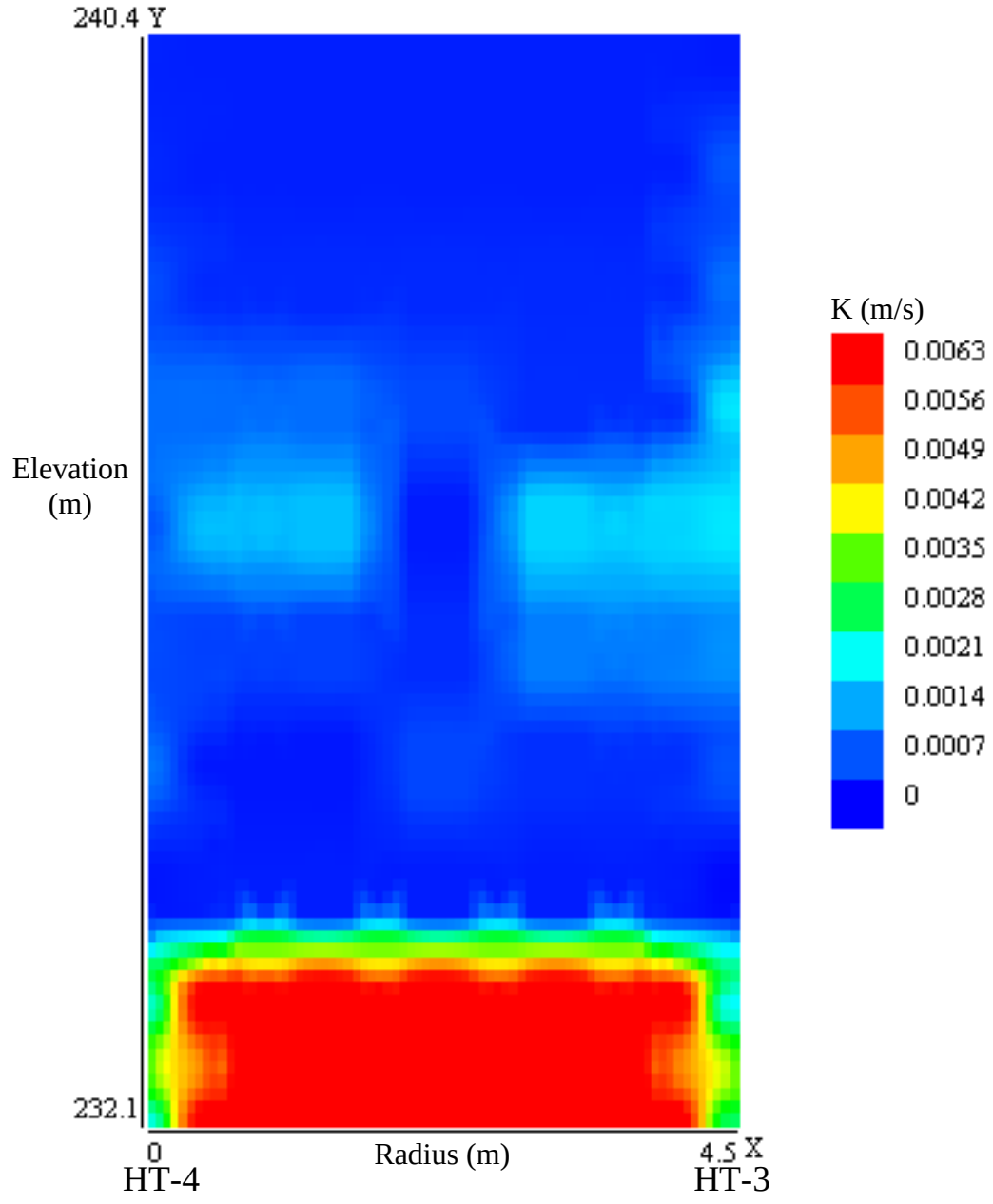

Figure 55: Interwell K values from constrained SVD analysis with HT-4 as the source well and HT-3 as the receiver well ($S_s = 1.5 \times 10^{-5}$).

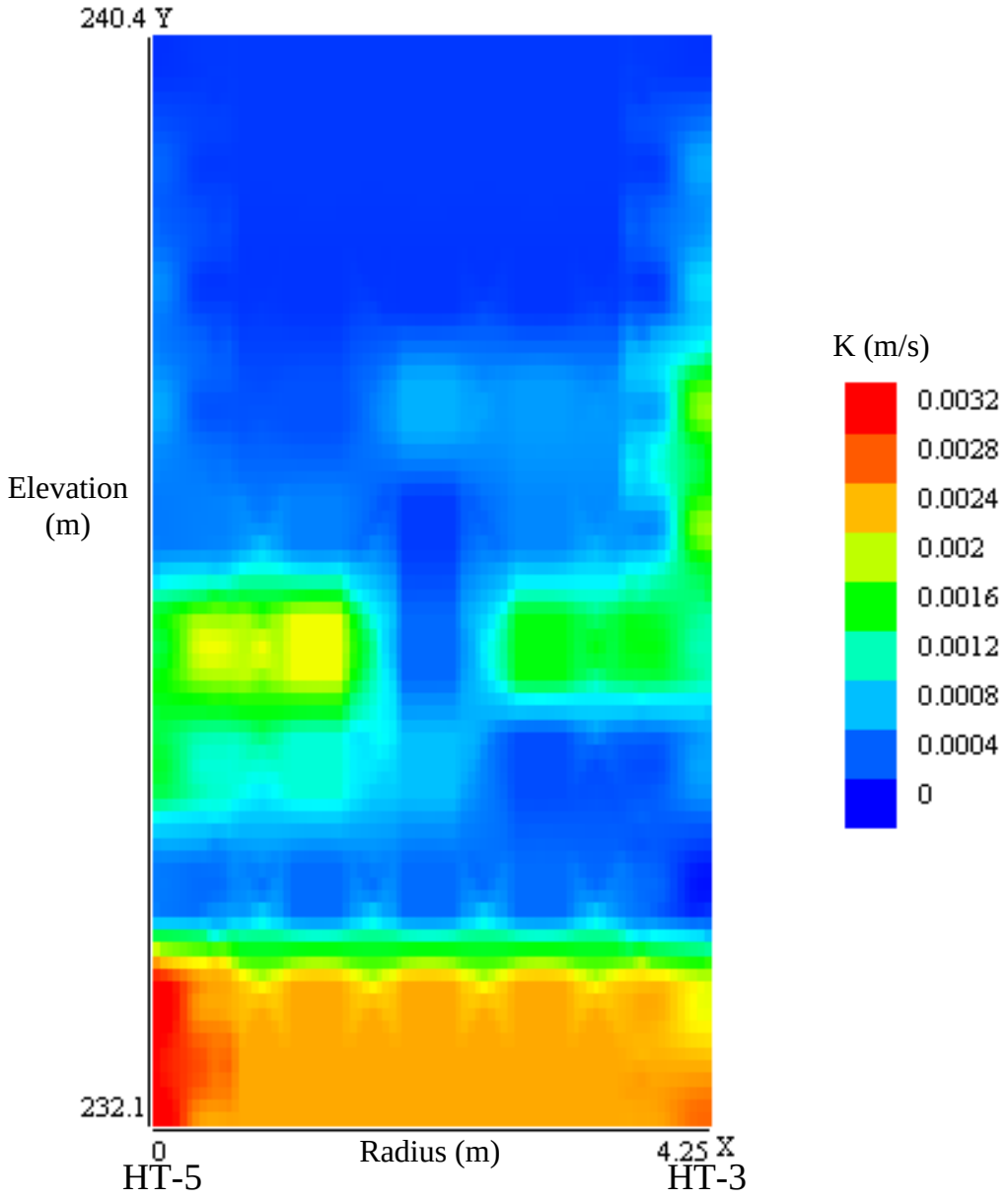

Figure 56: Interwell K values from constrained SVD analysis with HT-5 as the source well and HT-3 as the receiver well ($S_s = 1.5 \times 10^{-5}$).

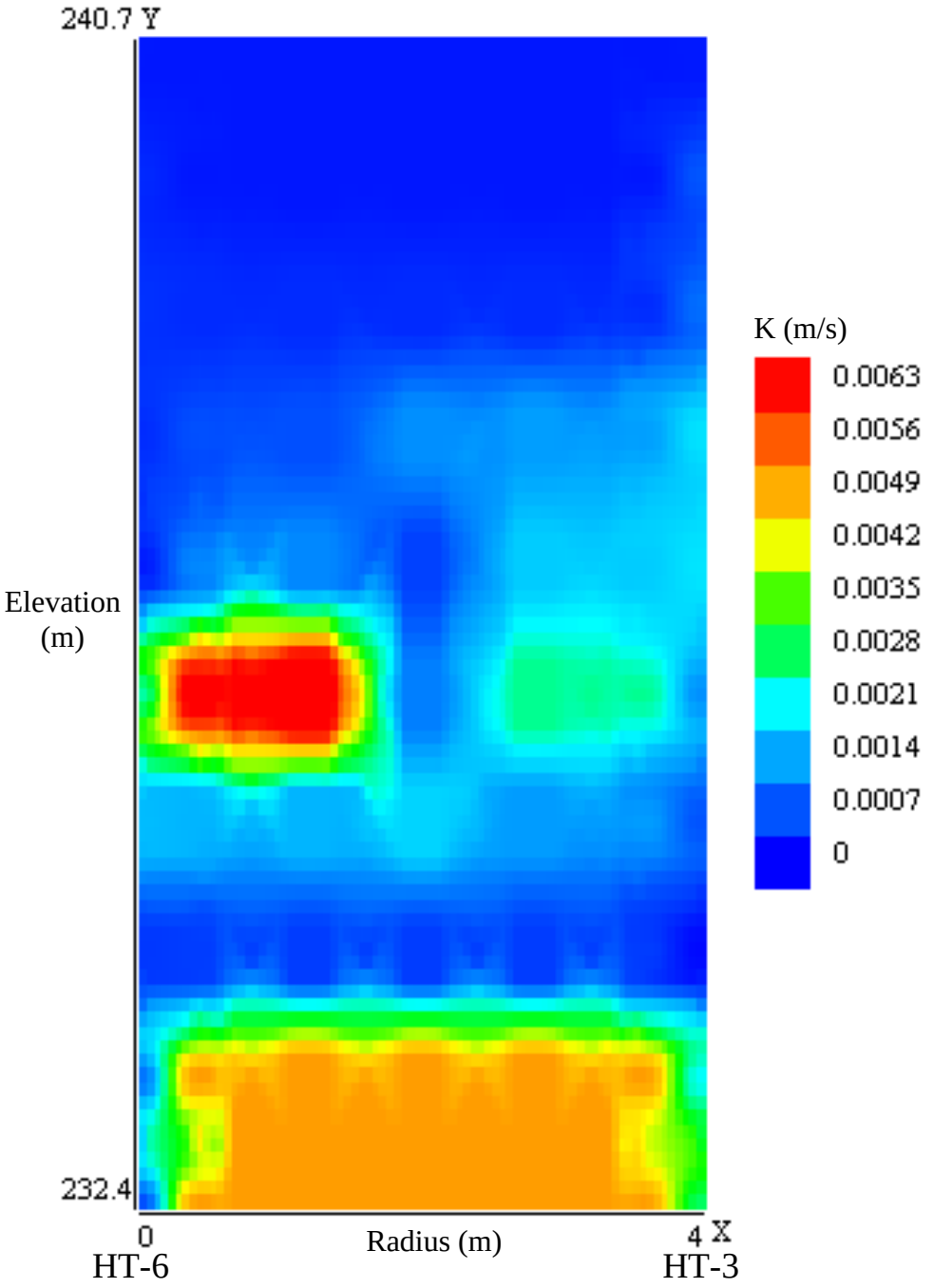

Figure 57: Interwell K values from constrained SVD analysis with HT-6 as the source well and HT-3 as the receiver well ($S_s = 1.5 \times 10^{-5}$).

CHAPTER 4: Summary and Conclusions

The goals of this research were to develop field equipment and time-efficient processing procedures to characterize aquifer parameters using hydraulic tomography with a sinusoidal pressure source. The study consisted of collecting and processing a series of MOGs at a well-studied alluvial aquifer in eastern Kansas. Previous studies at the site focused on obtaining information about K that was specific to the immediate area around the wells, or a large average K value across the entire site. A K value averaged over a large area is useful for water resource problems, but studies at contaminated sites require an understanding of fine-scale heterogeneities in K. Initial data were collected with a single channel receiver, but a multilevel sensor receiver constructed later substantially sped up data collection.

Most hydraulic tomography studies use processing programs that require large amounts of time and processing power for the inversion to K values. The straight ray trace approximation greatly simplifies the processing. The unconstrained SVD inversion program was created and modeling studies were performed using synthetic data to demonstrate that data could be inverted with relatively small amounts of error. Zones could be resolved using the SVD program to dimensions of about one meter. After modeling, the SVD program was run using phase values obtained in the field. K values at the site are known from HRST to range from about 0.000305 m/s to 0.00305 m/s, and follow the general trend of higher K zone at the base of the aquifer, a low K zone above, a moderately high K zone still higher up the profile, and a low K zone at the top. The success or failure of the inversion was evaluated by comparing

the resulting K values to the range of K values seen from HRST as well as the general trends of high or low K zones seen from HRST. The unconstrained analysis showed the general trends from the site, but some K values were orders of magnitude above the expected range. Filtering and editing of rays failed to reduce the magnitude of K values into the expected range. The SVD analysis program was then updated with a weighting factor for HRST results used to constrain the inversion. The constrained SVD analysis produced both the expected trends of high and low K zones as well as K values within the expected range.

The success of the inversion seems to be correlated with the number of ray paths between the source and receiver wells. Varying source and receiver intervals for each well pair offered the opportunity to examine how much data needed to be collected. Initial data were collected at too fine a scale (0.305 m) given the resolution capabilities of the model, yet two of the later well pairs did not have enough ray paths to adequately characterize the area (using a 0.914 m collection interval). Varying the number of ray paths used in the initial well pair verified this conclusion. Of the variations tested in this study, the geometry used for GEMS was most efficiently and accurately characterized with 300 ray paths, but 750 ray paths will provide some additional accuracy if time is available for their collection.

The goals of the research were successfully achieved. The field equipment and processing programs developed reduced the time needed to get K values from a hydraulic tomography study. Five well pairs were analyzed and all had reasonable interwell K distributions after using the constrained inversion, as compared to the

general range seen with HRST. The small problems with some well pairs can be explained by equipment problems in one case and by too few ray paths in another two cases. The results of this research show that hydraulic tomography combined with appropriate inversion programs can estimate interwell K distributions with resolutions down to about one square meter in the most sensitive regions. Future studies with the GEMS data will focus on continuing to refine the field and processing techniques.

References

Aster, R.C., Borchers, B., and Thurber, C.H., 2005, Parameter Estimation and Inverse Problems, Elsevier Academic Press, Burlington, MA.

Bohling, G.C., 1999, Evaluation of an induced gradient tracer testing an alluvial aquifer, Ph.D. Dissertation, The University of Kansas, 224 p.

Bohling, G.C., Butler, Jr., J.J., Zhan, X., and Knoll, M.D., 2007, A field assessment of the value of steady shape hydraulic tomography for characterization of aquifer heterogeneities: Water Resources Research 43, W05430, 1-23.

Brauchler, R., Cheng, J.-T., Dietrich, P., Everett, M., Johnson, B., Liedl, R., and Sauter, M., 2007, An inversion strategy for hydraulic tomography: Coupling travel time and amplitude inversion: Journal of Hydrology 345, 184-198.

Butler, Jr., J.J., McElwee, C.D., and Bohling, G.C., 1999, Pumping tests in networks of multilevel sampling wells: Motivation and methodology: Water Resources Research 35(11), 3553-3560.

Engard, B., 2006, Estimating Aquifer Parameters From Horizontal Pulse Tests, Master's Thesis, The University of Kansas, 107 pp.

Fetter, C.W., 2001, Applied Hydrogeology, 4th Ed., Prentice-Hall, Upper Saddle River, New Jersey.

Hao, Y., Yeh, T.-C. J., Xiang, J., Illman, W.A., Ando, K., Hsu, K.-C., and Lee, C.-H., 2007, Hydraulic tomography for detecting fracture zone connectivity: Ground Water 46(2), 183-192.

Healey, J., McElwee, C., and Engard, B., 2004, Delineating hydraulic conductivity with direct-push electrical conductivity and high resolution slug testing, American Geophysical Union Poster H23A-1118.

Huettl, T.J., 1992. An evaluation of a borehole induction single-well tracer test to characterize the distribution of hydraulic properties in an alluvial aquifer. Masters Thesis, The University of Kansas.

Hvorslev, M.J., 1951, Time lag and soil permeability in groundwater observations, US Army Corps of Engineers Waterways Experimental Station, Bulletin 36.

Illman, W.A., Liu, X., and Craig, A., 2007, Steady-state hydraulic tomography in a laboratory aquifer with deterministic heterogeneity: Multi-method and multiscale validation of hydraulic tomography tomograms: Journal of Hydrology 341, 222-234.

Illman, W.A., Craig, A.J., and Liu, X., 2008, Practical issues in imaging hydraulic conductivity through hydraulic tomography: Ground Water 46(1), 120-132.

Karasaki, K., Freifeld, B., Cohen, A., Grossenbacher, K., Cook, P., and Vasco, D., 2000, A multidisciplinary fractured rock characterization study at Raymond field site, Raymond, CA: Journal of Hydrology 236, 17-34.

Lane, Jr., J.W., Day-Lewis, F.D., and Casey, C.C., 2006, Geophysical monitoring of a field-scale biostimulation pilot project: Ground Water 44(3), 430-443.

Li, W., Englert, A., Cirpka, O.A., Vanderborght, J., and Vereecken, H., 2007, Two-dimensional characterization of hydraulic heterogeneity by multiple pumping tests: Water Resources Research 43, W04433, 1-13.

Liu, X., Illman, W.A., Craig, A.J., Zhu, J., and Yeh, T.-C. J., 2007, Laboratory sandbox validation of transient hydraulic tomography: Water Resources Research 43, W05404, 1-13.

McElwee, C.D., 2000, Implementation of a nonlinear model for analysis of slug tests, Kansas Geological Survey Computer Program Series 2000-01.

McElwee, C.D., and Zemansky, G.M., 2005, Effect of a mobile fine fraction on slug test results: Natural Resources Research 14(1), 31-37.

O'Connor, H.G., 1992, Geologic map, Douglas County: Kansas Geological Survey, Map M-26, scale 1:50,000, 33 x 31 inches.

Prosser, D.W., 1981, A method of performing response tests on highly permeable aquifers: Ground Water 19(6), 588-592.

Ross, H.C., 2005, Utility of multi level slug tests to define spatial variations of hydraulic conductivity in an alluvial aquifer, northeastern Kansas, Masters Thesis, The University of Kansas.

Ross, H.C., and McElwee, C.D., 2007, Multi-level slug tests to measure 3-D hydraulic conductivity distributions: Natural Resources Research 16(1), 67-79.

Sellwood, S., 2001. A direct-push method of hydrostratigraphic site characterization. Masters thesis, The University of Kansas.

Shepp, L.A., and Kruskal, J.B., 1978, Computerized tomography: The new medical x-ray technology: The American Mathematical Monthly 85(6), 420-439.

Straface, S., Fallico, C., Troisi, S., Rizzo, E., and Revil, A., 2007, An inverse procedure to estimate transmissivity from heads and SP signals: Ground Water 45(4), 420-428.

Thorton, D., S. Ita, and K. Larsen. 1997, Broader use of innovative ground water access technologies, In Proceedings of Superfund XVIII Conference, vol. 2.

Watson, D.B., Doll, W.E., Gamey, T.J., Sheehan, J.R., and Jardine, P.M., 2005, Plume and lithologic profiling with surface resistivity and seismic tomography: Ground Water 43(2), 169-177.

Yeh, T.-C. J., and Liu, S., 2000, Hydraulic tomography: development of a new aquifer test method: Water Resources Research 36(8), 2095-2105.

Yeh, T.-C. J., and Zhu, J., 2007, Hydraulic/partitioning tracer tomography for characterization of dense nonaqueous phase liquid source zones: Water Resources Research 43, W06435, 1-16.

APPENDIX A: HRST K Profiles

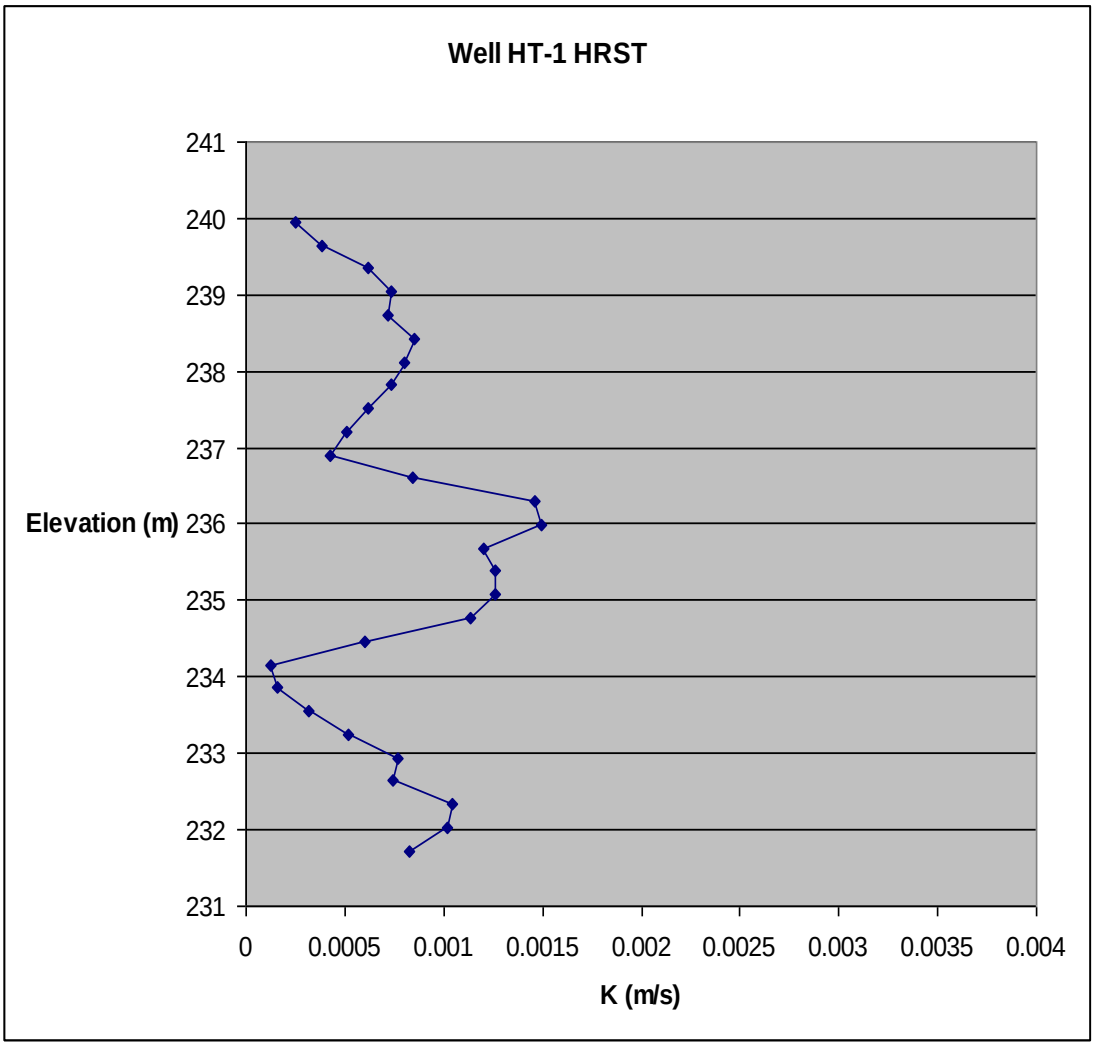

Figure 58: HRST results for well HT-1 (processed by Brett Engard).

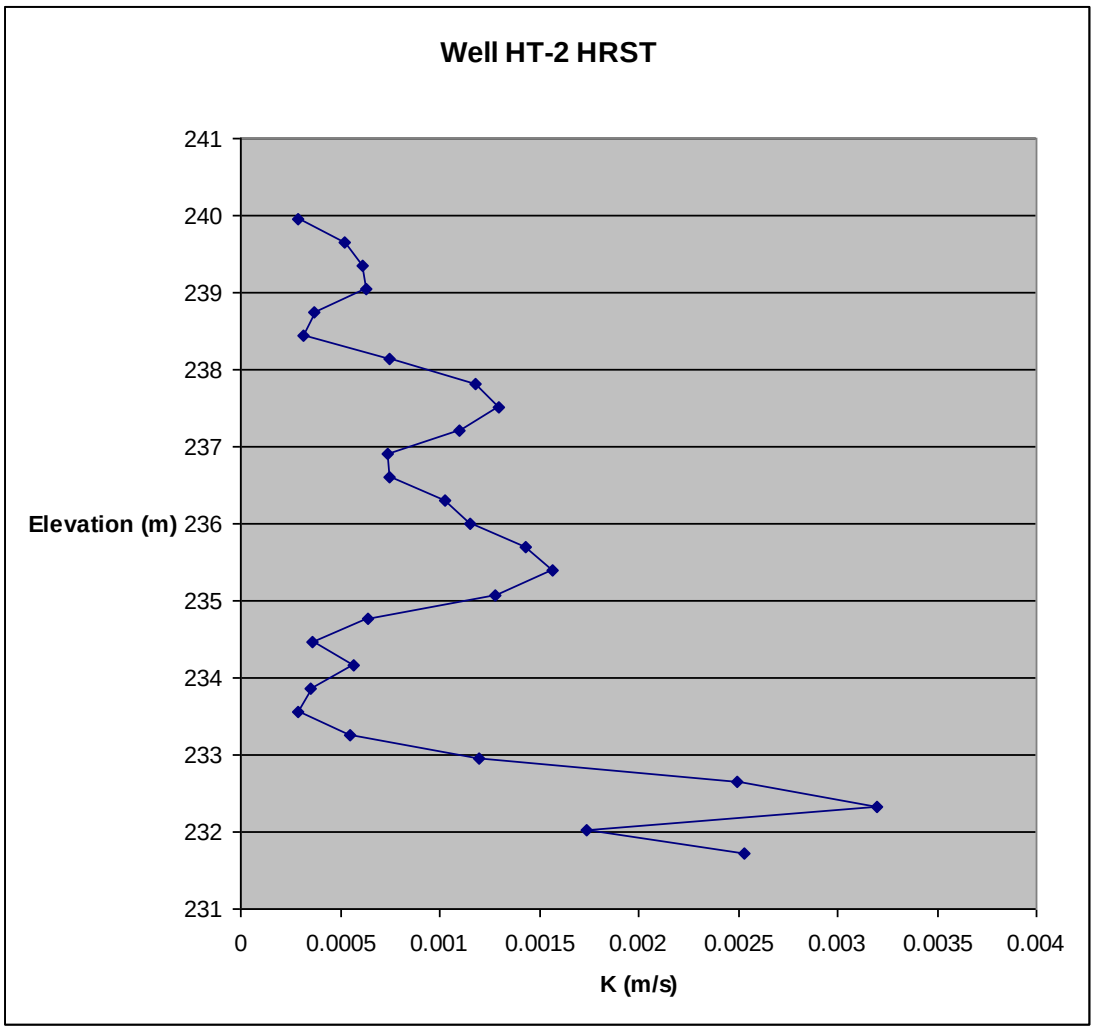

Figure 59: HRST results for well HT-2 (processed by Brett Engard).

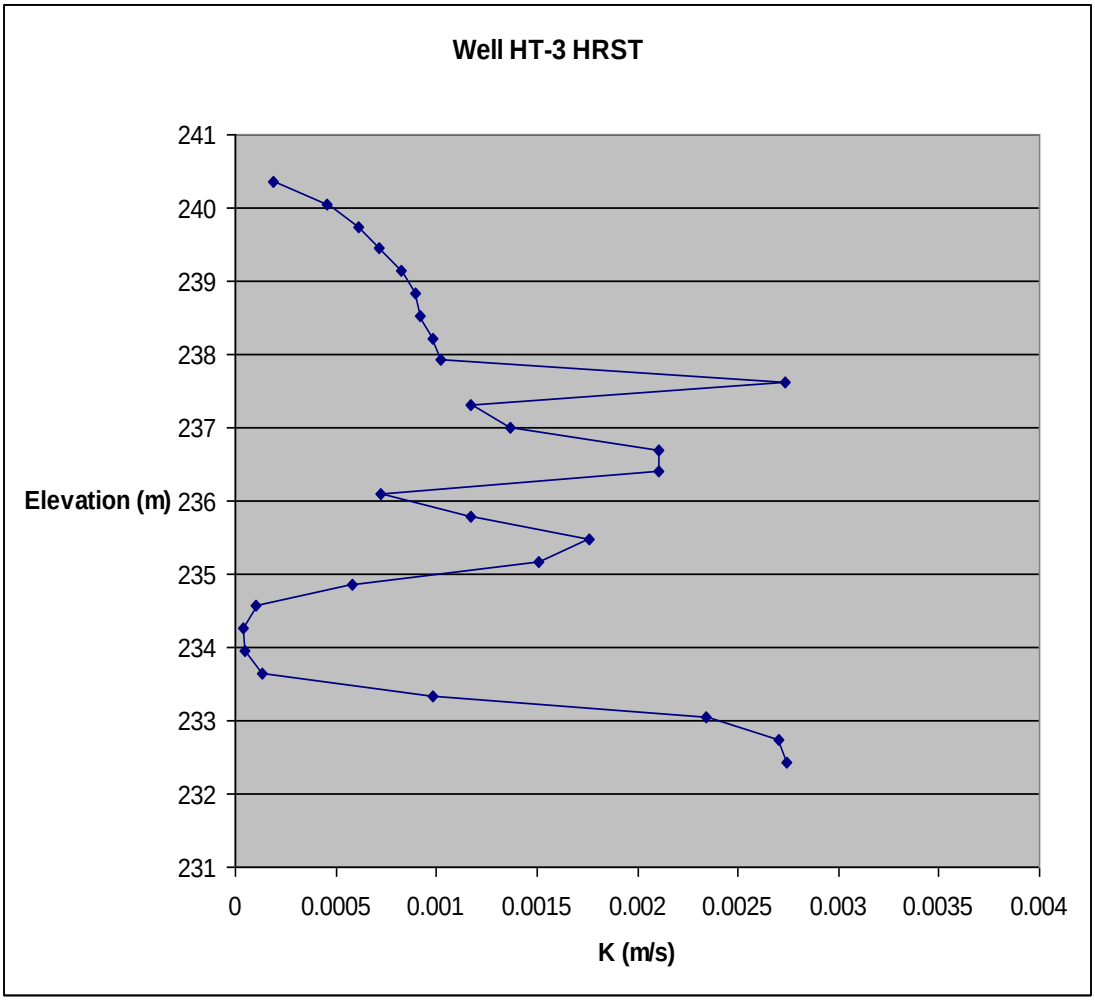

Figure 60: HRST results for well HT-3 (processed by Brett Engard).

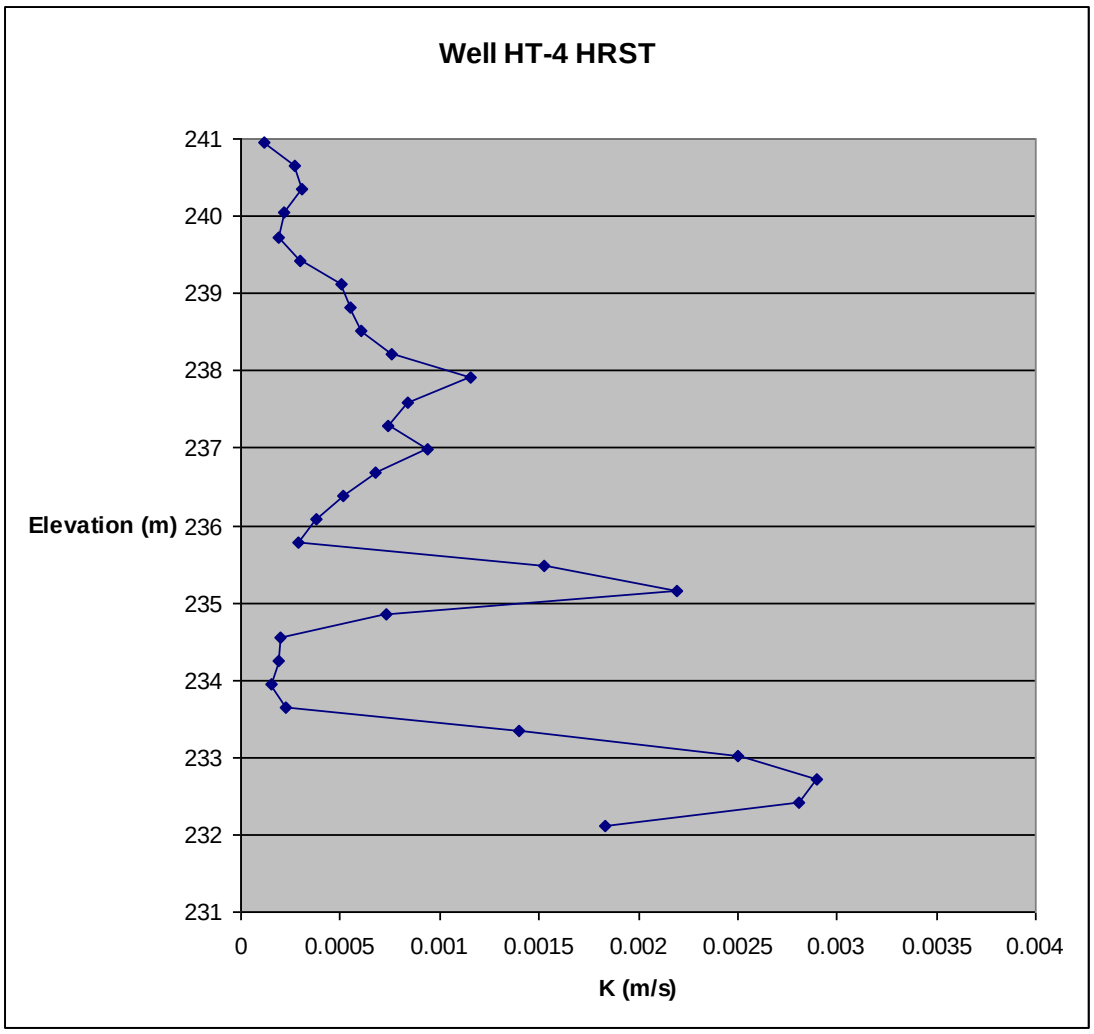

Figure 61: HRST results for well HT-4 (processed by Pema Deki).

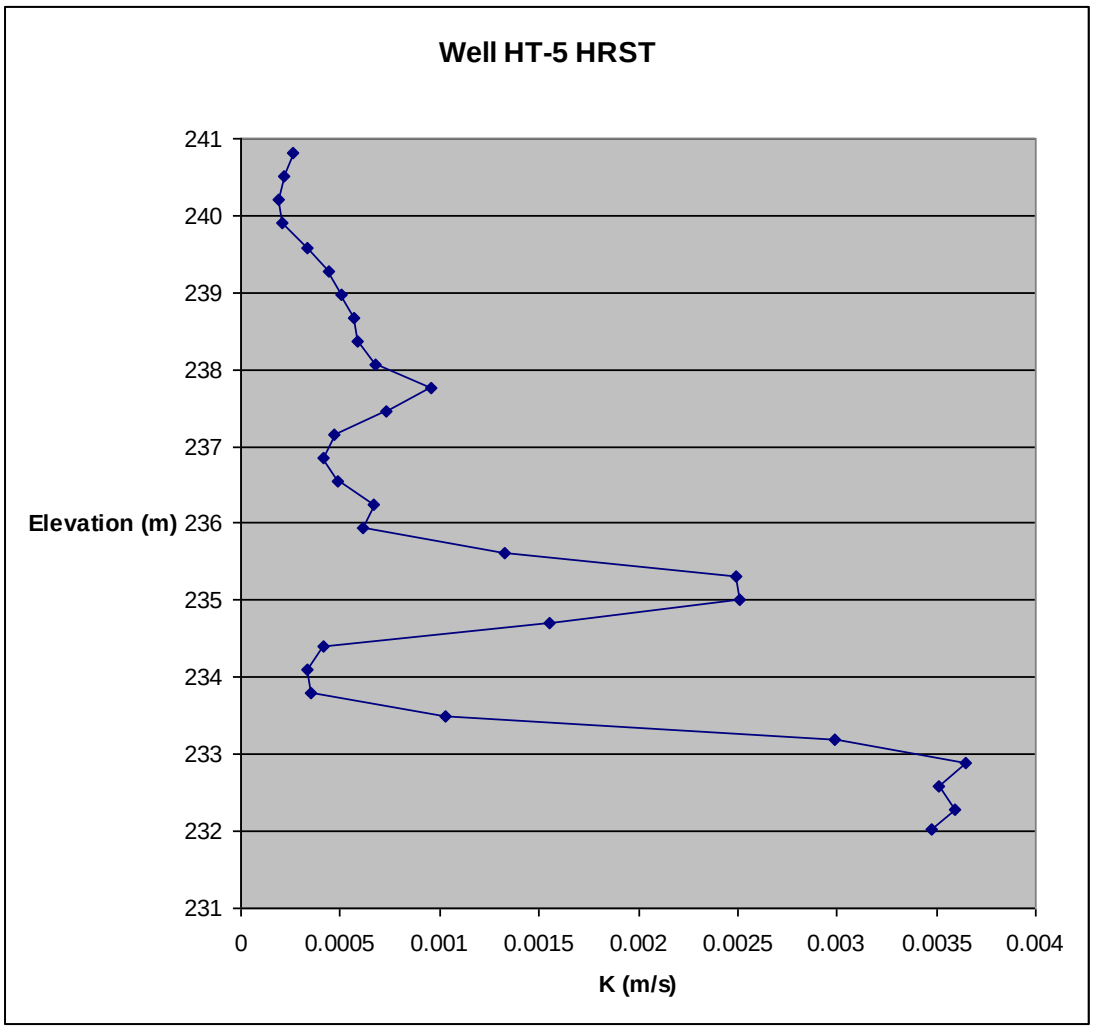

Figure 62: HRST results for well HT-5 (processed by Pema Deki).

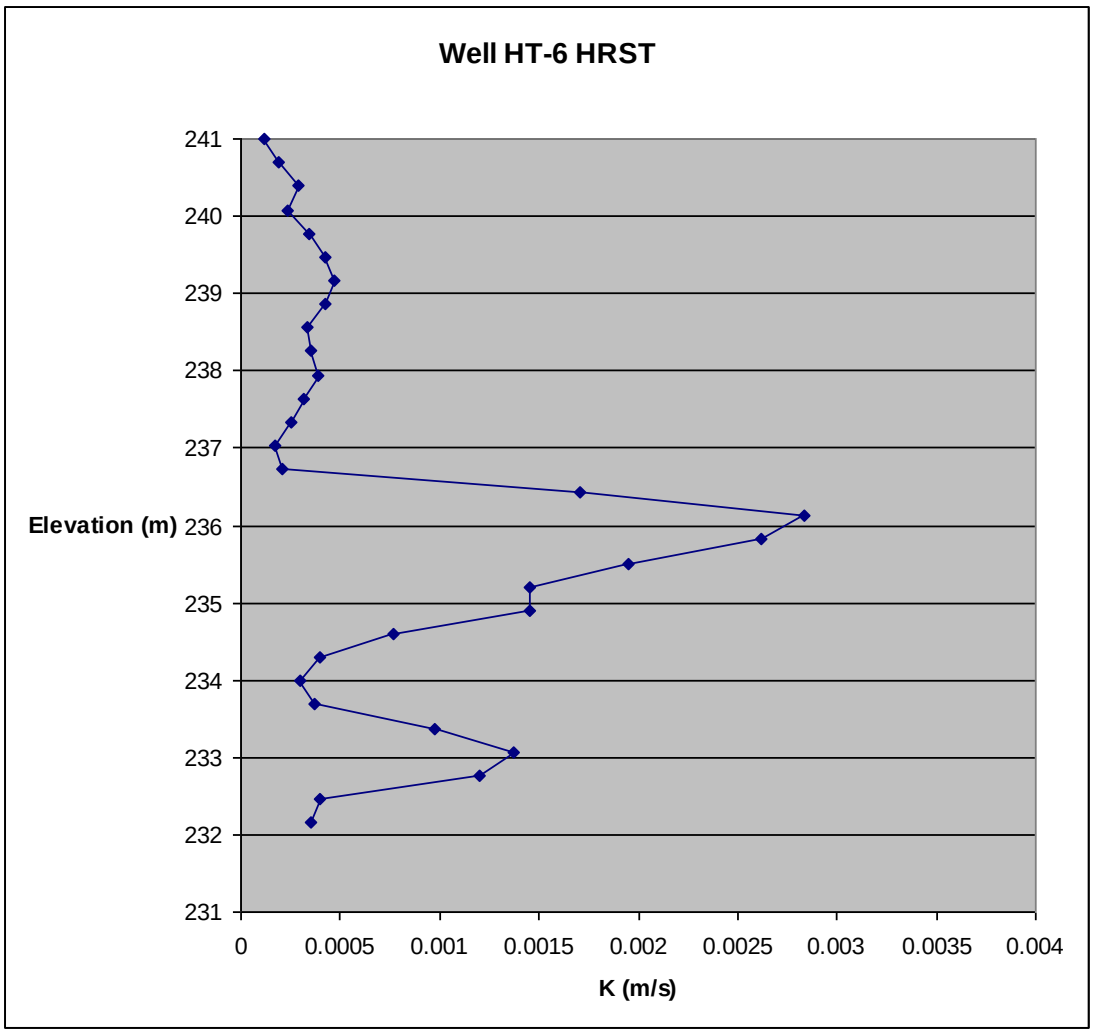

Figure 63: HRST results for well HT-6 (processed by Pema Deki).

APPENDIX B: Calculated vs. Experimental Zone Phase

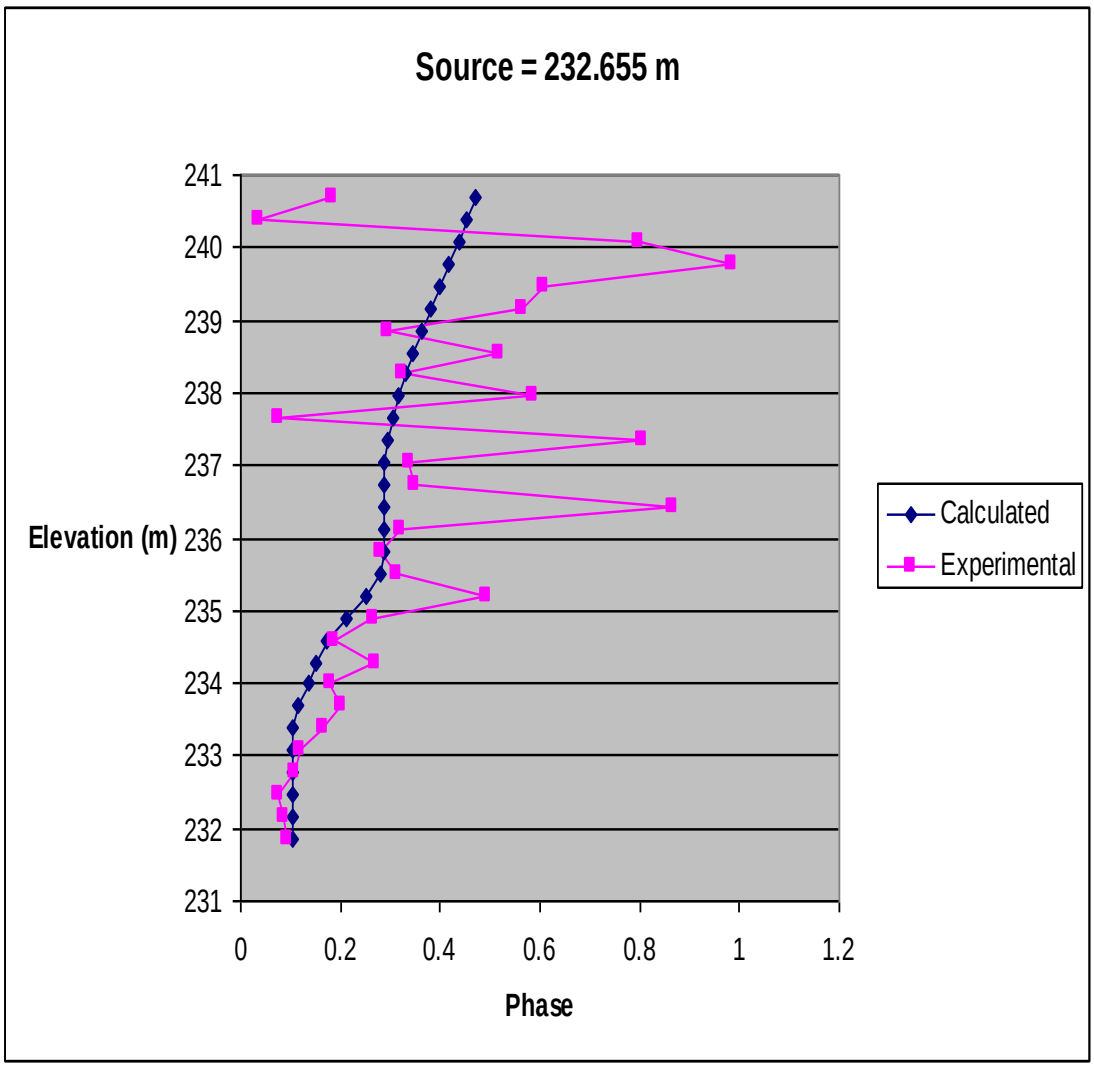

Figure 64: Experimental field phases and phases calculated using constrained SVD for a MOG from well HT-3 to well HT-1 with a source location of 232.655 m.

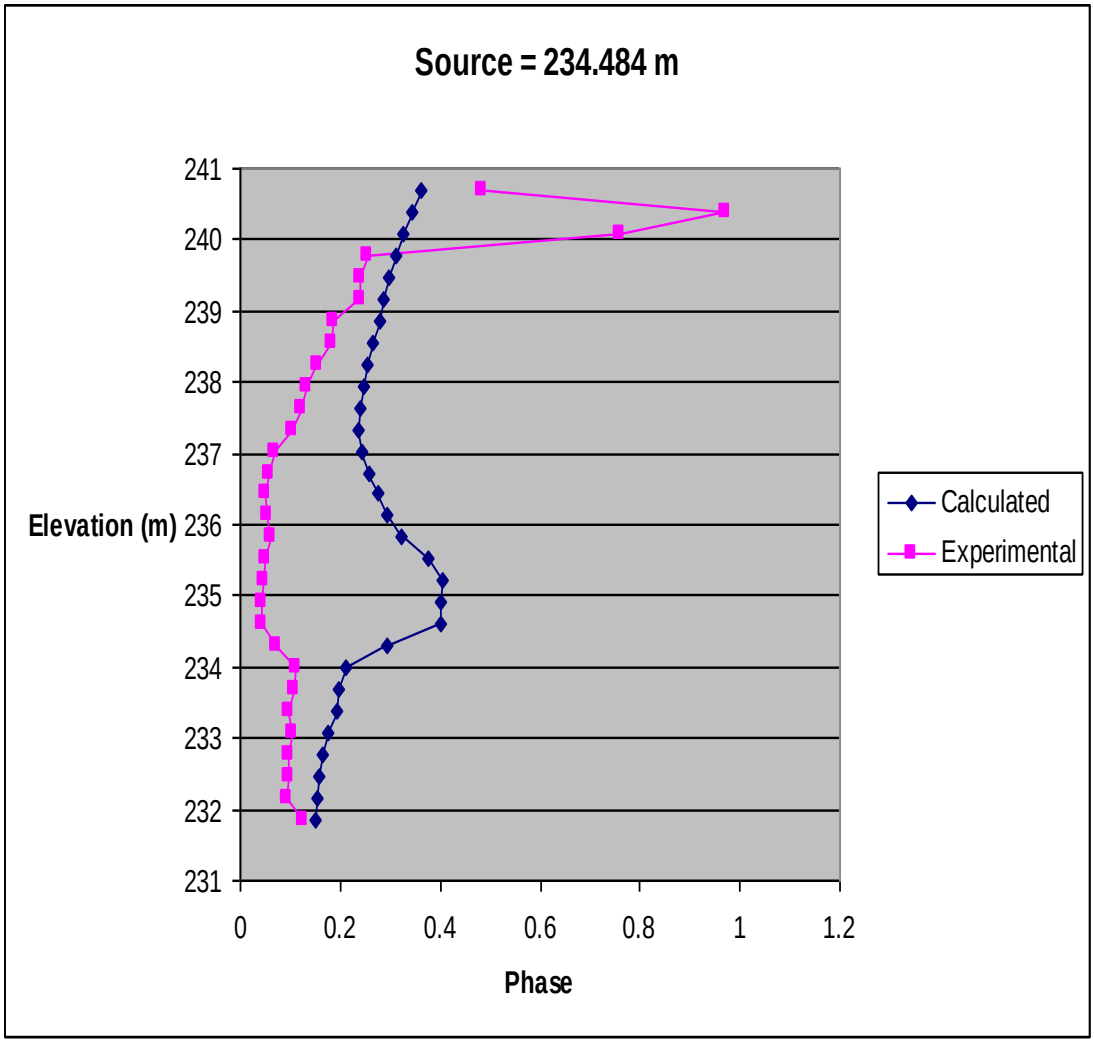

Figure 65: Experimental field phases and phases calculated using constrained SVD for a MOG from well HT-3 to well HT-1 with a source location of 234.484 m.

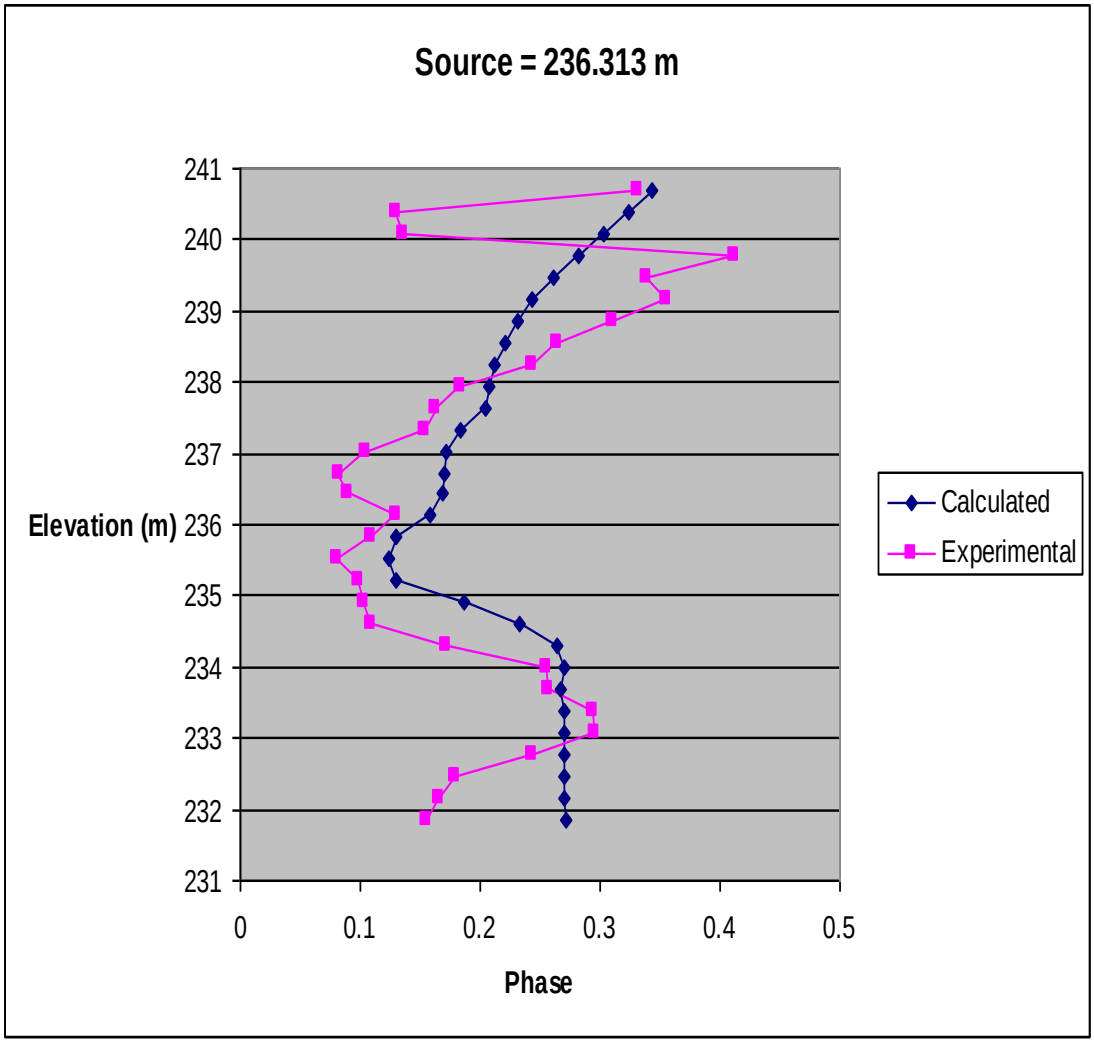

Figure 66: Experimental field phases and phases calculated using constrained SVD for a MOG from well HT-3 to well HT-1 with a source location of 236.313 m.

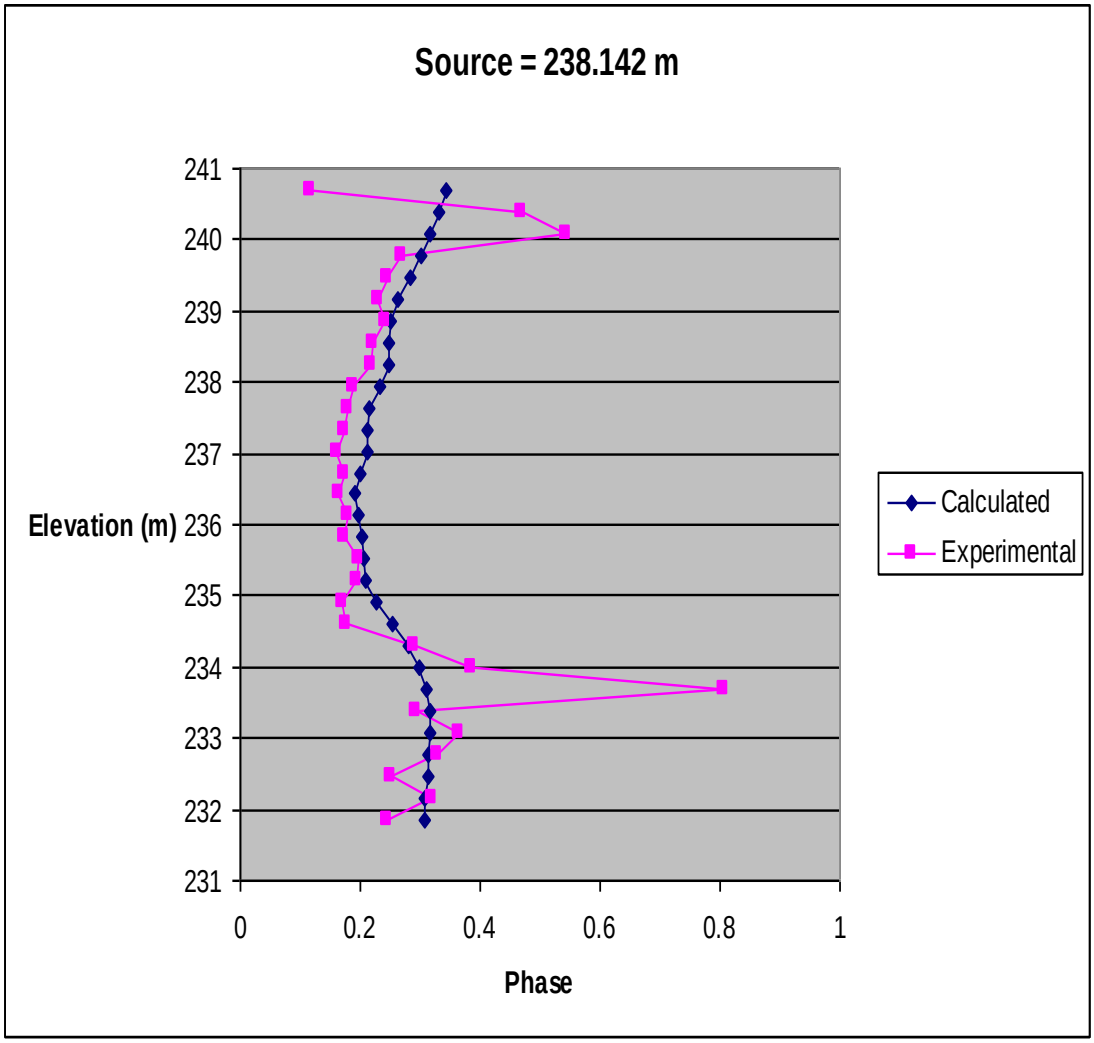

Figure 67: Experimental field phases and phases calculated using constrained SVD for a MOG from well HT-3 to well HT-1 with a source location of 238.142 m.

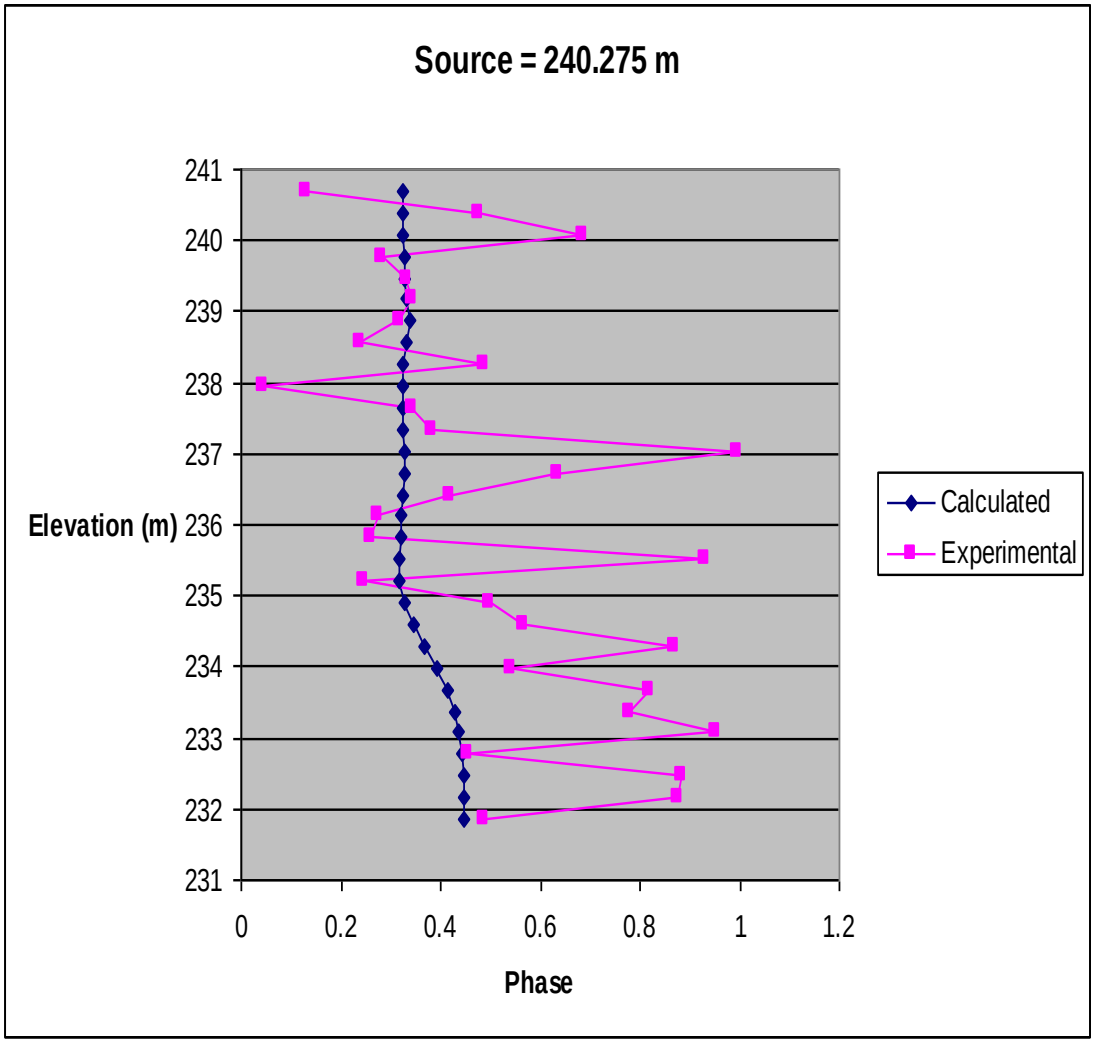

Figure 68: Experimental field phases and phases calculated using constrained SVD for a MOG from well HT-3 to well HT-1 with a source location of 240.275 m.

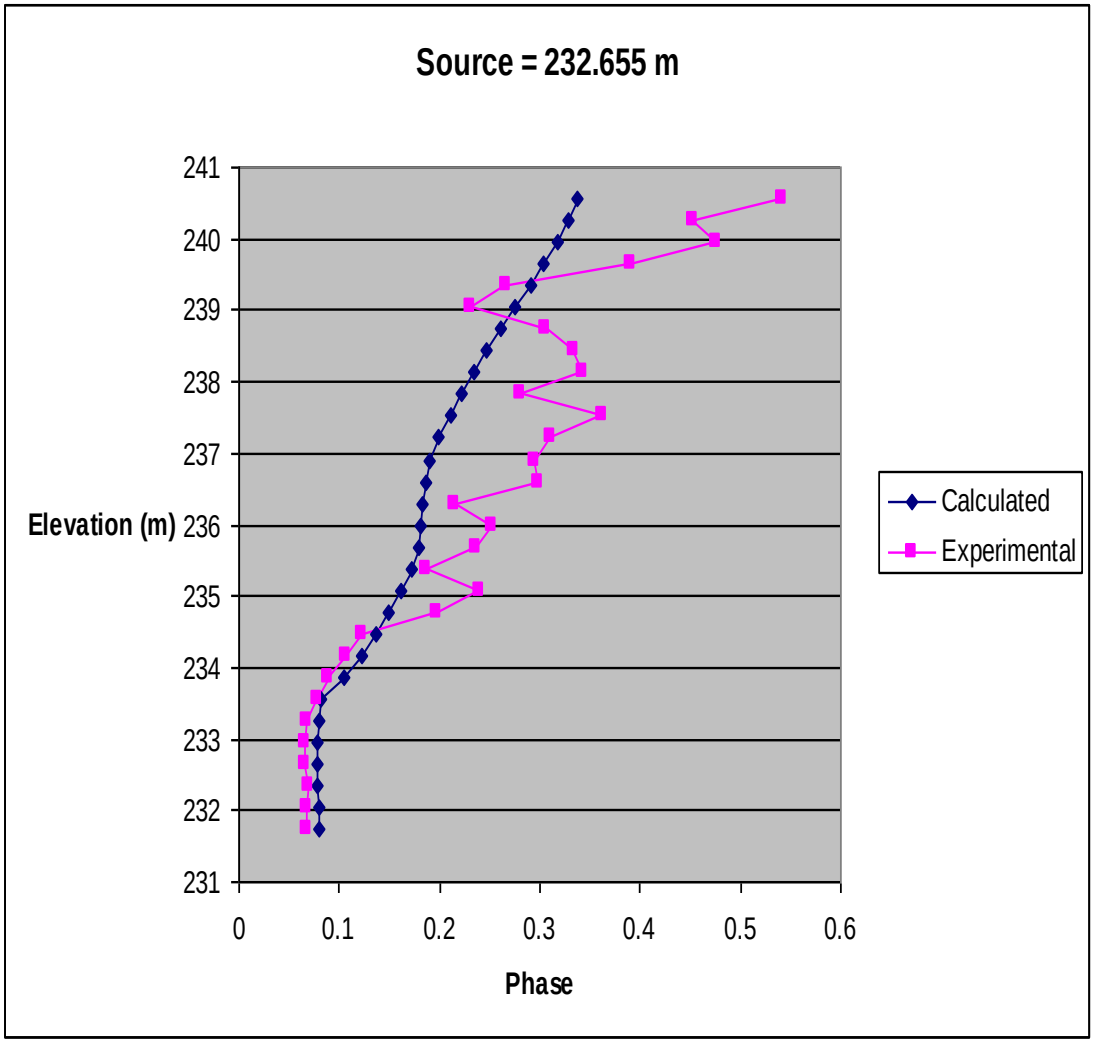

Figure 69: Experimental field phases and phases calculated using constrained SVD for a MOG from well HT-3 to well HT-2 with a source location of 232.655 m.

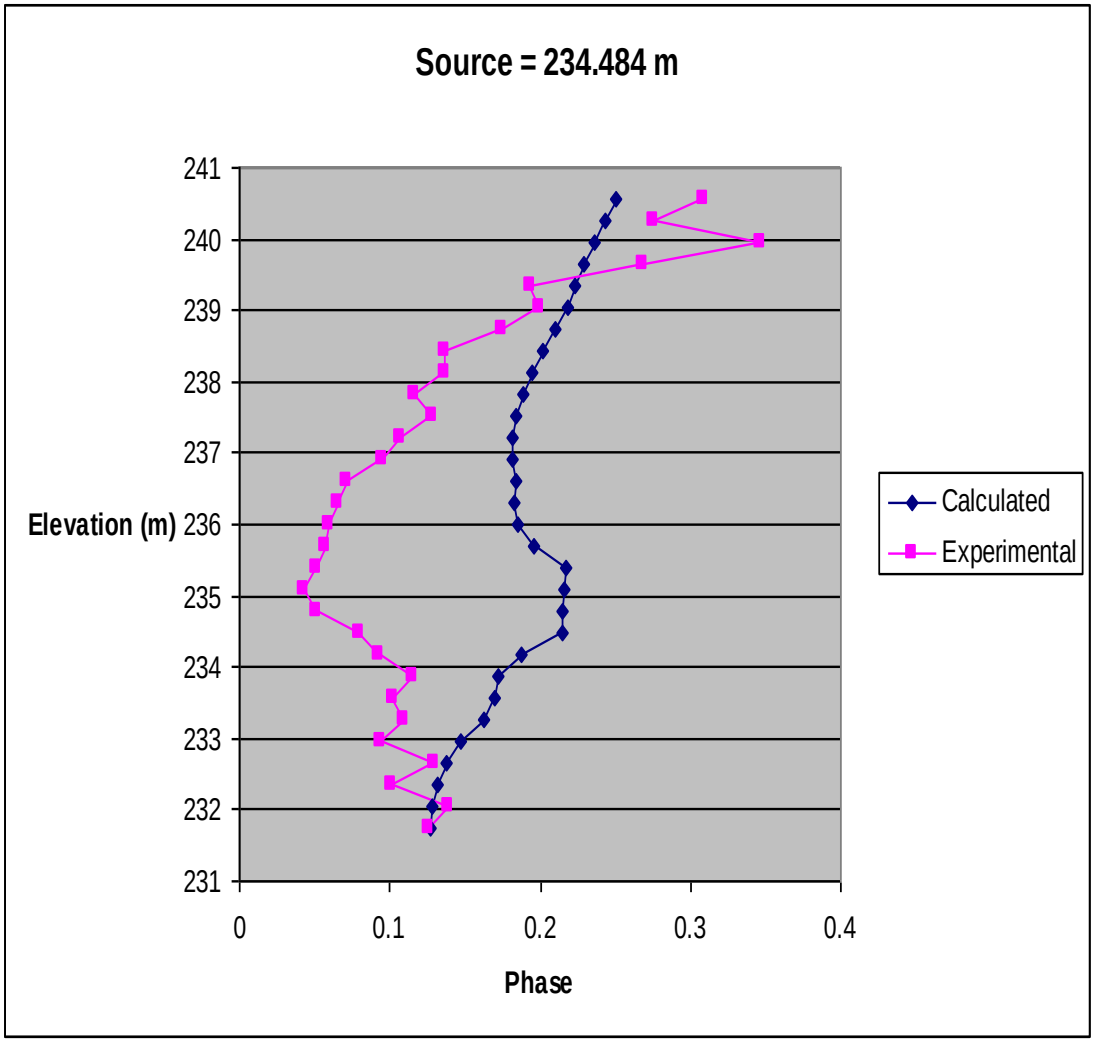

Figure 70: Experimental field phases and phases calculated using constrained SVD for a MOG from well HT-3 to well HT-2 with a source location of 234.484 m.

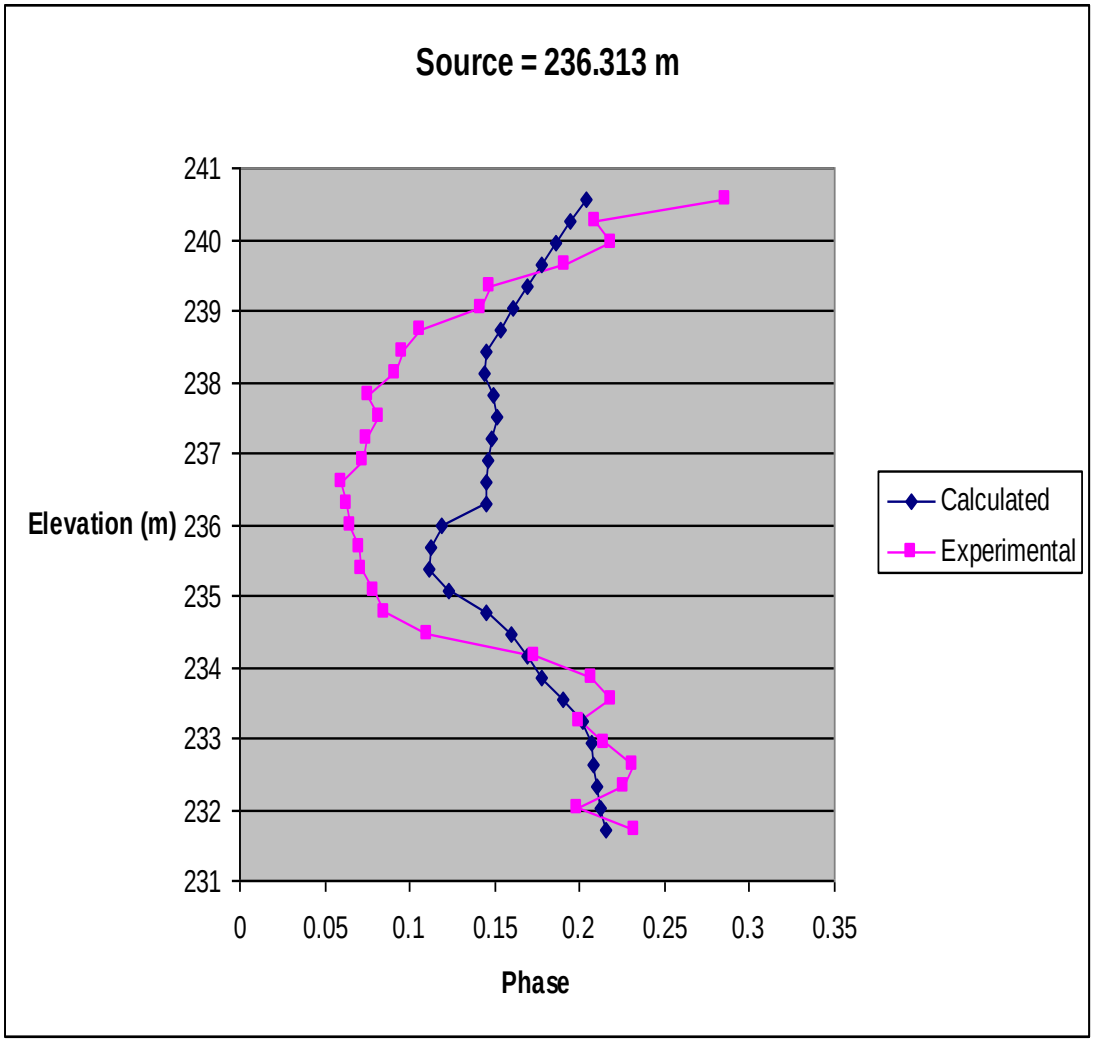

Figure 71: Experimental field phases and phases calculated using constrained SVD for a MOG from well HT-3 to well HT-2 with a source location of 236.313 m.

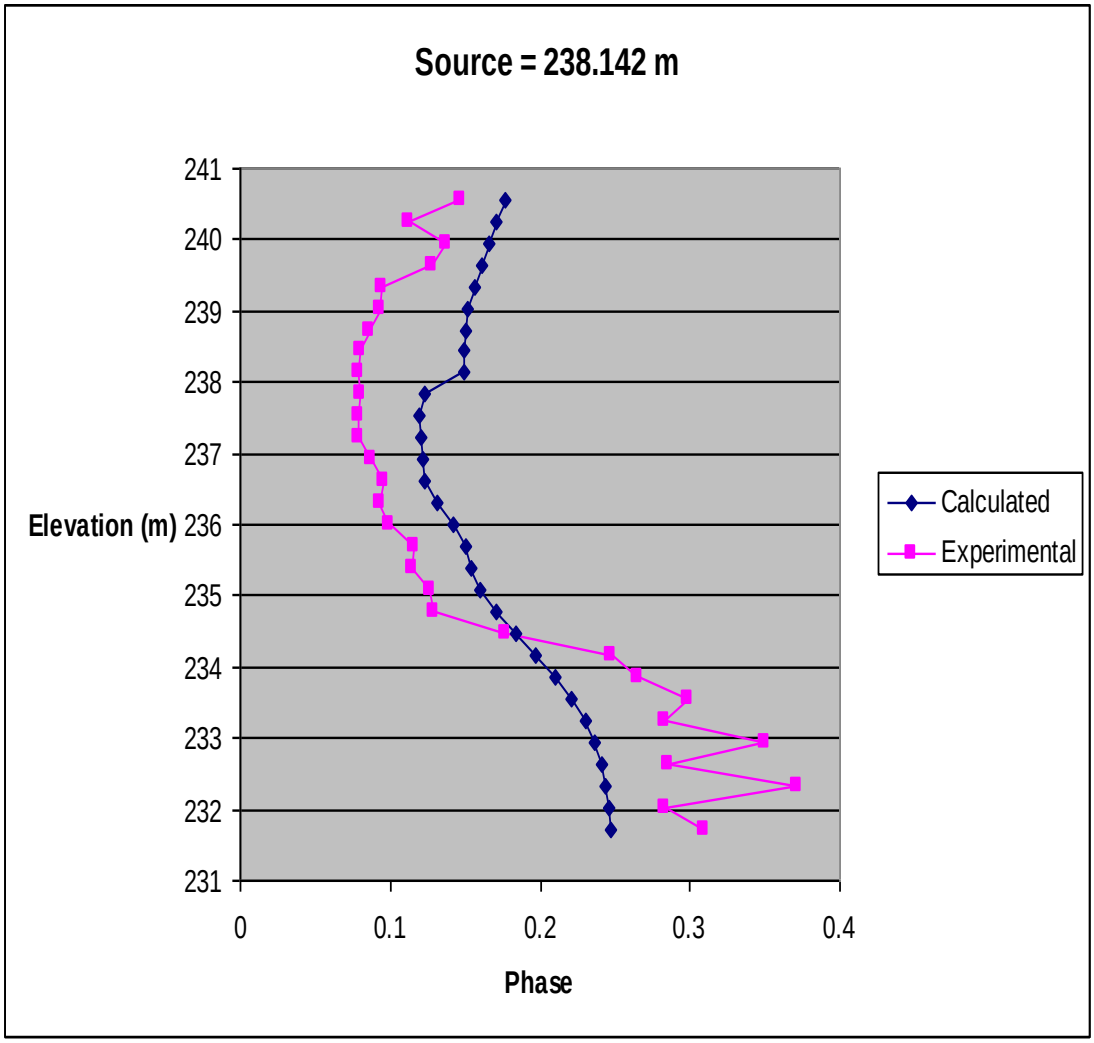

Figure 72: Experimental field phases and phases calculated using constrained SVD for a MOG from well HT-3 to well HT-2 with a source location of 238.142 m.

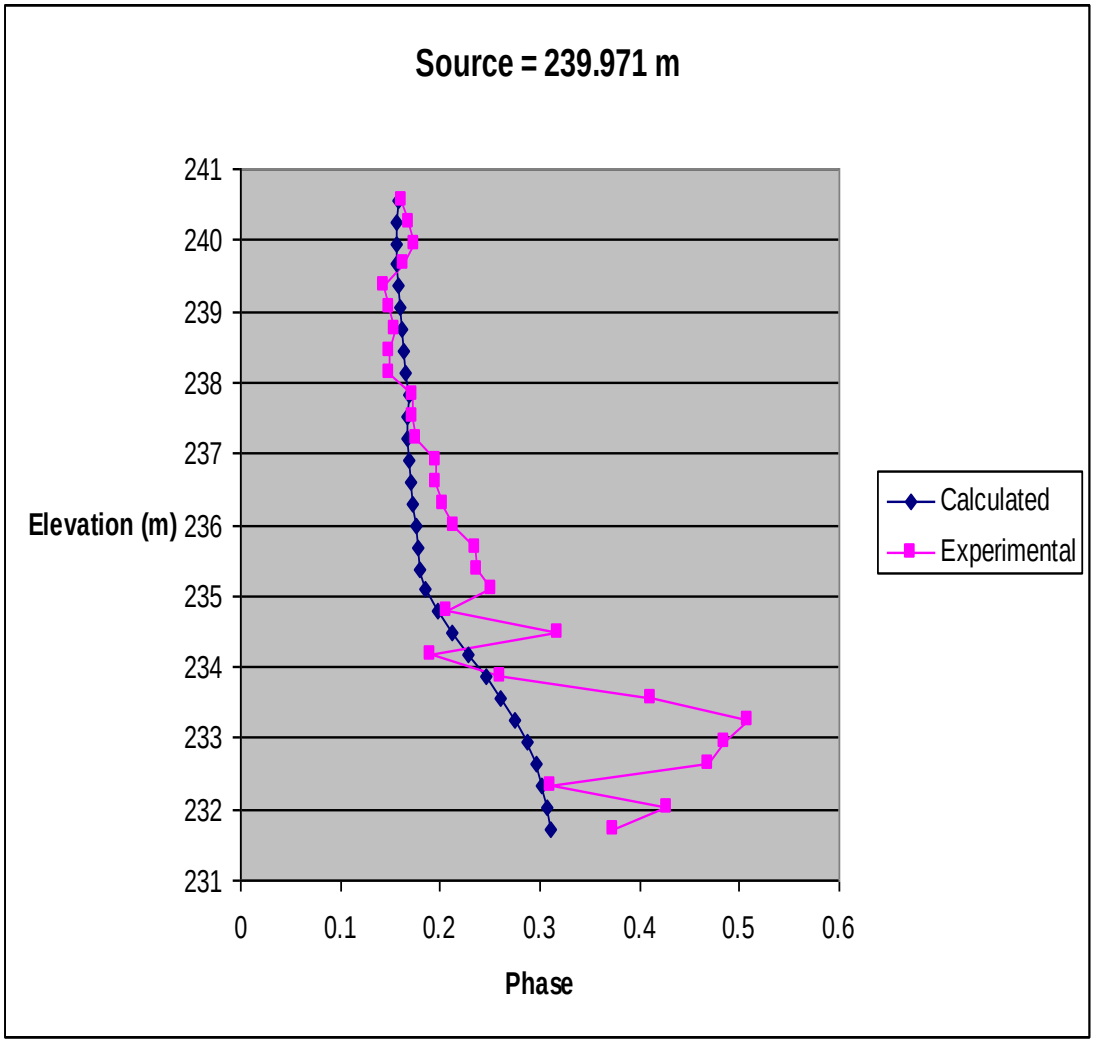

Figure 73: Experimental field phases and phases calculated using constrained SVD for a MOG from well HT-3 to well HT-2 with a source location of 239.971 m.

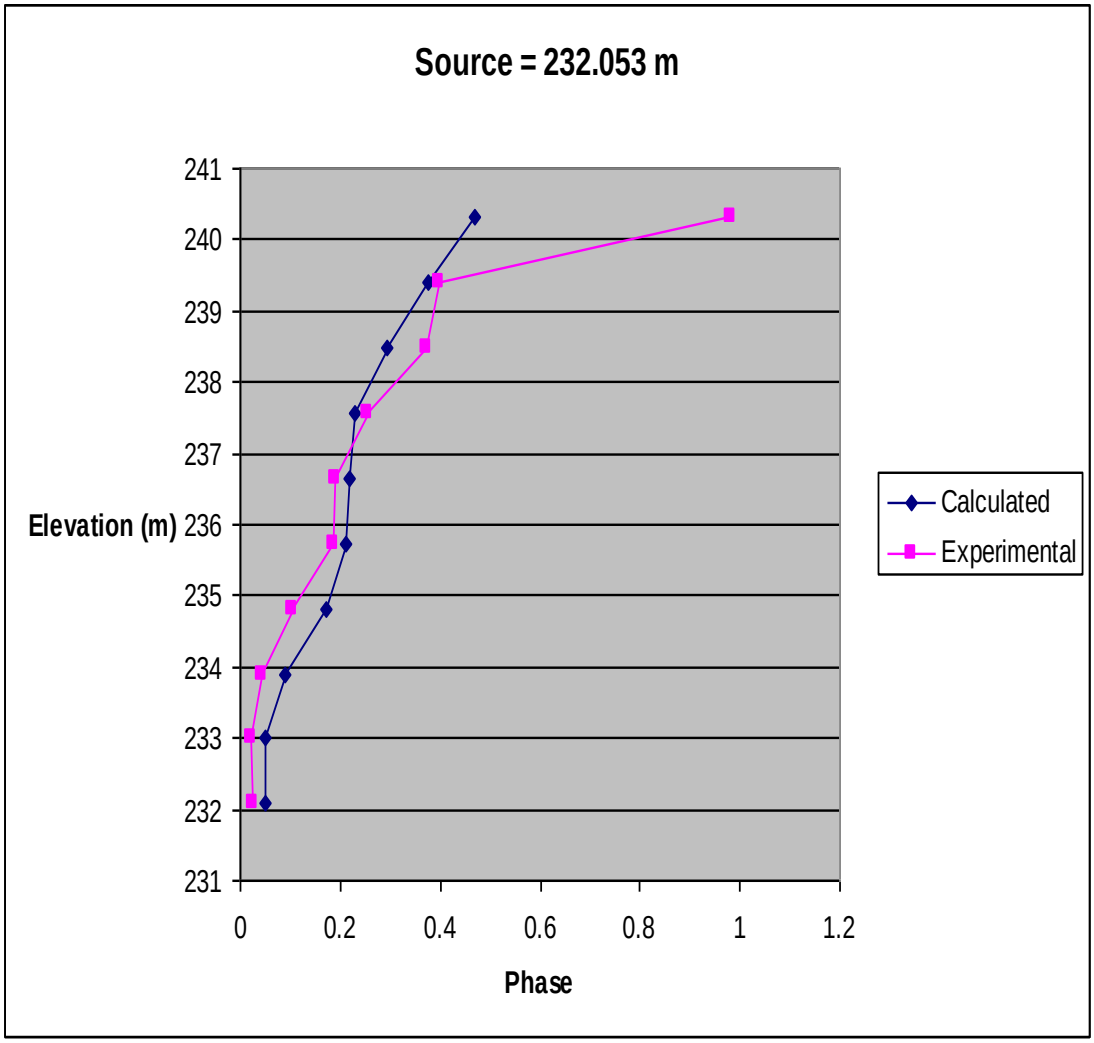

Figure 74: Experimental field phases and phases calculated using constrained SVD for a MOG from well HT-4 to well HT-3 with a source location of 232.053 m.

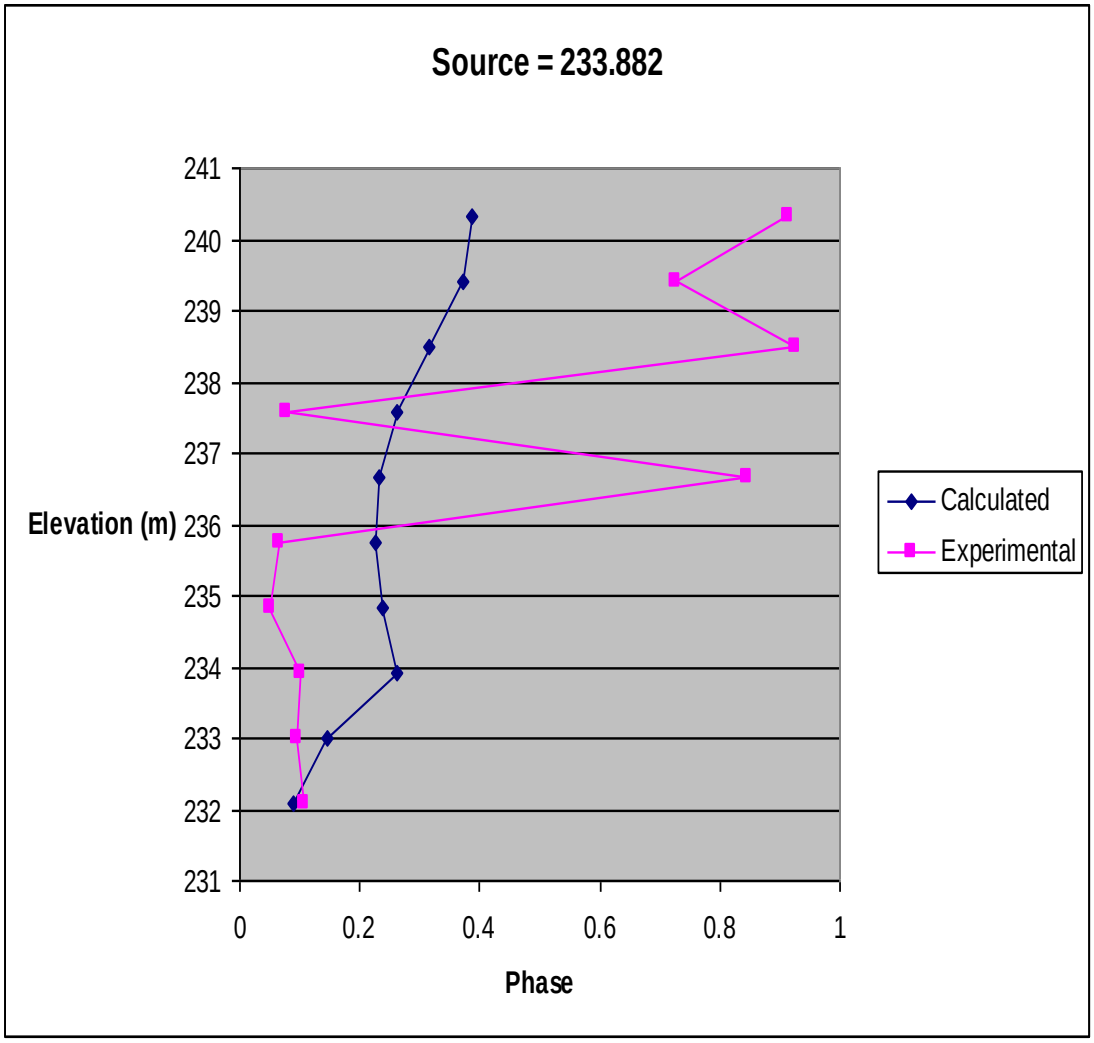

Figure 75: Experimental field phases and phases calculated using constrained SVD for a MOG from well HT-4 to well HT-3 with a source location of 233.882 m.

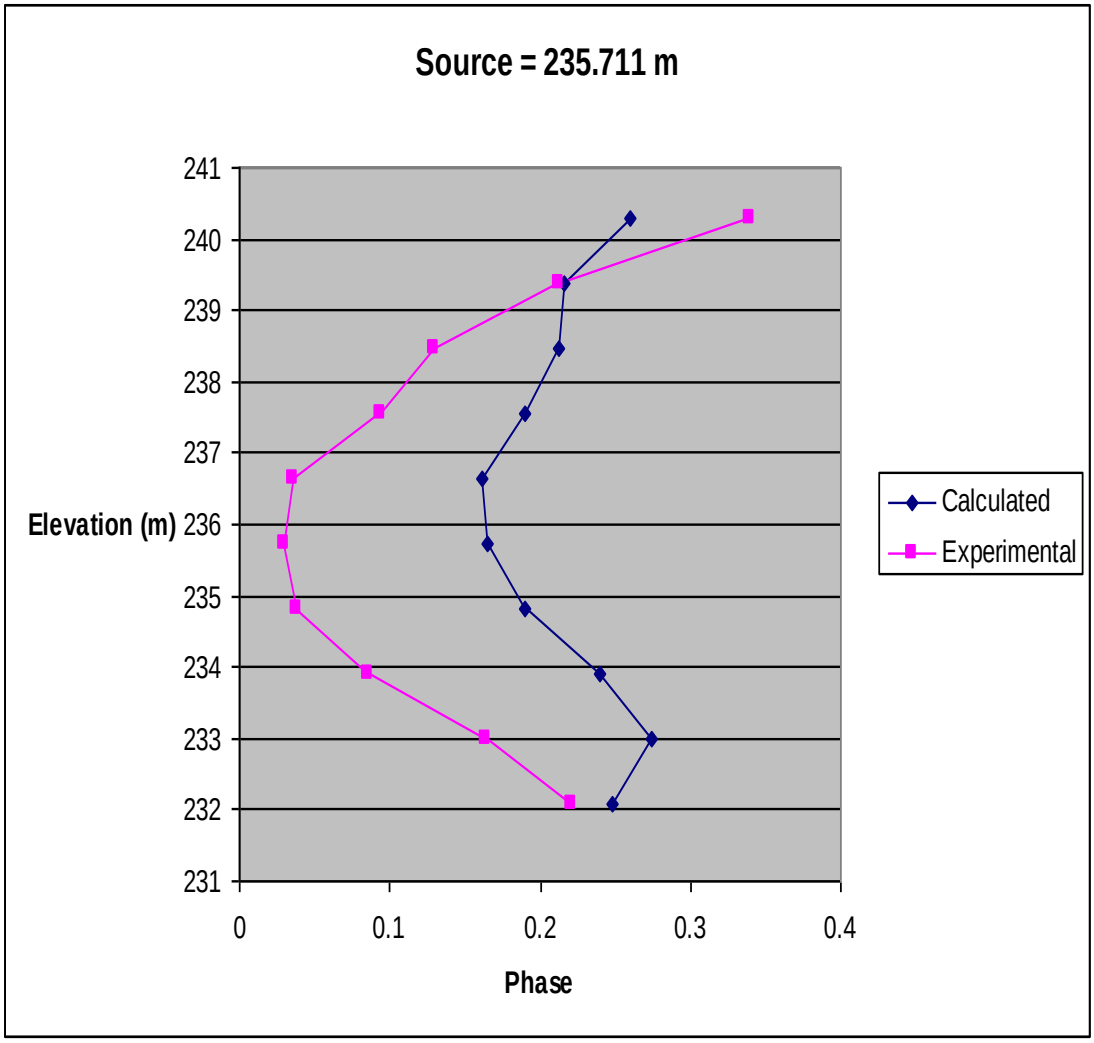

Figure 76: Experimental field phases and phases calculated using constrained SVD for a MOG from well HT-4 to well HT-3 with a source location of 235.711 m.

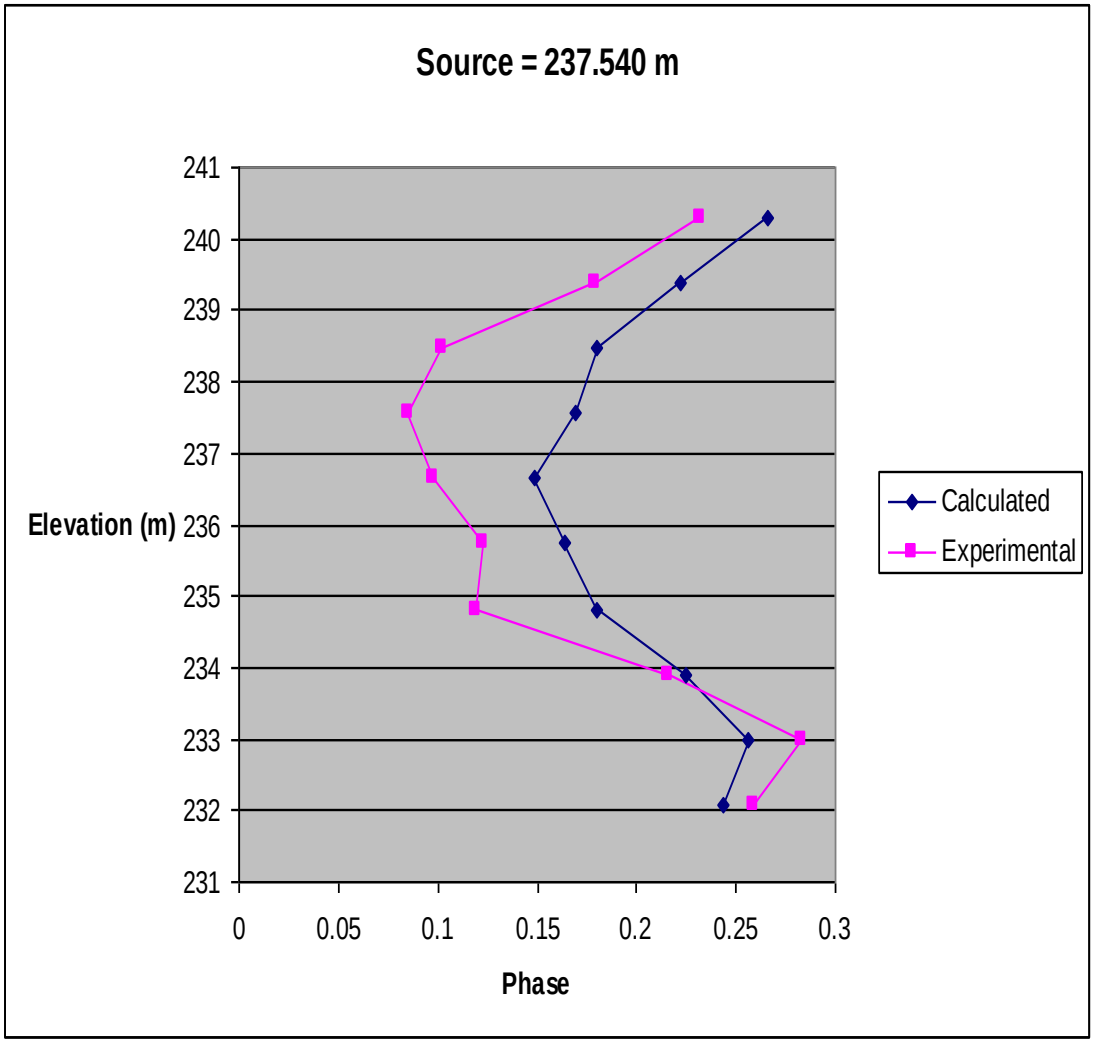

Figure 77: Experimental field phases and phases calculated using constrained SVD for a MOG from well HT-4 to well HT-3 with a source location of 237.540 m.

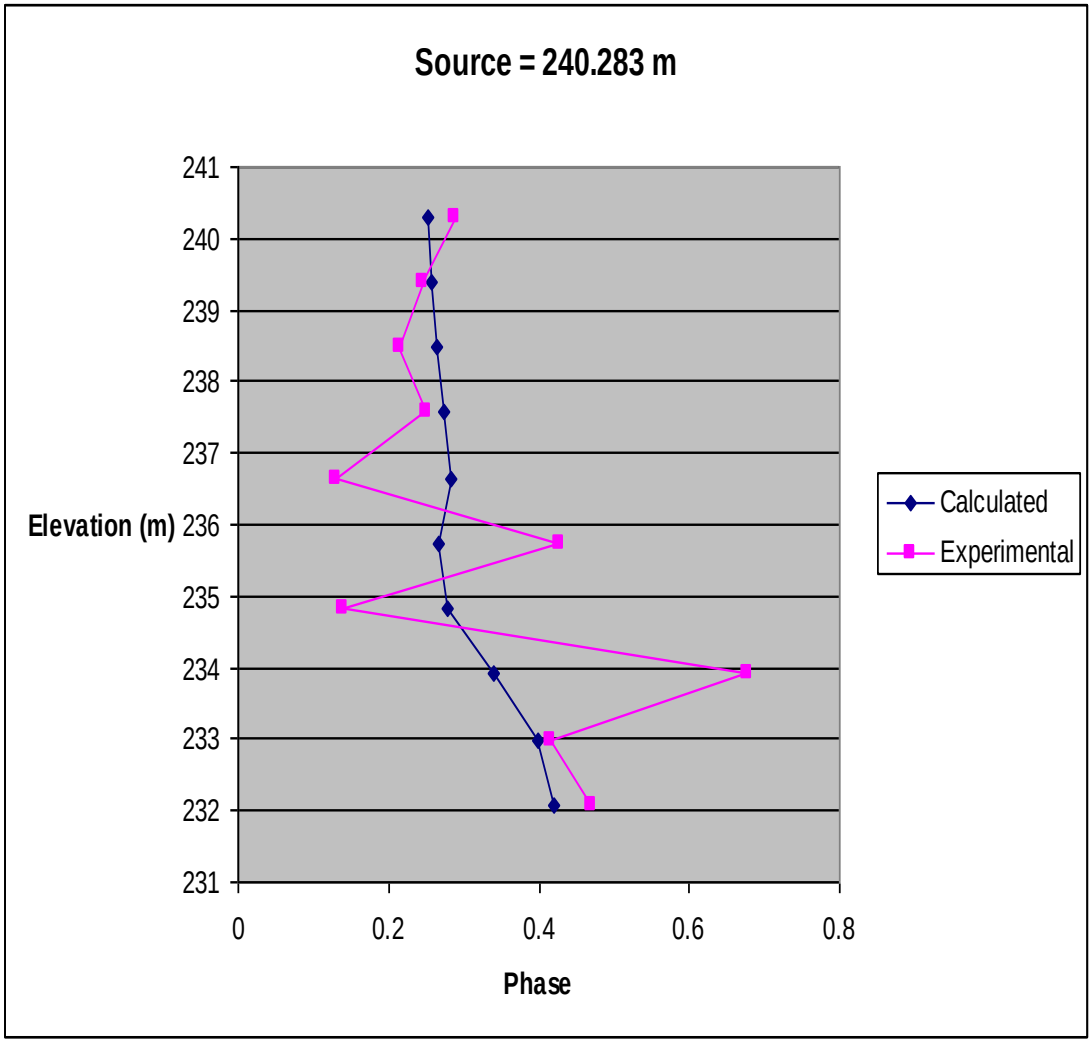

Figure 78: Experimental field phases and phases calculated using constrained SVD for a MOG from well HT-4 to well HT-3 with a source location of 240.283 m.

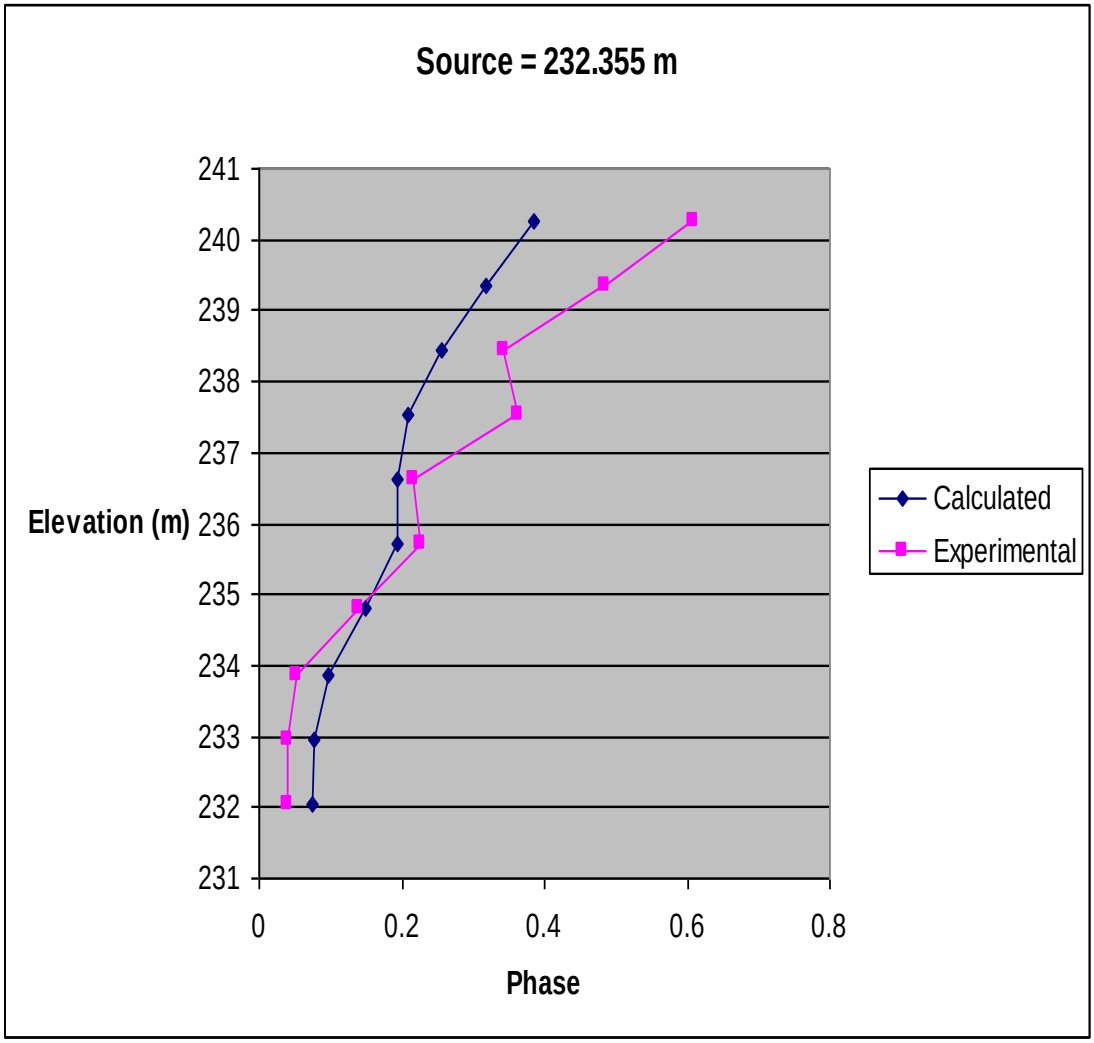

Figure 79: Experimental field phases and phases calculated using constrained SVD for a MOG from well HT-5 to well HT-3 with a source location of 232.355 m.

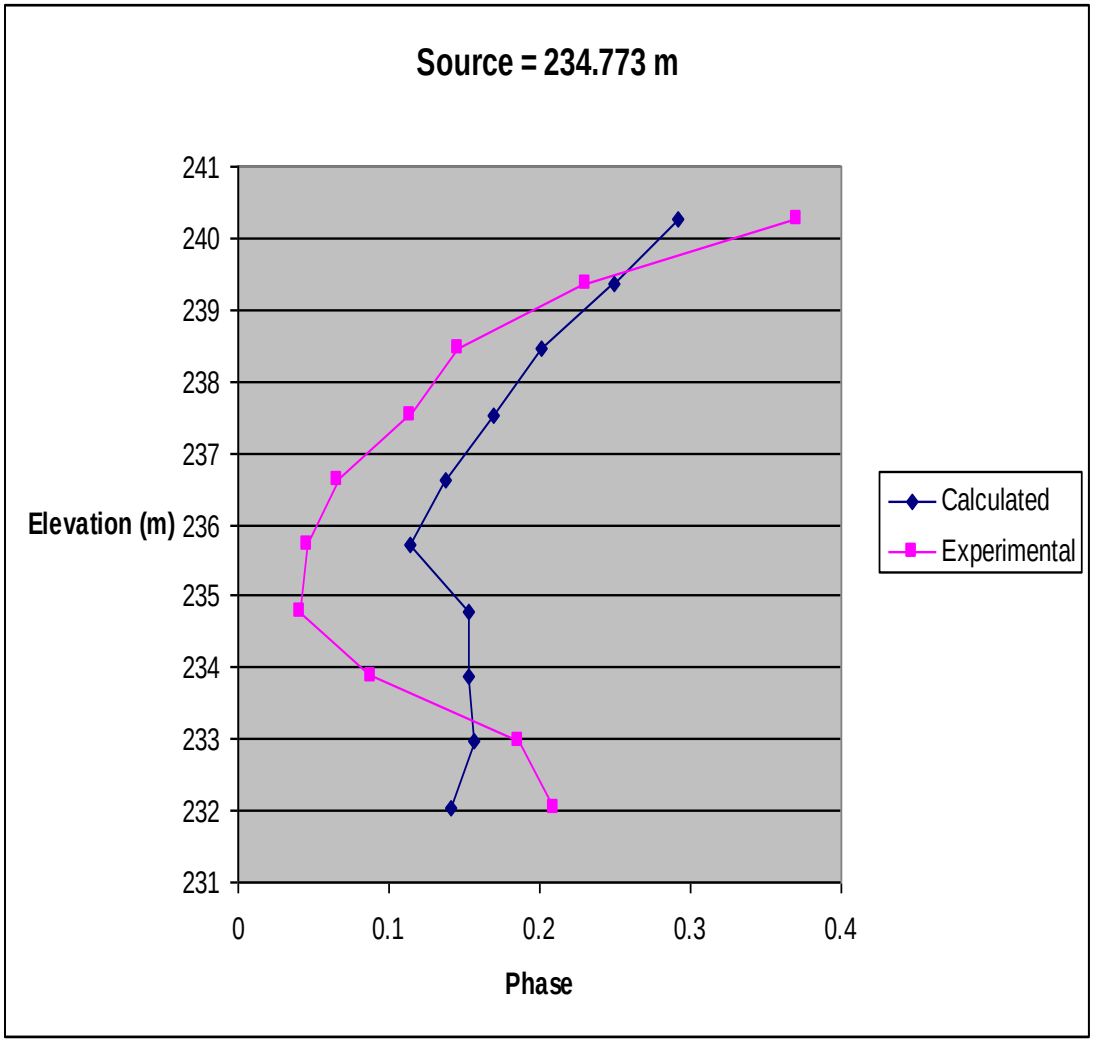

Figure 80: Experimental field phases and phases calculated using constrained SVD for a MOG from well HT-5 to well HT-3 with a source location of 234.773 m.

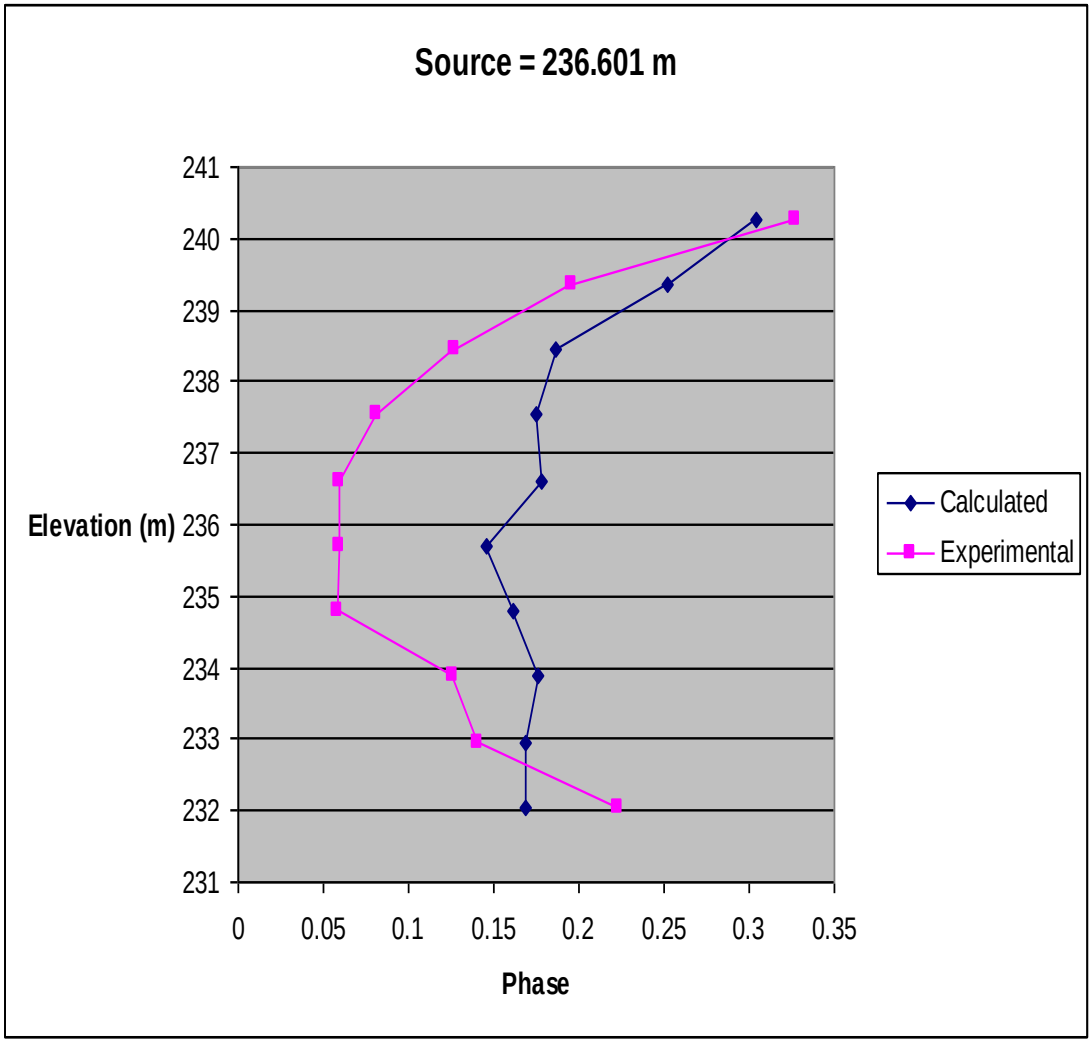

Figure 81: Experimental field phases and phases calculated using constrained SVD for a MOG from well HT-5 to well HT-3 with a source location of 236.601 m.

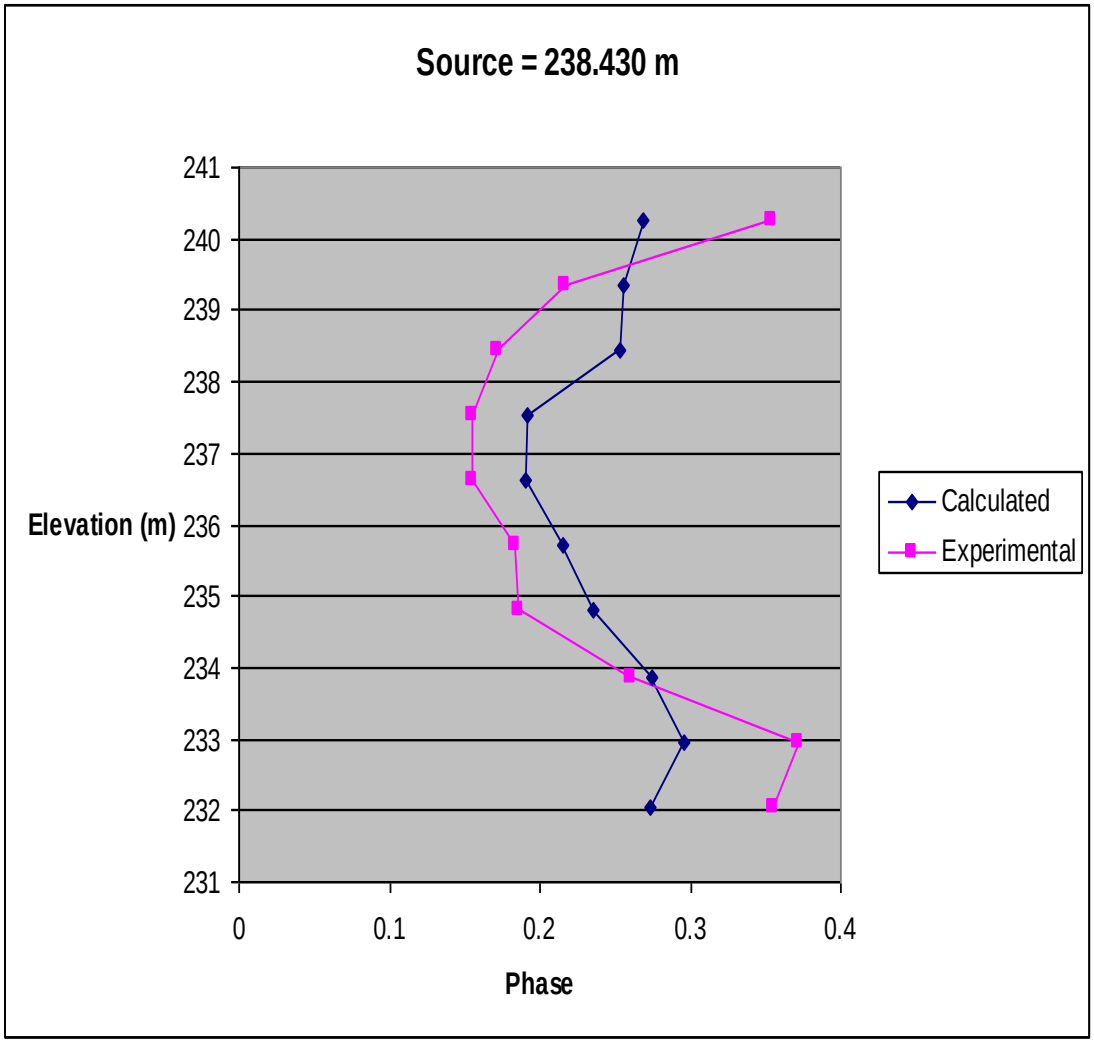

Figure 82: Experimental field phases and phases calculated using constrained SVD for a MOG from well HT-5 to well HT-3 with a source location of 238.430 m.

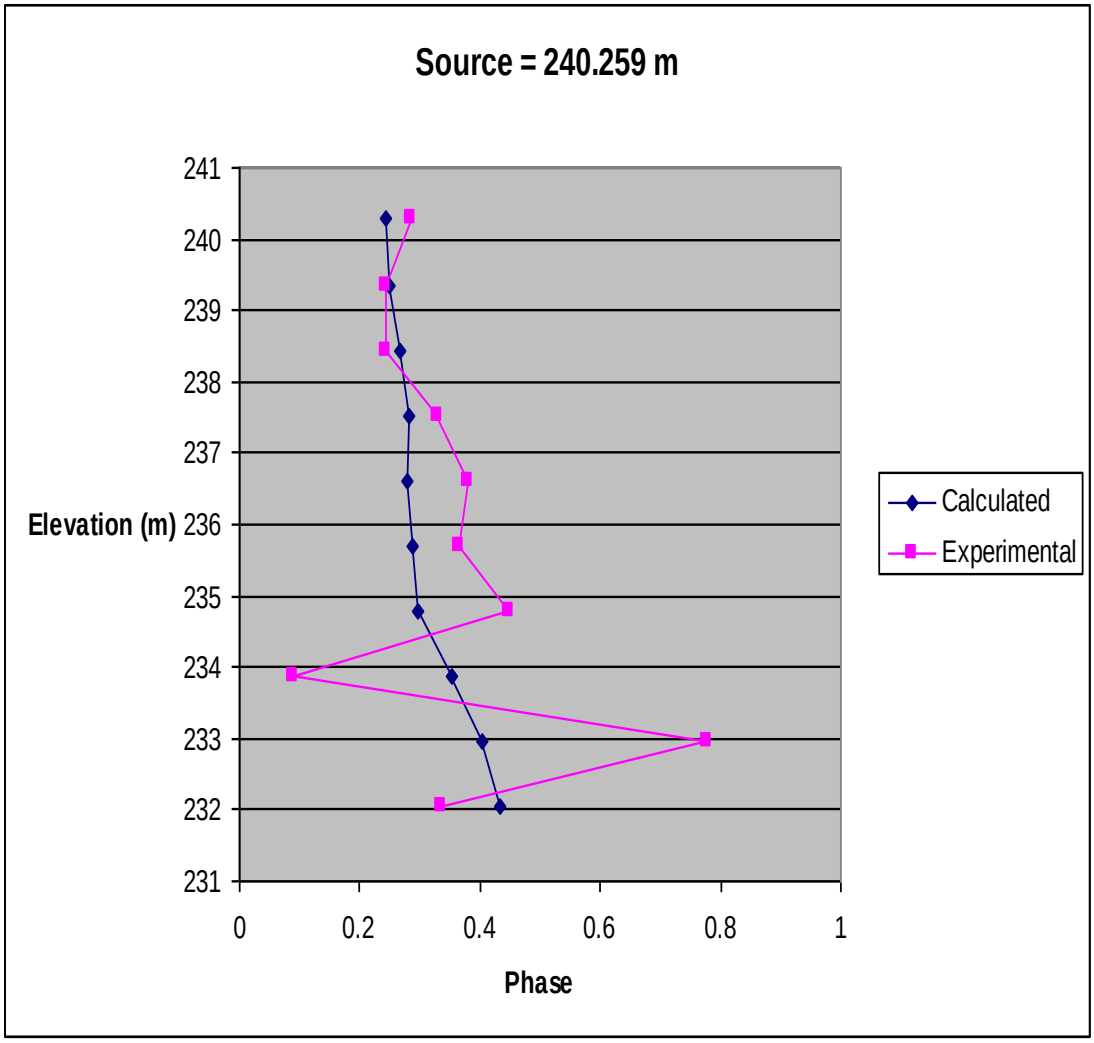

Figure 83: Experimental field phases and phases calculated using constrained SVD for a MOG from well HT-5 to well HT-3 with a source location of 240.259 m.

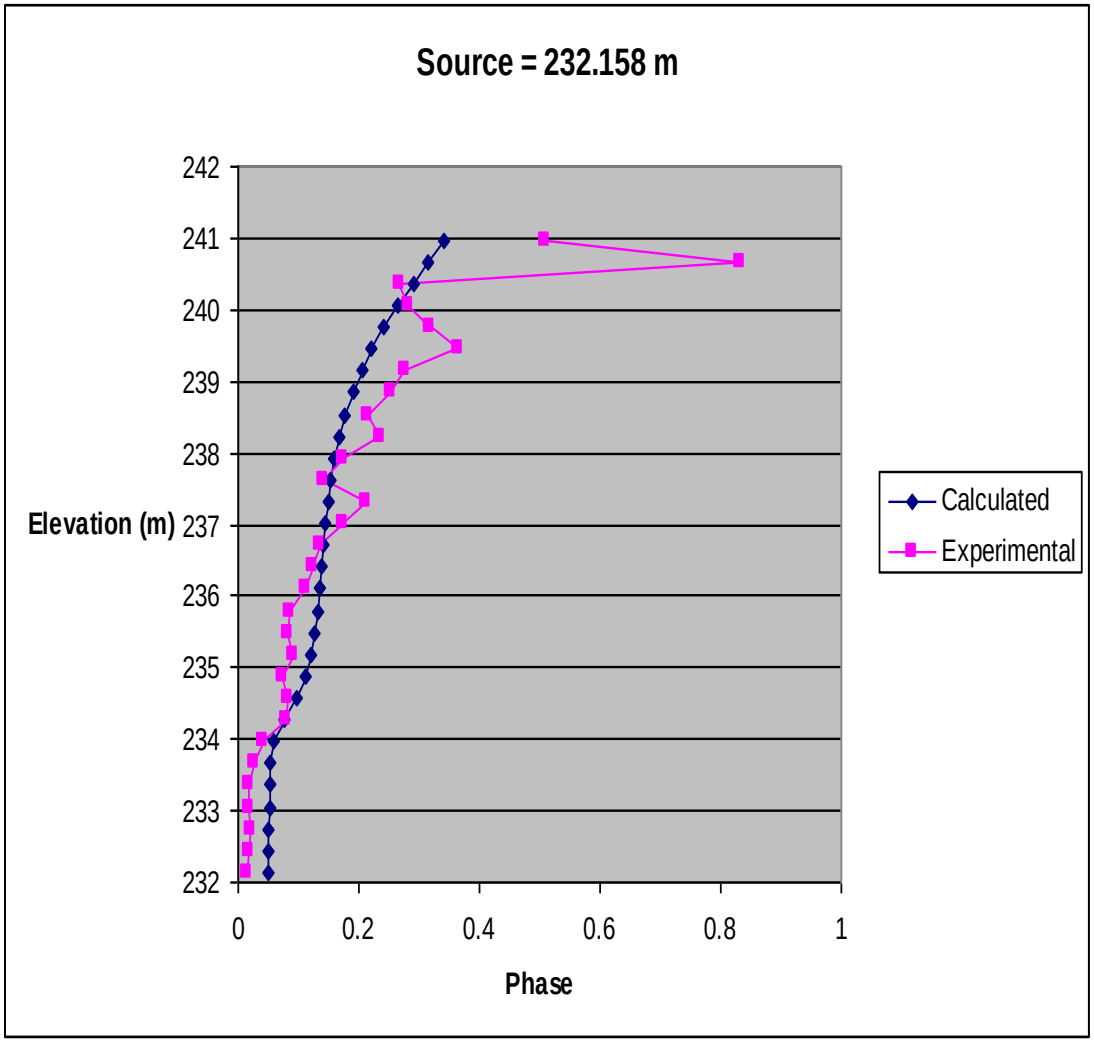

Figure 84: Experimental field phases and phases calculated using constrained SVD for a MOG from well HT-6 to well HT-3 with a source location of 232.158 m.

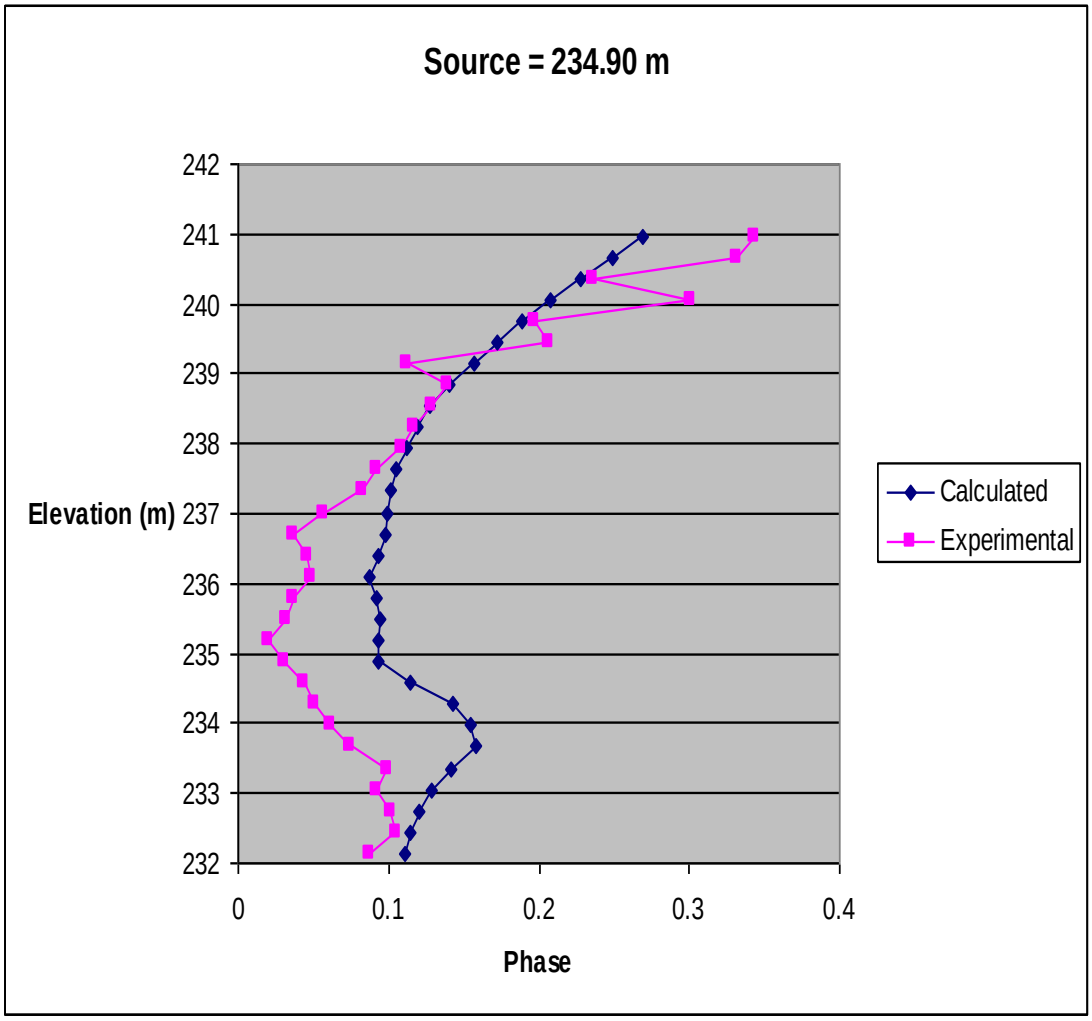

Figure 85: Experimental field phases and phases calculated using constrained SVD for a MOG from well HT-6 to well HT-3 with a source location of 234.90 m.

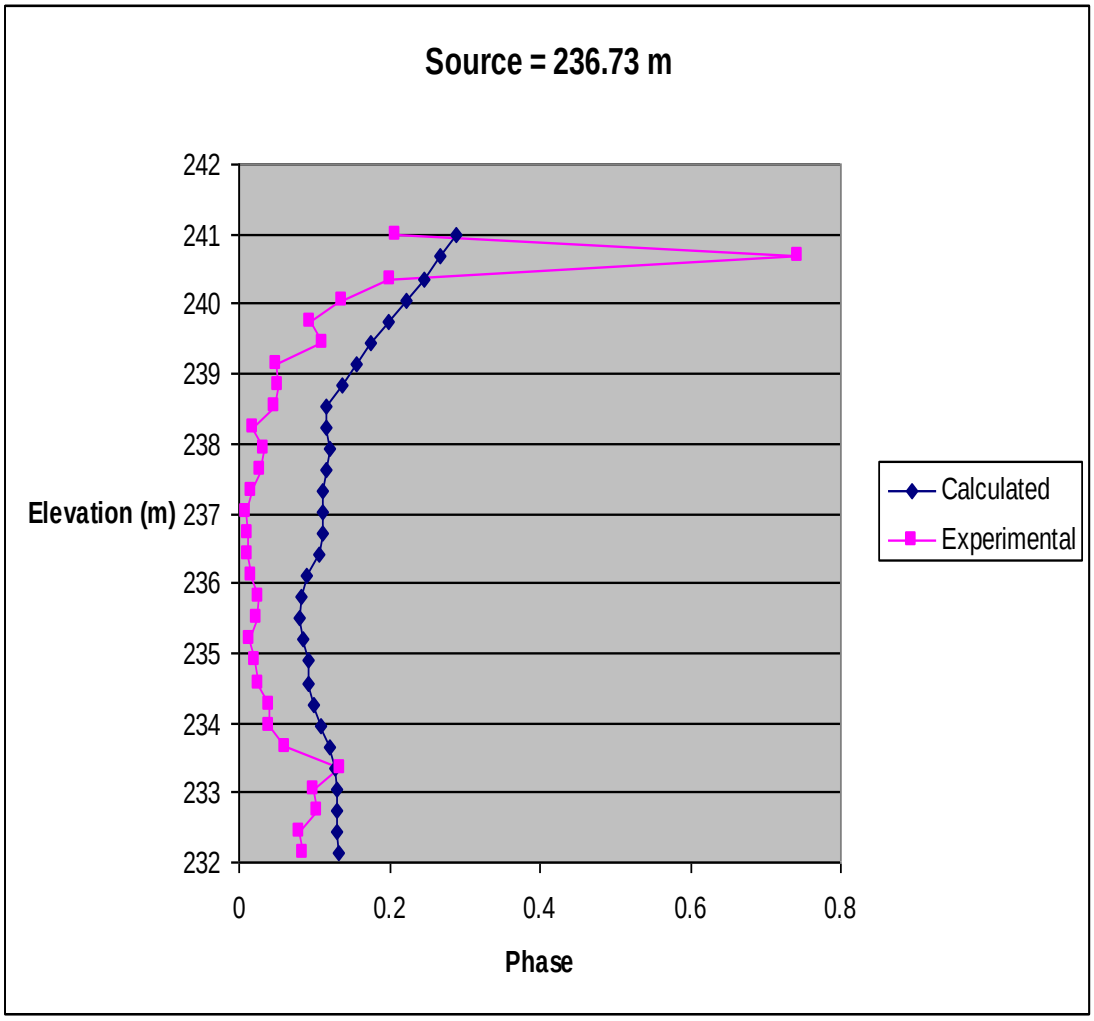

Figure 86: Experimental field phases and phases calculated using constrained SVD for a MOG from well HT-6 to well HT-3 with a source location of 236.73 m.

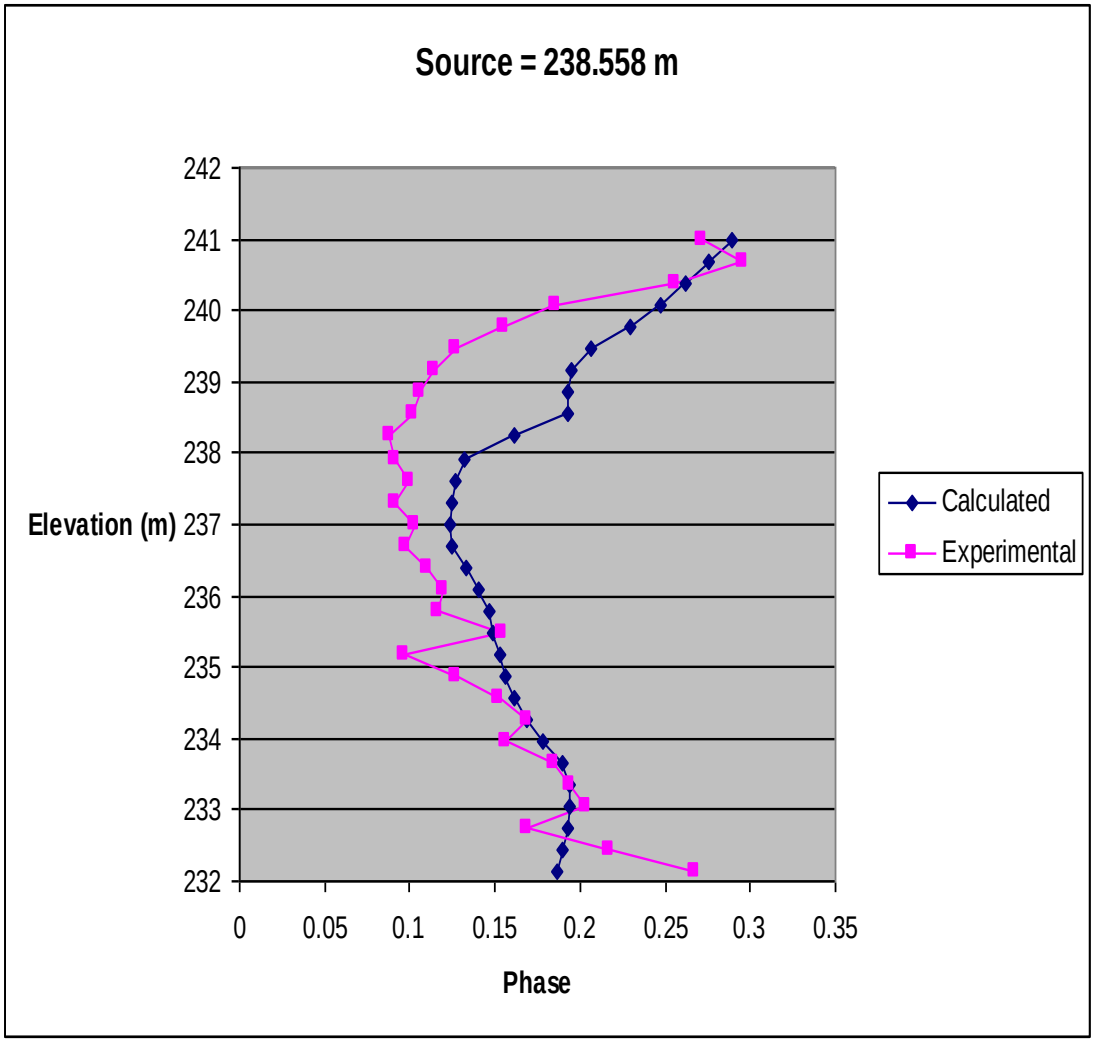

Figure 87: Experimental field phases and phases calculated using constrained SVD for a MOG from well HT-6 to well HT-3 with a source location of 238.558 m.

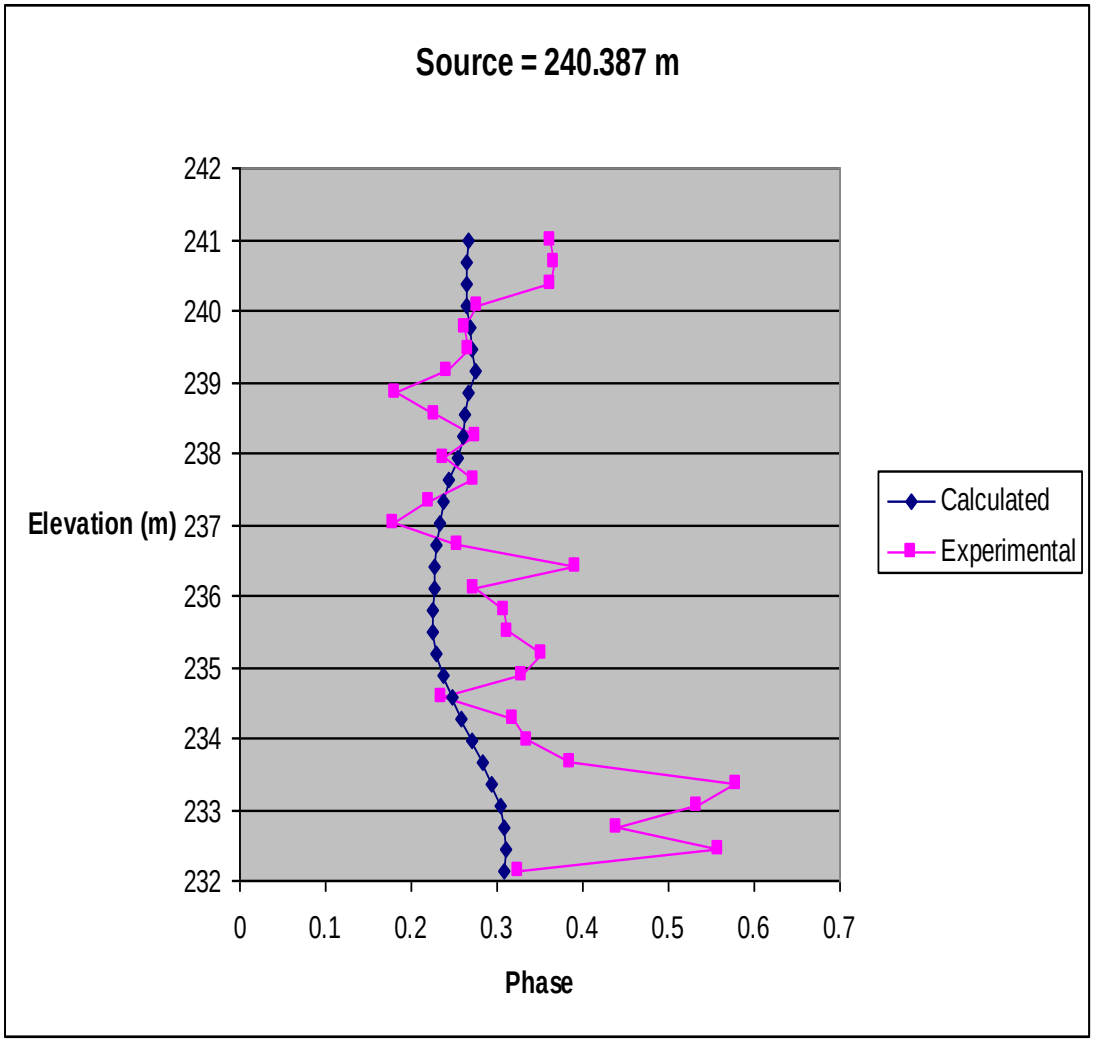

Figure 88: Experimental field phases and phases calculated using constrained SVD for a MOG from well HT-6 to well HT-3 with a source location of 240.387 m.